CHARACTERIZATION OF HYDROTHERMAL FLUIDS WITHIN SYNVOLCANIC FAULTS OF THE ~2.7Ga, MINE SEQUENCE, NORANDA DISTRICT, QUEBEC

by

STEPHEN M. ZUBOWSKI

Thesis presented as a partial
requirement in the
Master of Science (M.Sc.) in Geology

School of Graduate Studies
Laurentian University
Sudbury, Ontario

Library and Archives
Canada

Published Heritage
Branch

395 Wellington Street
Ottawa ON K1A 0N4
Canada

Bibliothèque et
Archives Canada

Direction du
Patrimoine de l'édition

395, rue Wellington
Ottawa ON K1A 0N4
Canada

Canadä

ABSTRACT

The McDougall I, McDougall II and C-shaft faults are synvolcanic structures that accommodated subsidence and acted as conduits for magmas and ascending hydrothermal fluids that were responsible for the formation of volcanogenic massive sulfide deposits within the Mine Sequence of the ~2.7Ga, Noranda Volcanic Complex. Fluid inclusions within hydrothermal quartz-chalcopyrite breccia veins in these faults are of moderate to high salinity and have minimum temperatures of entrapment (T_h – homogenization temperature) <250°C, a temperature range in which chloride brines are incapable of transporting significant quantities of Cu, unless under unusually oxidizing conditions. Fluid Inclusion Assemblage (FIA) salinities and homogenization temperatures from early pre-mineralization comb-textured quartz indicate that the fluids had salinities of 5.8 - 14.0wt% NaCl equiv., and low-moderate temperatures of 125 - 212°C (up to 378.9°C – for individual inclusions not part of an FIA). Phase separation caused by boiling within the conduit, resulted in inclusions with salinities of 0.5 - 3.6wt% NaCl equiv., below that expected for Archean seawater. Secondary ore-related FIAs have salinities of 4.1 - 17.4 wt% NaCl equiv., minimum temperatures of entrapment with T_h ranging from 138.0 to 236.7°C and salinity vs. T_h trends suggestive of mixing between lower salinity and higher temperature fluids.

Results from microthermometry and salt decrepitation mound analysis are consistent with fluids that are predominantly evolved seawater with compositions having been modified via fluid-rock interaction within semiconformable alteration zones in the Mine Sequence. Less common are saline fluids inclusions containing dominantly immiscible CO_2 within the McDougall II fault that suggest phase separation at depth and

heterogeneous entrapment, with salinities in the 0.8 - 21.3wt% NaCl equiv. range, Th_{CO2}

from 9.1 - 21.1°C and decrepitation temperatures (T_d) of 294.3 - 477.4°C. The calculated

hydrostatic pressure for CO_2 bearing inclusions indicates that trapping occurred of 9.2-

13.9 MPa, consistent with an open to seafloor fault system and a water depth of <400m.

Volatiles from quartz and chalcopyrite separates include, in order of abundance H_2O »

$CO_2 \geq CH_4 > N_2 \geq COS > C2$- HC's > C3- HC's, and are consistent with the volatile

composition of discharging fluids from modern, back-arc hydrothermal systems. Quartz

separates have $\delta 13C_{CH4}$ and $\delta 13C_{CO2}$ isotopic signatures representative of a depleted

source for CO_2-bearing fluids in the McDougall I fault, and magmatic and seawater

sources for CO_2-bearing fluids in the McDougall II fault. The latter data indicate that

magmatic fluids were, at least episodically, incorporated into a dominantly evolved

~2.7Ga seawater hydrothermal system at Noranda.

ACKNOWLEDGEMENTS

TABLE OF CONTENTS

APPENDICES ARE LOCATED ON A DVD IN THE BACK POCKET

LIST OF FIGURES

LIST OF TABLES

CHAPTER 1
INTRODUCTION

Goals and Objectives of the Study

Most fluid inclusion (FI) studies of volcanogenic massive sulfide (VMS) deposits have focused on fluids trapped within quartz and sulfide (principally sphalerite) directly below or within the massive sulfide lens and have indicated that fluids with salinities in the range of seawater are dominant (Spooner and Bray, 1977; Costa et al., 1983; Khin Zaw et al., 1996; Ulrich, 2000; Hou et al., 2001; Sanchez-España et al., 2003; Dreiberg, 2003; Weiershäeuser, 2005). Results of these FI studies have been used to suggest that dominantly an evolved seawater (Seyfried et al., 1988) hydrothermal systems as opposed to magmatic hydrothermal systems have been responsible for the formation of VMS deposits (i.e., Dreiberg, 2003; Ioannou, 2004; Moura, 2005). Evolved seawater fluids are chemically distinct from seawater (Seyfried and Janecky, 1985, Janecky and Seyfried, 1982) and are Mg^{2+} and SO_4^- free and are enriched in Ca^{2+} to maintain fluids of 0.55 molal concentration (Seyfried et al., 1988). However, it is unclear if this seawater signature at the seafloor or in the near-seafloor environment of the massive sulfide deposit reflects seawater from a seawater dominated convective hydrothermal system modified through interaction with wall rock in semiconformable alteration zones, or local, less evolved seawater that has been drawn into the deposit and immediate footwall rocks where it would dominate the near seafloor discharge environment. This question is particularly important, as the footwall rocks to VMS deposits in many districts have undergone extensive hydrothermal alteration and are located within broad zones of semiconformable alteration where seawater has interacted with the volcanic and sedimentary rocks at various temperatures (Hannington et al., 2003; Franklin et al., 2005;

1

Dubé et al., 2007). The end result of seawater–rock interaction is evolved seawater fluids with salinities and temperatures greater than seawater. Thus, is there then a record of evolved seawater fluids and perhaps magmatic fluids in VMS deposits? To test this hypothesis it is necessary to sample fluids from deeper levels below their discharge sites where ambient seawater has had less influence on the discharge hydrology of the VMS system (Spooner and Bray, 1977). This has not been done in active systems on the modern seafloor because of the obvious difficulty in obtaining samples. However, it can be done in ancient VMS hosting successions where the footwall strata are exposed either at surface or in drill core. Thus, the purpose of this study is to provide temperature and compositional constraints on hydrothermal fluids that are trapped within sulfide mineralized quartz veins in hydrothermally altered synvolcanic faults that represent the deep, sub-seafloor fluid conduits for Archean VMS deposits. This was accomplished by detailed mapping and sampling of two synvolcanic faults, the McDougall (McD) I/II and C-shaft (C) faults, within the Archean Noranda Volcanic Complex (NVC) (Santaguida et al., 1998) (Fig 1.1). The NVC was chosen as the study area because of its low metamorphic grade, minimal deformation, and because previous research had identified synvolcanic faults that were conduits for the hydrothermal fluids responsible for forming overlying VMS deposits (Setterfield et al., 1995; Santaguida et al., 1998; Hannington et al., 2004).

Location and Access

The NVC is host to 20 past-producing VMS deposits and 10 sub-economic VMS deposits, of which 18 past producing and 5 sub-economic deposits occur within the

Noranda formation (Cycle III and IV) (Gibson and Galley, 2007). The study area is

located near the Corbet deposit, some 6.6 km north-east of the town of Rouyn-Noranda,

Quebec, (Fig 1.2). The 2.78 Mt Corbet deposit (2.92% Cu, 1.62% Zn, 1.00g/t Au and

21.00 g/t Ag) was discovered in 1974 and was mined until 1984, and is one of the

stratigraphically lowest deposits within the Mine Sequence (Gibson and Galley, 2007).
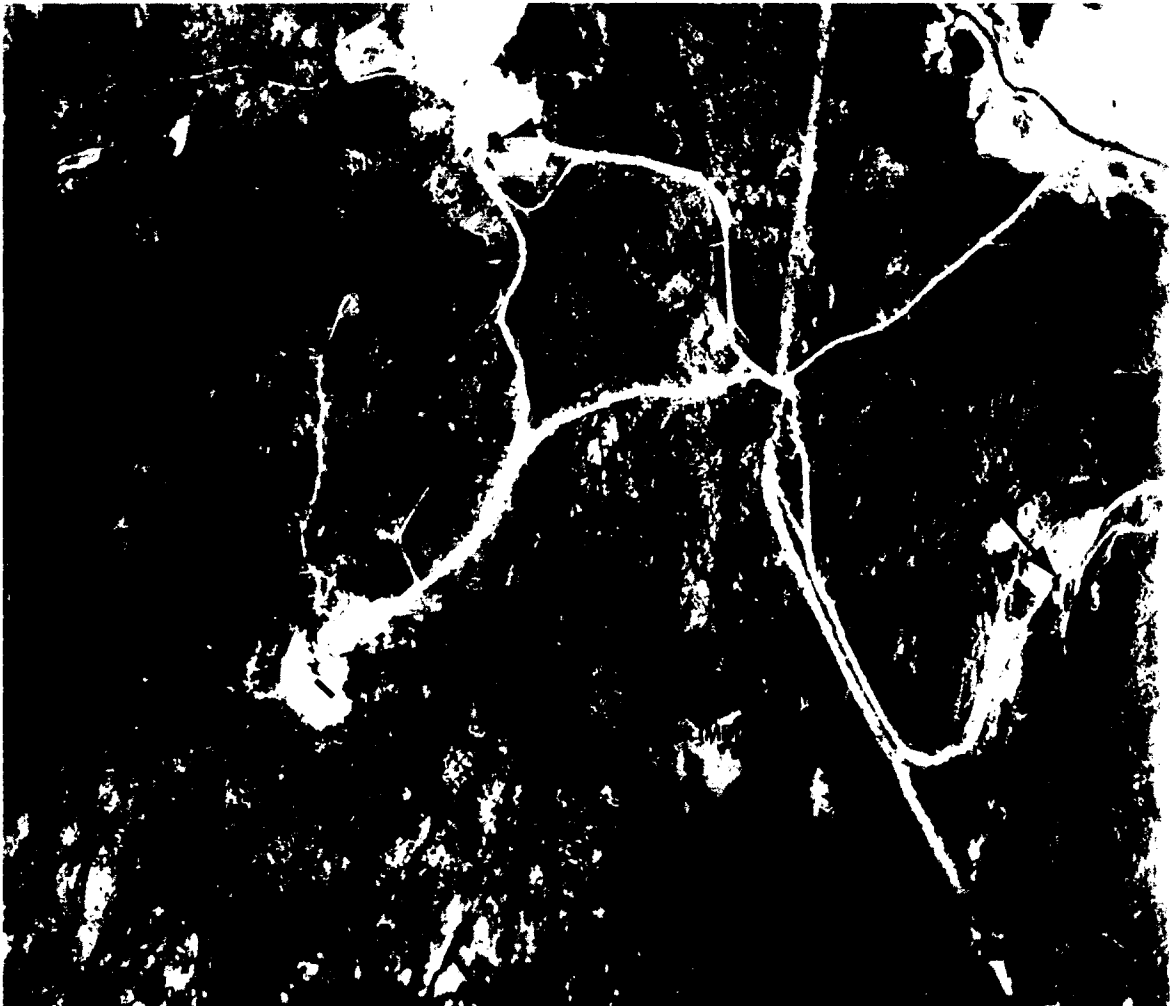
Figure 1.1: South-western portion of the Noranda Volcanic Complex (NVC) highlighting the location of the McDougall I and II and C-shaft Faults. The location of the Corbet Deposit, Millenbach Deposit and the Amulet "C" orebody are also indicated.

Access to the area is via Rue Saguenay (Hwy 101) to the Millenbach Road,
located 6 km north of Rouyn-Noranda. The Millenbach road is followed west then north
for 2.9 km until an unnamed gravel road (the Corbet Road) that extends west another 1.4
km to the rehabilitated Corbet deposit mine area. The outcrop exposures for the
McDougall faults are located ~100m south and south-west of the capped Corbet deposit
shaft respectively. The C-shaft fault was accessed by a 1.2 km traverse north-east of the
rehabilitated Corbet mine area (Fig 1.2).
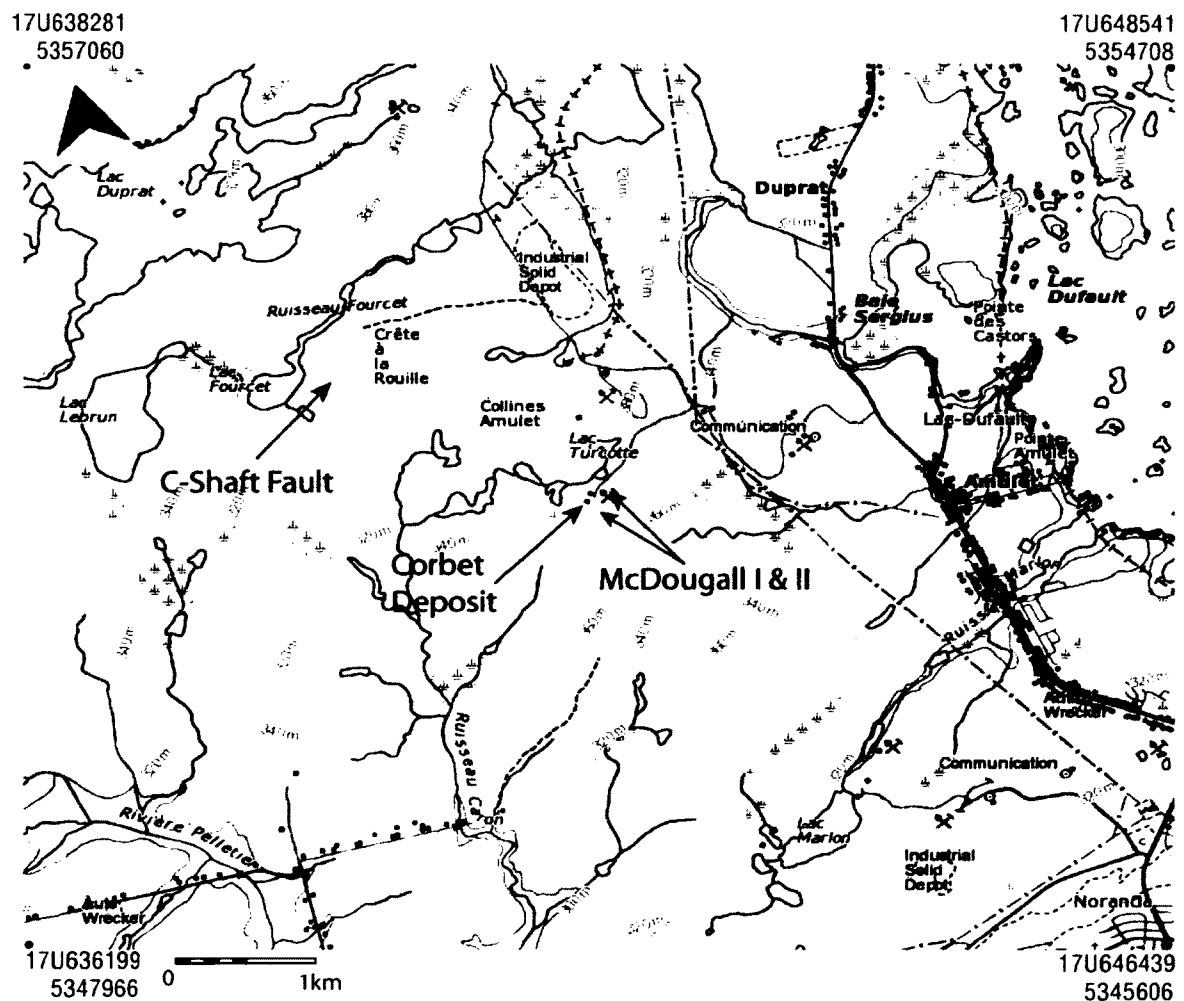
Figure 1.2: Location map of the McDougall I, II, C-shaft faults and the Corbet
Deposit. Information from Natural Resources Canada, Topographic Maps (2010).

Field and Analytical Methods

During the months of July and August 2002, 1:40 scale surface maps of 4 exposed mineralized sections of the McDougall and C-shaft faults were created, including photos for compilations of the map areas. A total of 46 samples of quartz filled amygdules in rhyolite exposed in trenches through the sub-economic Bedford deposit, and quartz-sulfide filled amygdules in silicified andesitic flows flanking the McDougall and C-shaft fault structures were also collected but no further research was conducted on these samples during this study. A total of 15 samples from the Corbet deposit, were collected from collections at Carleton University and the Geological Survey of Canada and 15 polished thin sections and 8 fluid inclusion sections were made from these samples. An additional 3 samples from the Corbet deposit had also been previously analyzed by microthermometry at the University of Toronto (Zubowski, 2001). In total 127 fluid inclusions analyzed representative of the Corbet deposit stockwork zone were analyzed and included with this study.

During the months of July and August 2003, detailed maps of the sulfide-quartz veins at the McDougall faults was created at a scale of 1:20. During mapping, 75 rock samples were collected (exact locations documented) from within the McDougall I, McDougall II and C-shaft faults and 28 thin sections and fluid inclusion section pairs were prepared. Petrography and flatbed scanned images to identify potential locations for fluid inclusion analysis were completed. A total of 547 microthermometric T_m/T_h pairs were measured using the Linkam THMS-600 fluid inclusion stage at Laurentian University on a Nikon Optiphot microscope with 5x, 10x, 50x and 100x long working

distance objective lenses. All fluid inclusions were documented in relation to their mineral assemblage and the texture of the host quartz.

To identify other major cations present in the inclusions, 12 samples were analyzed using the breached inclusion technique at Vale Exploration, Copper Cliff using a JSM-6400 scanning electron microscope with an Energy Dispersive X-ray Spectrometer (EDS) and 9 samples were analyzed using decrepitation mound analysis at Laurentian University using a JSM-6400 scanning electron microscope. Twelve samples hosting CO_2 bearing fluid inclusions underwent further compositional analysis using gas chromatography at the University of Toronto. Quartz and chalcopyrite separates were hand-picked from crushed samples.

A total of 6 hand samples from the McDougall I and II faults, over the fall and spring term of 2006 were analyzed by Laser Ablation - Induced Coupled Plasma Mass Spectroscopy (LA-ICPMS) at the Ontario Geoscience Laboratories for major and trace elements using a closed beaker digest. Of the 12 samples analyzed by gas chromatography, 10 were submitted to the University of Western Ontario for gas chromatography – isotope ratio mass spectrometry (GC-irMS) (10 samples with 3 aliquots analyzed per sample with each sample consisting of 2 duplicates). Individual compositional analysis of fluid inclusions from 19 chip-mounted samples representing 12 samples, were analyzed using Laser Ablation – induced coupled plasma mass spectroscopy (LA-ICPMS) at Laurentian University. Results of the LA-ICPMS analysis were inconclusive and therefore not further discussed, but the data can be found in Appendix 7. In June of 2010, 8 thin sections were examined by Dr. Götze at Freiberg

University, Germany using "hot-cathode" cathodoluminescence (CL), to verify that the vein quartz exhibits hydrothermal signatures and growth zoning.

Structure of the Thesis

This thesis is structured such that Chapter 1 provides a general introduction to the study and the goals and objectives of the project including field and analytical methods. Chapter 2 summarizes the geology of the Noranda District and provides a description of the synvolcanic McDougall and C-shaft faults. Chapter 3 presents analytical data pertaining to the fluid inclusions studied in order to constrain the physico-chemical characteristics of the fluids within the synvolcanic structures. The chapter is organized such that the operating parameters of the analytical instruments and sample preparation methods are described first, followed by the results, and then by an interpretation of the data specific to that technique. Chapter 4 includes a discussion and lists the conclusions of the research. The four chapters are followed by 10 Appendices which contain details and results of the mapping and the analytical techniques employed. Larger prints of the 1:40 scale maps are located in the back pocket.

Research Funding

Funding for this project was provided by an NSERC Strategic Grant #STPGP 224028-99 awarded to Drs. E.T.C. Spooner, and S.D Scott, at the University of Toronto and Dr H.L. Gibson, at Laurentian University. Additional funding was provided by an NSERC Discovery Grant (Dr. Gibson) and an SEG Student Grant.

The NSERC Strategic Grant was in support of three geoscience projects aimed at refining and quantifying the ore-bearing hydrothermal model for the world class volcanic – hosted massive sulfide ore system at Noranda, Quebec. This study is one of the

geoscience projects and the other two projects focused on the fluid

chemistry/characteristics of hydrothermal fluids within the peripheral recharge zone, the

semi-comformable alteration zones (Ms. Renée Turmel), and within the synvolcanic

Flavrian and Powell Plutons (Ioannou et al., 2004; Weiershaeuser, 2005; Weiershaeuser

and Spooner, 2005).

CHAPTER 2
REGIONAL GEOLOGY

Regional geology of the Noranda Area

The VMS deposits of the Noranda District are hosted by the Noranda Subgroup of the 2.7 Ga Archean Blake River Group, located within the south-central segment of Abitibi Subprovince (Figs. 2.1, 2.2 and 2.3). The Abitibi Subprovince forms an east-trending, 700x300 km wide greenstone belt in the southernmost Superior Province, which extends from eastern Ontario into western Quebec (Dimroth, 1982). The southern segment of the Abitibi Subprovince is composed of volcanic-dominated supracrustal, minor sedimentary and intermediate to felsic syntectonic-synvolcanic intrusive rocks (Jolly, 1978; Dimroth, 1982; Mortensen, 1993). Regional metamorphic grade increases from prenhite-pumpellyite in the south, to greenschist facies in the northern region (Ayer et al., 2002). The Abitibi Subprovince is the largest and best-preserved greenstone belt in the Superior province (Card, 1990) and one of the most productive base metal regions in Canada, containing a total of 83 VMS deposits with an aggregate tonnage of 730 Mt, clustered within 13 districts (Gibson and Galley, 2007; Franklin et al., 2005).

The Blake River Group is located within the south-central region of the Abitibi Subprovince and consists of strata composed of subaqueous calc-alkaline to transitional arc basalts and lesser andesites, with local rhyolites (Mortensen, 1993; Ayer et al., 2002) (Fig. 2.2). The volcanic rocks comprise a tectonic setting that is thought to represent an arc or back-arc environment, with volcanic signatures interpreted to form in a plume dominated extensional environment with periodic arc and rifted arc magmatism (Gibson and Galley, 2007; Ayer et al., 2002). Stratigraphic subdivision of the Blake River Group currently includes 6 subgroups, but this subdivision is under revision. In its current state,

9

stratigraphic subdivision with corresponding geochronological data has been summarized by Gibson and Galley (2007) in Fig. 2.3.

Recently, the Blake River group has been interpreted to be a mega-caldera, referred to as the Misema Caldera (Pearson and Daigneault, 2009). The boundaries of this megacaldera encompasses the entire Blake River group and included two internal calderas, the New Senator and Noranda calderas respectively.

Geology of the Noranda District and Noranda Subgroup

The VMS deposits of the Noranda District occur in three structurally bounded subgroups, the Rouyn-Pelletier, Noranda, and Renault-Dufresnoy subgroups (Gibson and Galley, 2007). Of particular interest to this study is the Noranda Subgroup, which contains 18 VMS deposits and the synvolcanic faults studied and described herein. The larger and gold-rich Horne deposit occurs in the older Rouyn-Pelletier subgroup. VMS deposits in the Noranda subgroup occur within the 3 km thick Mine Sequence, comprised of tholeiitic to transitional basaltic to andesitic and rhyolitic flows with minor volcaniclastic rocks (Gibson and Watkinson, 1990). The Mine Sequence is interpreted to have been erupted during a period of cauldron subsidence (Gibson and Watkinson, 1990).

The Flavrian pluton is interpreted to be a multi-phase, shallow dipping, high level syn-volcanic sill-like intrusion that intruded the Mine Sequence at various stratigraphic intervals (Goldie, 1979; Kennedy, 1985; Richard, 1999; Galley, 2003). The 5 phases, from oldest to youngest, include the Meritens quartz-diorite, tonalite, early and late trondhjemite and ending with a post volcanic albite granite. It has been suggested that the Flavrian Pluton was emplaced into its own volcanic pile during and after cauldron subsidence (Gibson and Watkinson, 1990), with the annular distribution of the earlier

Mines
1. Kam-kotia
2. Kidd Creek
3. Dome et al.
4. Shunsby
5. Sigma Lamaque
6. Selbaie
7. Joutel
8. Matagami deposits
9. Chibougamau deposits
10. Gonzague-Langlois
11. Noranda area
    Laronde.
    Home

Geological Units

crb	Belle River complex	mar	Marest Pluton	rlb	Round Lake batholith	
bro	Brouillan pluton	mst	Mistaouc batholith	scapa	Scapa wackes	
chi	Centre Hill intrusion	n	Nat river batholith	wan	Waswanipi North Pluton	
	and Potter mine	pou	Poularies pluton			
eja	Eau Jaune complex	ra	Ramsey Algoma batholith			
grs	Ghost range sill	r	Rice Lake batholith			
k	Kenogamisi batholith	rss	Rosseau pluton			
lap	Lapparent massif					

Faults
PDF Porcupine-Destor Fault
LCF Larder-Cadillac Fault
BRF Buskegau River Fault
MRF Matagami River Fault

〜〜〜 **Unconformity**

HURONIAN AND PALEOZOIC COVER

ABITIBI ASSEMBLAGES
2676 to 2670 Ma
(Timiskaming)
▇ Sedimentary
▇ Volcanic
〜〜〜

2690 to 2685 Ma
(Porcupine)
☐ Sedimentary
☐ Volcanic
〜〜〜

2704 to 2696 Ma
(Blake River)
▇ Upper Unit
▇ Lower Unit

2710 to 2704 Ma
(Tisdale)
☐ Upper Unit
▇ Lower Unit

2719 to 2711 Ma
(Kidd-Munro)
〜〜〜
☐ Upper Unit
▨ Lower Unit

2723 to 2720 Ma
(Stoughton-Roquemaure)
〜〜〜
▨

2730 to 2724 Ma
(Deloro)
〜〜〜

2750 to 2735 Ma
(Pacaud)
〜〜〜

> 2750 Ma
▇

Felsic
mafic to ultramafic

Figure 2.1: Geological map of the Superior Province with the Blake River Group located in the lower center of the map. Map provided by Dr. Thurston, Laurentian University.
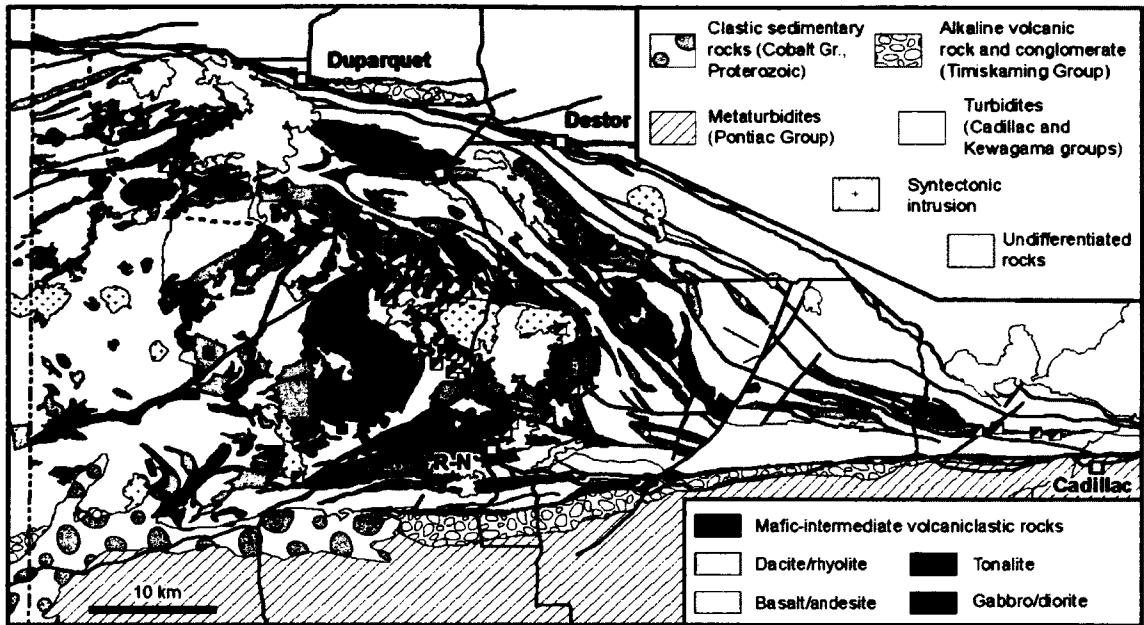
Figure 2.2: Geological map of the Blake River Group in the province of Quebec. Map provided by Dr. Goutier. (Mercier-Langevin, et al., 2011)
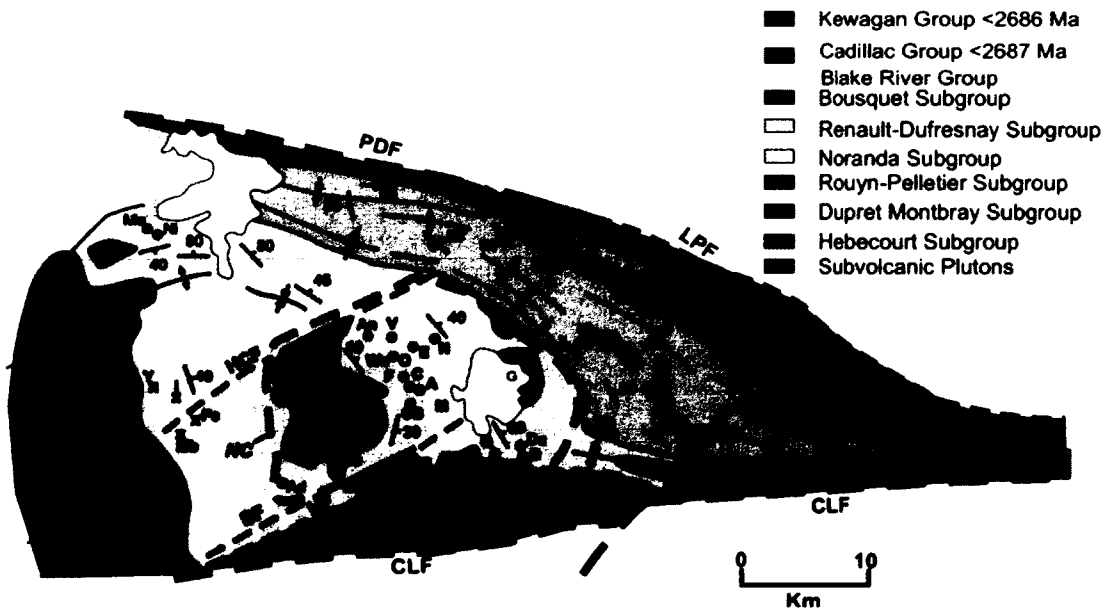
Figure 2.3: Main subgroups of the Blake River Group in the Noranda District. Synvolcanic plutons are represented by the Flavrian (Fp) and Powell Pluton (Pp). (after Gibson and Galley, 2007).

12

Meritens phase reflecting early ring fractures within the core of the Noranda Cauldron

(Setterfield et al., 1995). The Flavrian pluton is surrounded by a 0.5km wide aureole,

characterized by faintly porphyryoblastic, weakly hornfelsed, greenschist facies volcanic

rocks (Setterfield et al., 1995). To the south, the Powell Pluton is interpreted to be the

faulted extension of the Flavrian pluton (Spence and deRosen-Spence, 1975) that has

been displaced by the Beauchastel fault (Goldie, 1976).

Tholeiitic gabbro intrusions commonly referred to as diorite, occur as dikes and

sills throughout the Mine Sequence (Kerr and Gibson, 1993). Low-angle reverse faults

typically occupy the footwall contact of the sill-like gabbro intrusions (Kerr and Gibson,

1993). A single U-Pb zircon age for a gabbro intrusion at the Millenbach mine yielded an

age of 2698 Ma, only slightly younger than the host volcanics dated at 2698.3 Ma

(Goutier et al., 2006). However, the gabbro intrusions are not pervasively spilitized like

the volcanic succession and they are not affected by discordant alteration zones

associated with the VMS deposit (Kerr and Gibson, 1993). The gabbro intrusions may

be feeder dikes and sills to an overlying mafic volcanic succession that was removed by

erosion (Gibson, personal communication 2010). The gabbro intrusions and volcanic

strata are crosscut by the Lac Dufault pluton, which consists of 2 intrusions. The

western-most intrusion is post volcanic biotite granodiorite, surrounded by a 2km wide

contact metamorphic aureole of hornblende hornfels facies (Kerr and Gibson, 1993) and

has been dated at 2690 +/-2Ma (Mortensen, 1993). The eastern intrusion is synvolcanic

tonalite.

The Noranda subgroup, is interpreted to occupy a 15 by 20 km synvolcanic

subsidence structure that was first recognized by deRosen-Spence (1976), and was

defined and named the Noranda Cauldron by Gibson and Watkinson (1990). The

Noranda cauldron is centered on the Old Waite Paleofissure, a 1-km wide northeast

trending rift (Gibson, 1990; Gibson and Watkinson, 1990). The cauldron is bounded to

the north by the Hunter Creek fault and the Horne Creek fault to the south (Dimroth et al.,

1982; Gibson and Watkinson, 1990). The eastern structural margin of the Noranda

Cauldron is interpreted to be defined by the Dalembert Shear and synvolcanic Dalembert

Pluton, and the western margin is now represented by the Flavrian-Powell Pluton (Gibson

and Watkinson, 1990; Kerr and Gibson, 1993; Gibson and Galley, 2007) (Fig 2.4).

Subsidence of the Noranda cauldron occurred in two stages, the first coincided with

eruption of basaltic andesitic and rhyolitic flows that comprise the Flavrian, Northwest,

Rusty Ridge and Amulet formations, the second stage is represented by eruption of

basaltic andesitic and lesser rhyolitic flows of the Millenbach, Waite and Amulet

Andesite formations. The interval or hiatus between subsidence cycles is marked by the

occurrence of an extensive deposit of bedded tuff, referred to as the C-Contact tuff.

Economic VMS deposit distribution within the Noranda District is not uniform

(Gibson and Galley, 2007), with 90% of the past producing deposits and 50% of the sub-

economic deposits occurring within the Mine Sequence (Gibson and Galley, 2007).

Within the Mine Sequence, the Corbet and Ansil deposits formed during volcanism and

subsidence associated with the first stage of cauldron subsidence. During a hiatus

between subsidence stages small Zn-rich deposits formed along the "C" Contact Tuff

(Amulet C, Dufault, Moosehead and F-shaft deposits). With the onset of the second

subsidence cycle, the Millenbach-D68, Amulet A, Old Waite, East Waite, Vauze and

Norbec deposits formed along the Main contact tuff (Gibson and Watkinson, 1990).

14
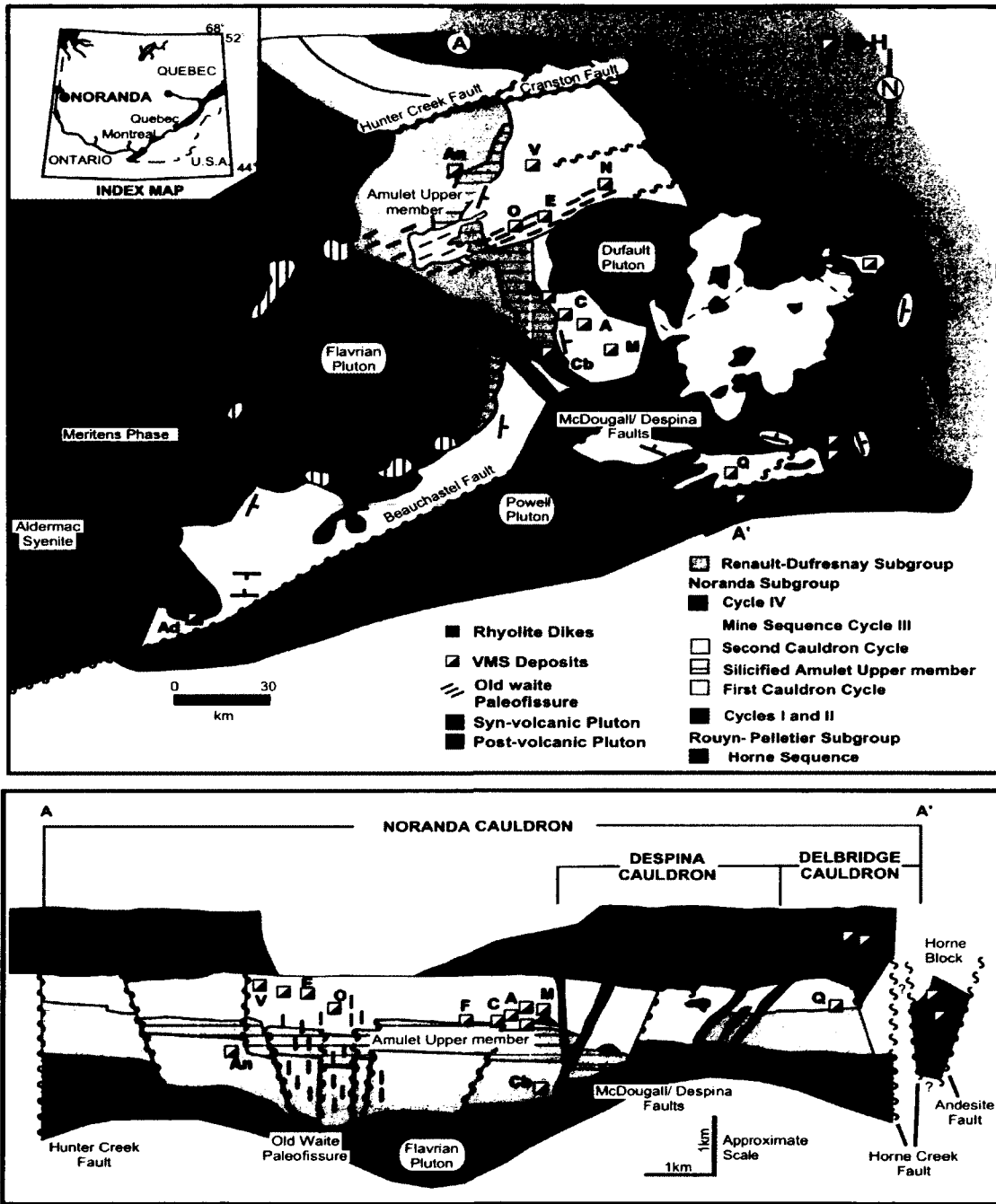
Figure 2.4: Plan view and cross-section through the Noranda Cauldron. Note the nested cauldrons and collapse accommodated by the McDougall-Despina Faults. The McDougall fault also accommodated emplacement of the Flavrian Pluton (Meritens Phase). (Gibson and Galley, 2007).

Although VMS mineralization formed during eruptions and collapse of the cauldron, the fundamental control on the location of VMS deposits are volcanic vents which define eruptive centers and these are localized along synvolcanic faults and fissures and less well defined ancillary structures (Gibson and Watkinson, 1990). For example, the McDougall-Despina Fault, and parallel, intersecting and ancillary faults accommodated subsidence of the Despina cauldron along the south-western margin of the Noranda Cauldron and localized the Corbet and D-68 VMS deposits that are separated by 1000 m of strata (Ikingura, 1984). Additionally, the C-shaft fault, a 070 trending fault oriented normal to the McDougall-Despina faults, intersected the Amulet C deposit, which is the northernmost known deposit aligned along the Amulet-Millenbach structure. Deposits within the Amulet-Millenbach structure occur over a 300m stratigraphic interval, indicating that these synvolcanic faults and similar structures within the Noranda cauldron not only accommodated subsidence, but also provided cross-strata pathways for ascending hydrothermal fluids and magmas during volcanism (Gibson, 1990).

VMS Deposits and Alteration

VMS deposits are syngenetic and they form contemporaneously with volcanism by the precipitation of sulfide minerals on or below the seafloor from a modified seawater hydrothermal fluid that is typically within a temperature range of 300-400°C (Franklin et al., 2005; Gibson and Galley, 2005; Lydon, 1984). VMS deposits within the Mine Sequence have a conformable bulbous or conical shaped massive sulfide lens (>60% sulfides) with a lower contact that transitions into a discordant, vein-type mineralized stringer or stockwork zone (Franklin et al., 1995; 2005) (Fig 2.5). Mineralization is simple, with pyrite, sphalerite, chalcopyrite and galena typically forming the massive ore

and chalcopyrite, pyrite, pyrrhotite, sphalerite and magnetite forming the stringer zone (Franklin et al., 1995).

MASSIVE SULFIDE LENS

"Exhalite" or "Tuff" unit
10
60
Sp+Py±Cp+Po+Gn
Py±Sp+Gn
90
14
stratification
Alteration Pipe
90 — Cu x100 / Cu+Zn
Disseminated +/- fracture mineralization (py,sp)
Fracture + Disseminated Mineralization (cp,po) "STOCKWORK" or "STRINGER ZONE"
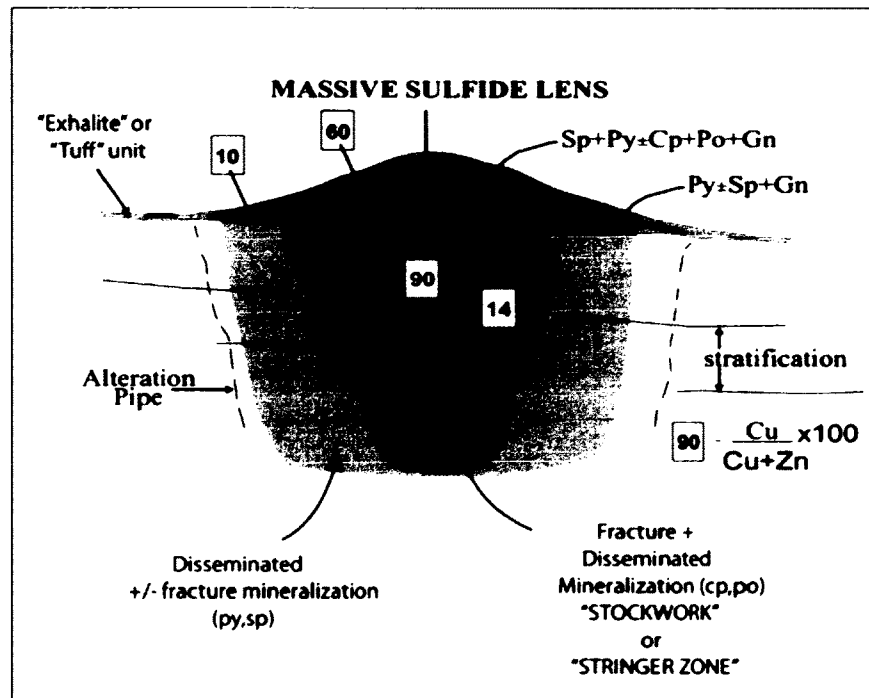
Figure 2.5: General shape and metal zoning of a Noranda VMS deposit. The sulfide stringers merge to form single narrow pipe-like conduit that is controlled by a primary synvolcanic fault or fissure (Gibson and Galley, 2007).

VMS deposits in the Mine Sequence at Noranda are associated with two types of alteration, proximal discordant alteration zones that is directly associated with the VMS deposits, and regional-scale zones of semiconformable alteration. In the flow dominated Mine Sequence the proximal discordant alteration zones have a vertically extensive, pipe-like morphology. They are characterized by an inner zone of chlorite alteration (Mg to more Fe-rich chlorite toward the centre of the "pipe") and an outer zone or margin of sericitic alteration (Gibson and Watkinson, 1990). The discordant alteration zone results from the interaction between ascending, high temperature, low pH, ore fluids and down-drawn seawater with their wall rocks (Franklin et al., 1981; 2005).

Semi-conformable alteration zones are produced by synvolcanic fluid flow within VMS hydrothermal (paleo-geothermal) systems that extend down to subvolcanic intrusions and up to the paleo-seafloor (Franklin et al., 2005). The hydrothermal fluid is seawater and evolved seawater that has been modified through interaction with volcanic rocks (Gibson, 1990). Within the Noranda Cauldron, the semi-conformable alteration zone mineralogy is difficult to distinguish from regional scale sub-greenschist and greenschist metamorphic assemblages (Hannington et al., 2003). For example, spilitization has resulted in a regional greenschist mineral assemblage of chlorite, quartz, epidote and albite in mafic rocks and sericite, chlorite, quartz and albite in felsic rocks of the Mine Sequence (Gibson, 1990). Within the regional spilitization of the Noranda cauldron, textures indicating former palagonite and zeolite have been recognized and they attest to an earlier, lower temperature, seafloor to sub-seafloor alteration.

The range in mineral compositions determined by Hannington et al. (2003), within the Mine Sequence, exceed the temperatures that would be commonly associated with regional greenschist and subgreenschist facies metamorphism of the Blake River Group. Fe-rich chlorite compositions within felsic rocks of the Mine Sequence are more iron-rich than in basalts elsewhere in the Blake River formation that are less altered, and are similar to chlorite found within VMS alteration pipes. Likewise, irregular epidote-quartz alteration patches on the decimeter to meter scale, overprint regional spilitization within mafic volcanic rocks throughout the Blake River Group. This alteration is also concentrated along syn-volcanic structures, dikes and sills, and along the margins of the Noranda cauldron (Gibson and Galley, 2007). Epidote-quartz alteration within the NVC is characterized by clinozoisite and quartz +/- amphibole assemblage that has granular

mosaic texture (Gibson and Galley, 2007). The ranges in iron composition within clinozoisite of the Noranda cauldron suggest temperatures approaching amphibolite facies inconsistent with their greenschist facies and indicating a hydrothermal origin for the clinozoisite (Hannington et al., 2003). Furthermore, a regional oxygen isotope study by Cathles (1993) of the Noranda cauldron indicate its volcanic rocks are generally enriched in ^{18}O (avg. $\delta^{18}O$ is 7.4 ± 2 ‰ enriched relative to SMOW), with higher temperature linear zones showing a relative $\delta^{18}O$ depletion ($\delta^{18}O < 6‰$) associated with synvolcanic structures that localized known VMS deposits. Within the contact aureole of the Lac Dufault Pluton, the volcanic rocks were metamorphosed to amphibolite facies; however, the faults within this study are located well outside the contact metamorphic aureole (Gibson, 1990).

DESCRIPTION OF THE MCDOUGALL-DESPINA AND C-SHAFT FAULTS

The McDougall and Despina Faults

The McDougall-Despina faults are two subparallel splays of a single fault located within the Noranda cauldron that defines the eastern margin of the Despina cauldron (Gibson and Watkinson, 1990). The McDougall-Despina fault set has a strike length of 4.8km, trends northwest at 300° to 340° (avg. 310°) and merges into a single fault northwest of the Corbet deposit (Fig 2.4 and 2.6A & B). To the southeast it ends against the Here Creek Rhyolite, which is not offset by McDougall or the Despina faults. The westernmost Despina fault dips to the northeast at 80° and the McDougall fault dips 70° to 80° to the southwest; they intersect at the depth of the Corbet deposits to form a single structure that continues along the northeasterly trend of the Despina fault (Setterfield et al., 1995).

Figure 2.6A

Legend:

Diorite   Amulet Andesite

Dufault Pluton   Amulet Formation

Flavrian Pluton   Rusty Ridge Formation

Meritens Phase, Flavrian Pluton   Northwest Formation

Rhyolite Dike   Flavrian Formation

F   Lac Fourcet   M   McDougall Fault

C   Corbet Deposit   D   Despina Fault

Héré Creek Rhyolite
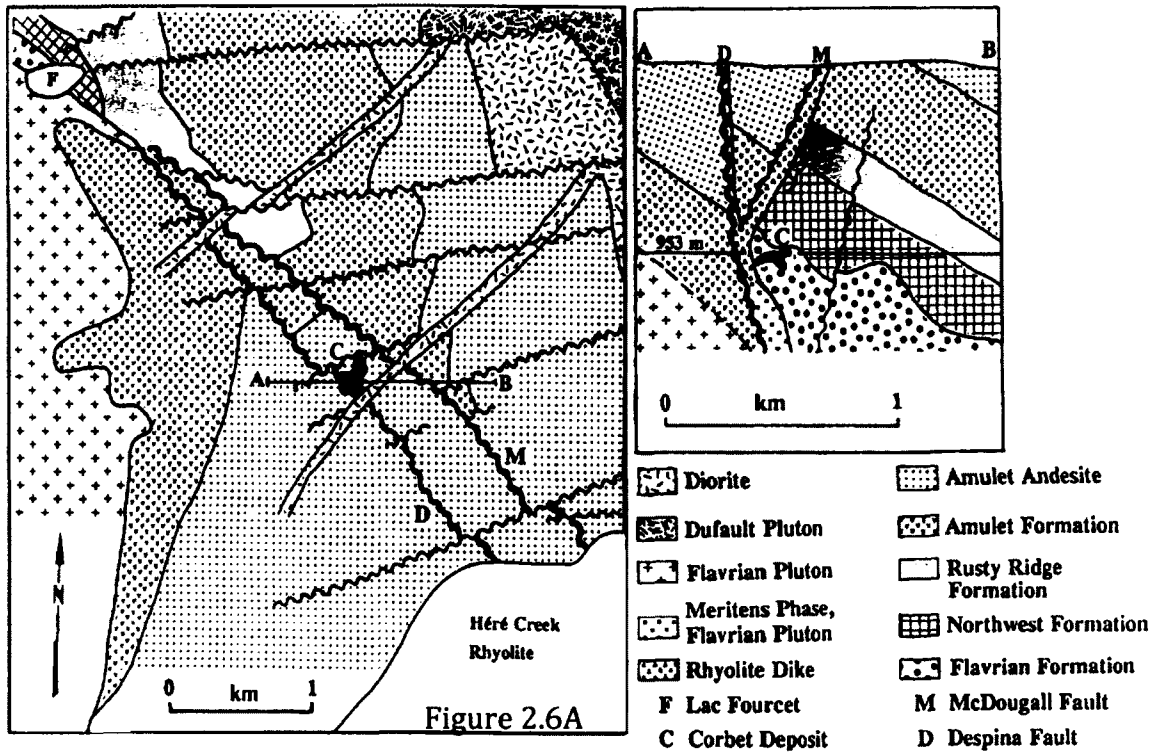
Figure 2.6A: Plan view of the intersection of the McDougall and Despina faults, terminating at Lac Forcet. *From Setterfield et al., 1995*

Figure 2.6B: Vent locations along the McDougall and Despina faults and locations of the Corbet, D-68 and sub-economic Bedford stringer zone. *From Setterfield, 1987.*

Figure 2.6B

20
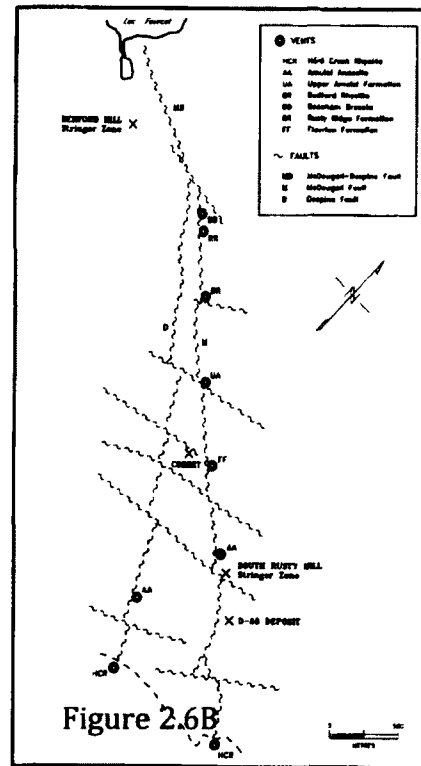
The McDougall-Despina fault is a normal fault that has a total combined vertical displacement of up to 950m (east side up) (Setterfield, 1984; Setterfield et al., 1995). Fault displacements calculated by Setterfield (1984), are in agreement with those of Knuckey and Watkins (1982) (Fig 2.7). Although the McDougall-Despina faults accommodated significant subsidence, movement is constrained to the eruption and emplacement of the Mine Sequence (Gibson, 1990).

The synvolcanic timing and offset along the McDougall-Despina fault is constrained by the Meritens phase of the Flavrian Pluton, and the Here Creek Rhyolite formation, which unconformably overlies the Mine Sequence. The Meritens quartz diorite phase is the oldest intrusive phase of the Flavrian pluton and its annular distribution within the pluton suggests it was emplaced along an early ring-fracture system (Goldie, 1976). At one locality, the Meritens phase occupies the McDougall-Despina fault at surface and diamond drill holes from the Corbet mine intersected the Meritens phase within the fault some 500m from the upper surface of a basaltic flow succession that comprises the Flavrian Formation, where it underlies an andesitic paleo-ridge that localizes the Corbet deposit (Gibson et al., 1993). Adjacent andesitic flows are typically in sharp contact with the Meritens phase, there is no evidence of contact metamorphism, and the Meritens phase displays only weakly developed chilled margins with adjacent flows (Gibson et al., 1993). Additionally, the Corbet discordant alteration zone crosscuts the Meritens phase where it is characterized by a similar chlorite alteration (Gibson, 1989). Therefore, the emplacement of the Meritens phase within the McDougall-Despina fault defines the earliest presence of this fault. Cessation of movement along the McDougall-Despina fault is defined by flows of the Here Creek
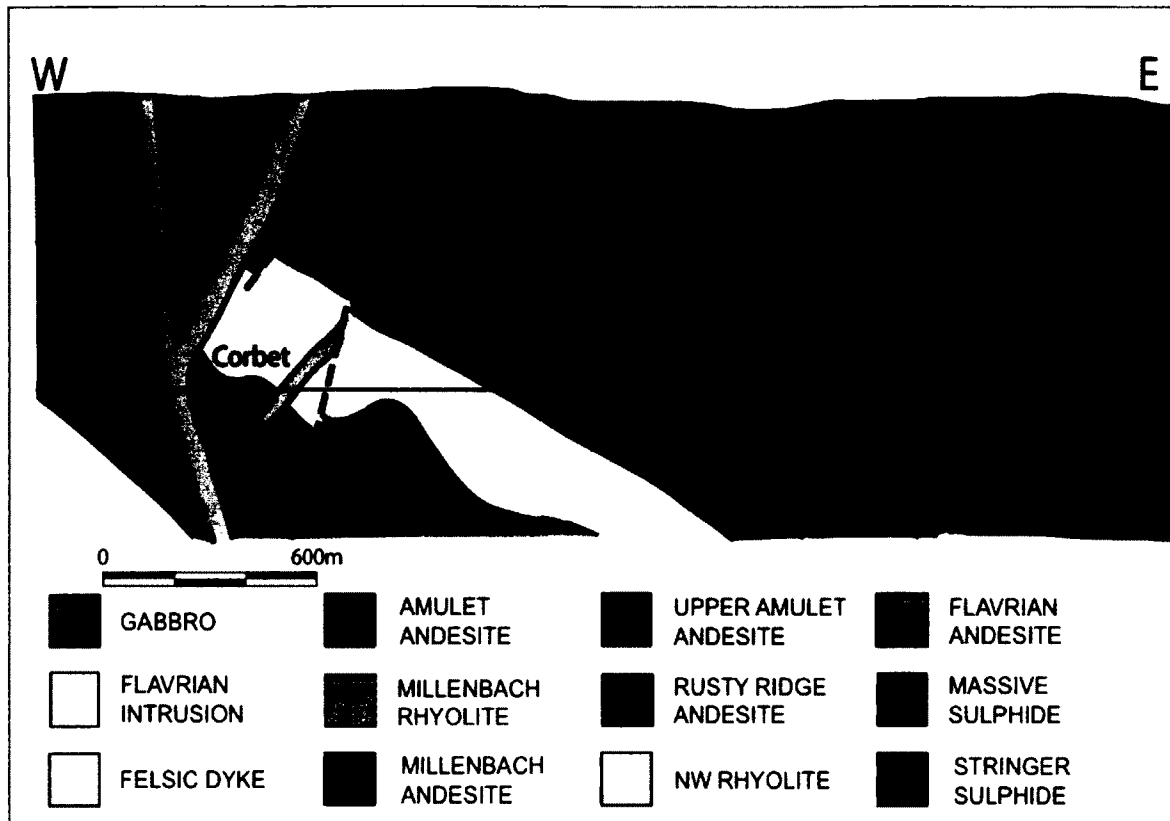
Figure 2.7: East-west cross section through the McDougall and Despina faults showing synvolcanic offset of strata and the location of the Corbet and Millenbach deposits (looking north). *Modified from Knuckey and Watkins, 1982.*

Rhyolite formation, which are not cut or offset by the faults. The Here Creek Rhyolite formation disconformably overlies the Amulet Andesite Formation, indicating that final movement along the faults resulted in tilting of the Amulet andesite flows. There is no evidence of subsequent movement along or within the faults, and rocks adjacent to the faults are undeformed. The faults appear as simple fractures or are occupied by synvolcanic dikes of rhyolite and andesite compositions (Setterfield, 1995); up to 11 dikes occupy the single, merged structure (Fig. 2.8) (Setterfield, 1987; Setterfield et al., 1995). Thus, the syn-volcanic McDougall-Despina faults not only accommodated

subsidence but also controlled magma ascent as defined by the numerous dikes, which

now occupy the structure.
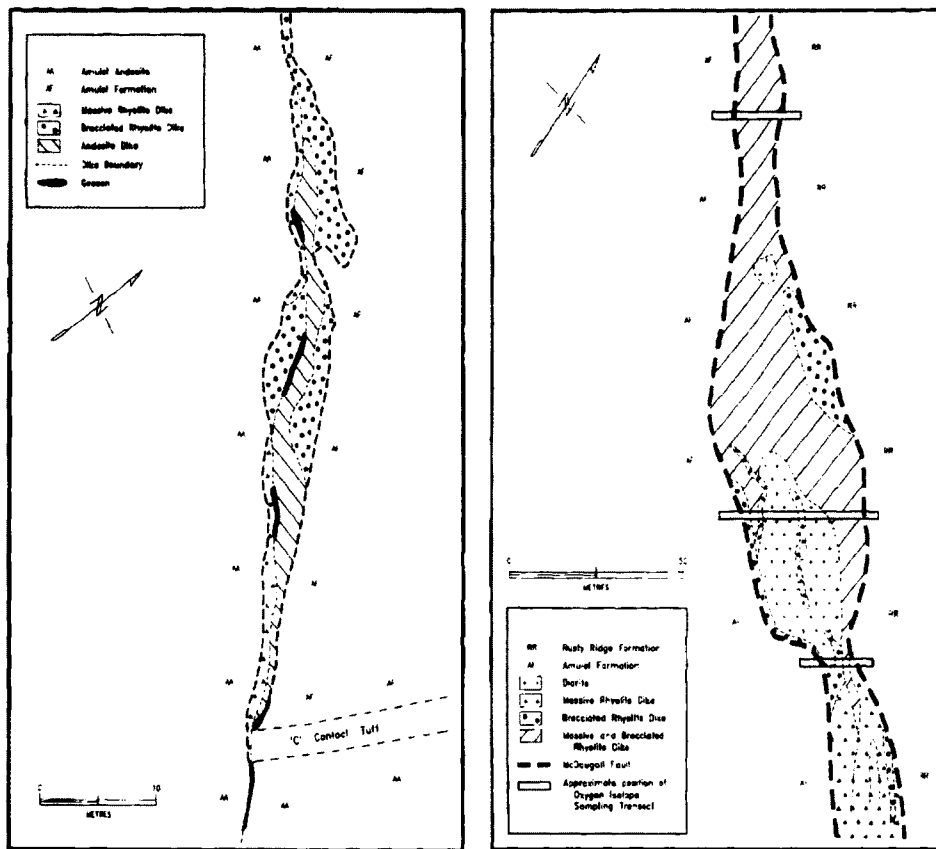
Figure 2.8: Figure to the left shows the relationship between andesite and massive brecciated rhyolite dikes in the McDougall Fault south of the Corbet Mine. The second geological map to the right illustrates eleven separate dikes that occupy the McDougall fault 1.7km northwest of the Corbet Mine. *From Setterfield, 1987.*

The McDougall-Despina fault, in addition to being a synvolcanic fault and

magma conduit also acted as a hydrothermal conduit during emplacement of the Mine

Sequence. For example, within the Amulet Andesite Formation, Setterfield et al. (1995)

defined a 15m alteration zone of sericite and chlorite altered spilitized andesitic flows

adjacent to the McDougall fault, and Gibson et al. (1993), demonstrated that sericite

altered volcanic rocks around the Corbet VMS deposit merged with and paralleled the

McDougall-Despina fault. Oxygen isotopic data from rhyolitic and dioritic dykes within

the McDougall-Despina fault and from the adjacent wall rocks have very low $\delta^{18}O$ values

(3.34-5.64‰) but are still enriched relative to SMOW, indicative of chlorite and sericite

alteration (Cathles, 1993). In addition the Corbet, Bedford and D68 VMS deposits, each

occurring at different stratigraphic intervals within the Mine Sequence are localized along

the McDougall-Despina fault.

The C-Shaft Fault

The C-Shaft fault is located 785m northwest of the Corbet deposit and within the

andesitic flows of the Upper Member of the Amulet Formation (Gibson et al., 1983; Farr,

1984). The C-shaft fault strikes 80° and dips 75-85° to the north and has been traced for

170m at surface from the McDougall fault to the Amulet C orebody. Limited movement

appears to have occurred along the fault, as fragments within the fault are angular and

rocks adjacent to the fault show no foliation or obvious effects of deformation. Quartz-

sulfide vein mineralization along the fault is erratic, occurring in fractured zones 0.5 - 5m

in strike length, with significant mineralization occurring in close proximity to the

intersection with the McDougall fault (Fig 2.9) and Map 1 – back pocket. Gibson et al.

(1983) have shown that the chlorite and sericite alteration that mantles the C-Shaft fault is

identical in mineralogy and in compositional changes to that comprising the chlorite and

sericite alteration associated with VMS deposits. They interpreted the C-shaft fault to

represent the deep structural "root" of a VMS alteration zone.
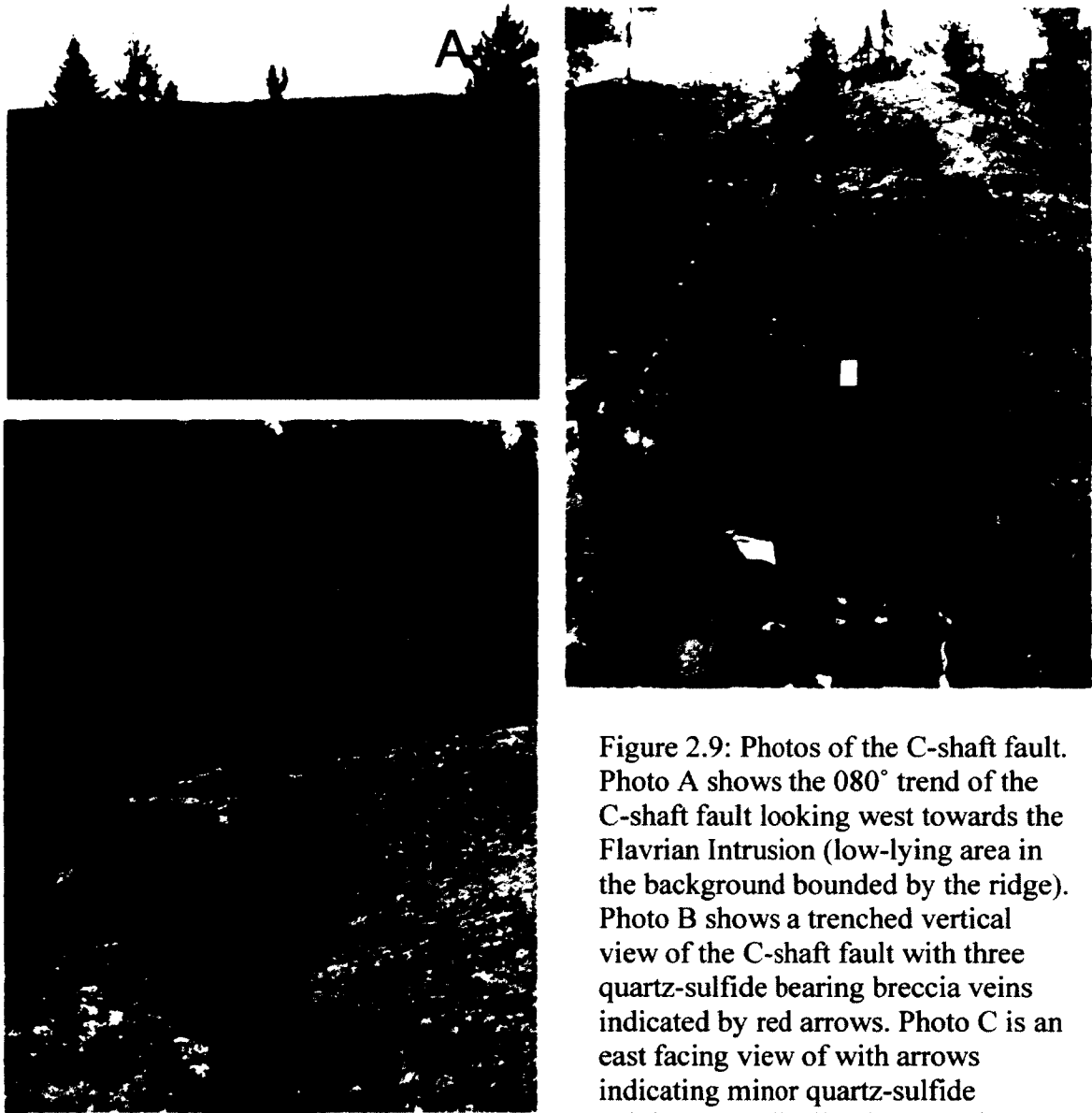
Figure 2.9: Photos of the C-shaft fault. Photo A shows the 080° trend of the C-shaft fault looking west towards the Flavrian Intrusion (low-lying area in the background bounded by the ridge). Photo B shows a trenched vertical view of the C-shaft fault with three quartz-sulfide bearing breccia veins indicated by red arrows. Photo C is an east facing view of with arrows indicating minor quartz-sulfide veining sporadically along the fault.

THE MCDOUGALL-DESPINA AND C-SHAFT FAULTS IN THE STUDY AREA (CORBET AREA)

The McDougall and Despina Faults

The McDougall I and II (McD I/II) faults, the focus of this study, represent ancillary faults to the main McDougall-Despina fault, and they displace similar volcanic facies of the Upper Member of the Amulet Formation (Fig 2.4). The McDougall I (Fig

2.10 A & B; UTM northing 0642402, easting 5351280) and McDougall II faults (Fig

2.10 C & D; UTM northing 0642368, easting 5351120) have limited surface exposure

and are characterized by anastomosing quartz-sulfide mineralized veins. Detailed

mapping of the McDougall I fault focused on 10x12m and 8x3m areas east of the fault

(Back pocket; Map 2A-south, 2B-north). Mapping of the McDougall II fault focused on

a 20x30m area (Back pocket; Map 3) that encompassed both sides of the fault.

The Upper Member of the Amulet Formation is the host rock to the fault within

all study areas, including the C-shaft area, and is significant as the majority of the VMS

deposits within the Mine Sequence formed after its extrusion (Gibson et al., 1983). The

Upper Member consists of variably silicified andesitic flows that are generally massive,

aphyric, sparsely plagioclase porphyritic, flow laminated and columnar jointed. Within

the Mine Sequence the member has been subdivided into 4 flows with thicknesses of 80

to 150m, based on variations in grain size and vesicularity, and the occurrence of

vitrophyric breccias at flow contacts (Gibson et al., 1983).

Within the McDougall I fault map area the Upper Member is a single aphanitic,

non-amygdoloidal and sparsely (<5%) feldspar-porphyritic massive andesitic flow (Fig.

2.11 A) that is black in colour on fresh surface but weathers to multicoloured deep red,

brown, buff, white and light green coloured areas depending of the degree silicification

and chlorite/sericite alteration. A discordant, framework-supported breccia containing

angular, wispy and sub-rounded andesitic clasts within a finer clastic matrix is exposed in

the south-east part of the map. The contact between the breccia and massive flows is

sharp (Fig 2.11 D). Outcrops of silicified andesite immediately to the east and south of

F
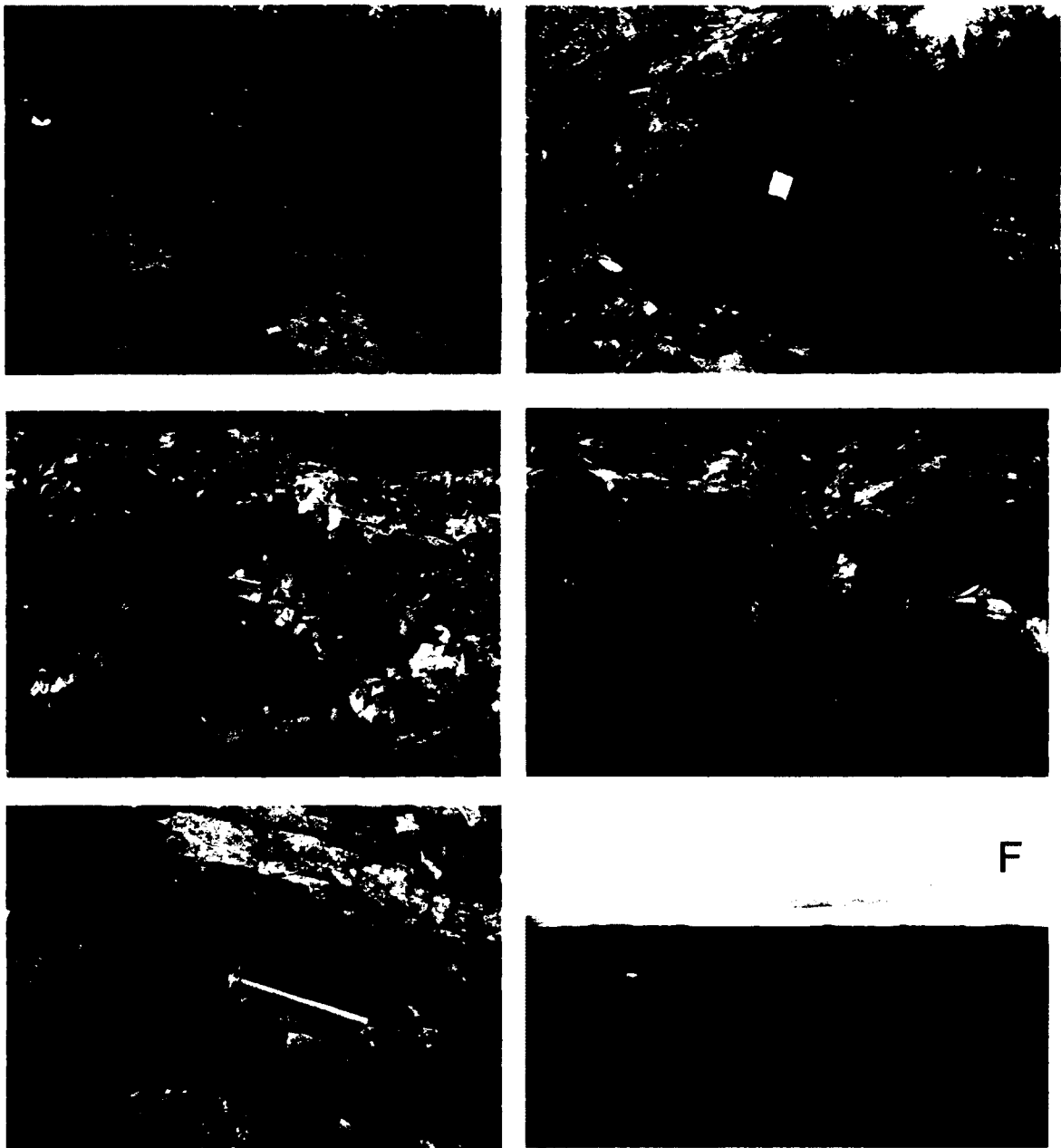
Figure 2.10 A) Outcrop photo (looking south) of the McDougall I fault that is exposed in two outcrops. The outcrops are separated by cover but a vertical cross-section view is exposed in the background. B) Vertical trenched cross-sectional view of the McDougall I faults main quartz-chalcopyrite veined zone. Sketch map in Fig. 2.15. C) Trenched outcrop view of the McDougall II fault. D) Northern vertical exposed surface of the McDougall II fault and the main sampling zone. Sketch map in Fig 2.16. E) Horizontal view of the McDougall II fault narrowing towards the north into a single un-mineralized fault. F) View of the reclamated Corbet shaft area from the McDougall II outcrop.

27
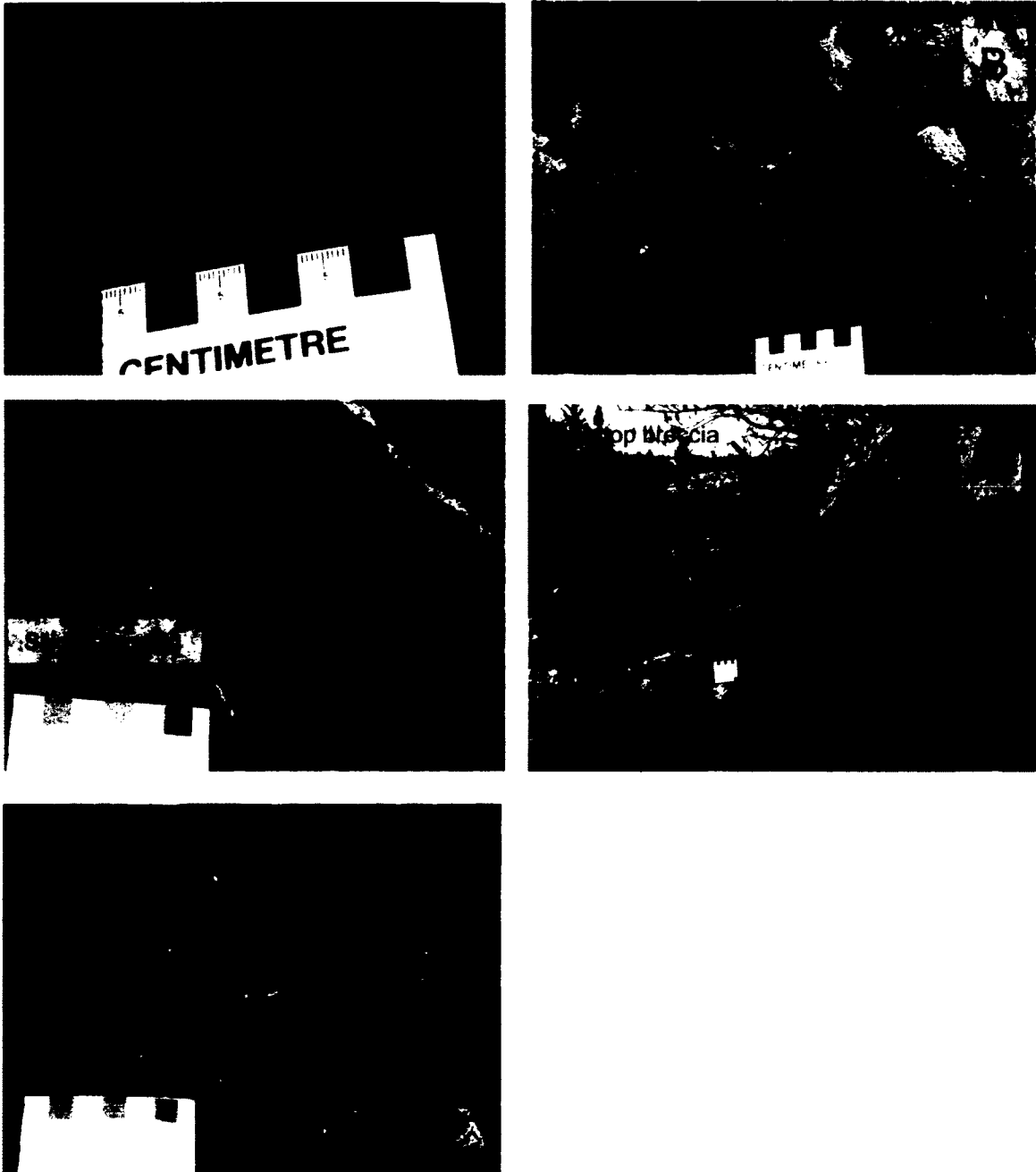
Figure 2.11 A) Aphanitic, andesitic flow of the Amulet Upper Member with trace pyrite blebs. B) Intense silicification of the Amulet Upper member andesite adjacent to the McDougall I fault. C) Sericite and Fe-chlorite alteration of the Amulet Upper member at McDougal I D) Flow top breccia with angular andesitic clasts at the McDougall I outcrop E) Breccia in the McDougall I fault with subrounded andesite clasts rimmed by quartz-sulfide veins.

the map area are crosscut by numerous rhyolite and andesite dikes that parallel the McDougall-Despina faults and breccia dikes that trend northeasterly (Gibson et al., 1983).

Within the McDougall II fault map area, the Upper Member is similar to that of the McDougall I map area, except that the massive andesitic flow contains 5 - 10% elongate amygdules filled by quartz with minor chlorite and pyrite (Fig 2.12 A); areas of the flow with 10% amygdules are more strongly silicified (Fig 2.12 B & C). A wedge-shaped, breccia dike containing angular fragments of the silicified andesite flank the main anastomosing quartz-sulfide zone of the McDougall II fault. The clasts range in size from 5cm to <0.5cm, constitute up to 80% of the dike and appear jig-saw fit to clasts rotated in close proximity to the main mineralized zone (Fig 2.12 E). The andesitic flow north of the McDougall II fault is overlain by a flow-top breccia. The flow-top breccia consists of hyaloclastite (Fig 2.13 A & B) that is sericitized and chloritized and cemented by quartz; flow tops are irregular and lobes of massive amygdaloidal andesite project up into the hyaloclastite flow breccia. The absence of a flow top breccia south of the McDougall II fault is interpreted to indicate movement along the structure, north side down, which is consistent with the sense of movement along the larger McDougall fault.

The McDougall I, II and C-Shaft faults have erratic variations in width over short distances, ranging from a simple fracture and increasing in width to a narrow single or anastomosing quartz-sulfide vein set ranging from 1 to 2m in width (Fig 2.14 A-E). The three faults have similar quartz-sulfide veining, and were subdivided into five vein types based on texture and degree of mineralization. The characteristic features of the veins are described in Table 2.1, which include petrographic observations, as macroscopic textural
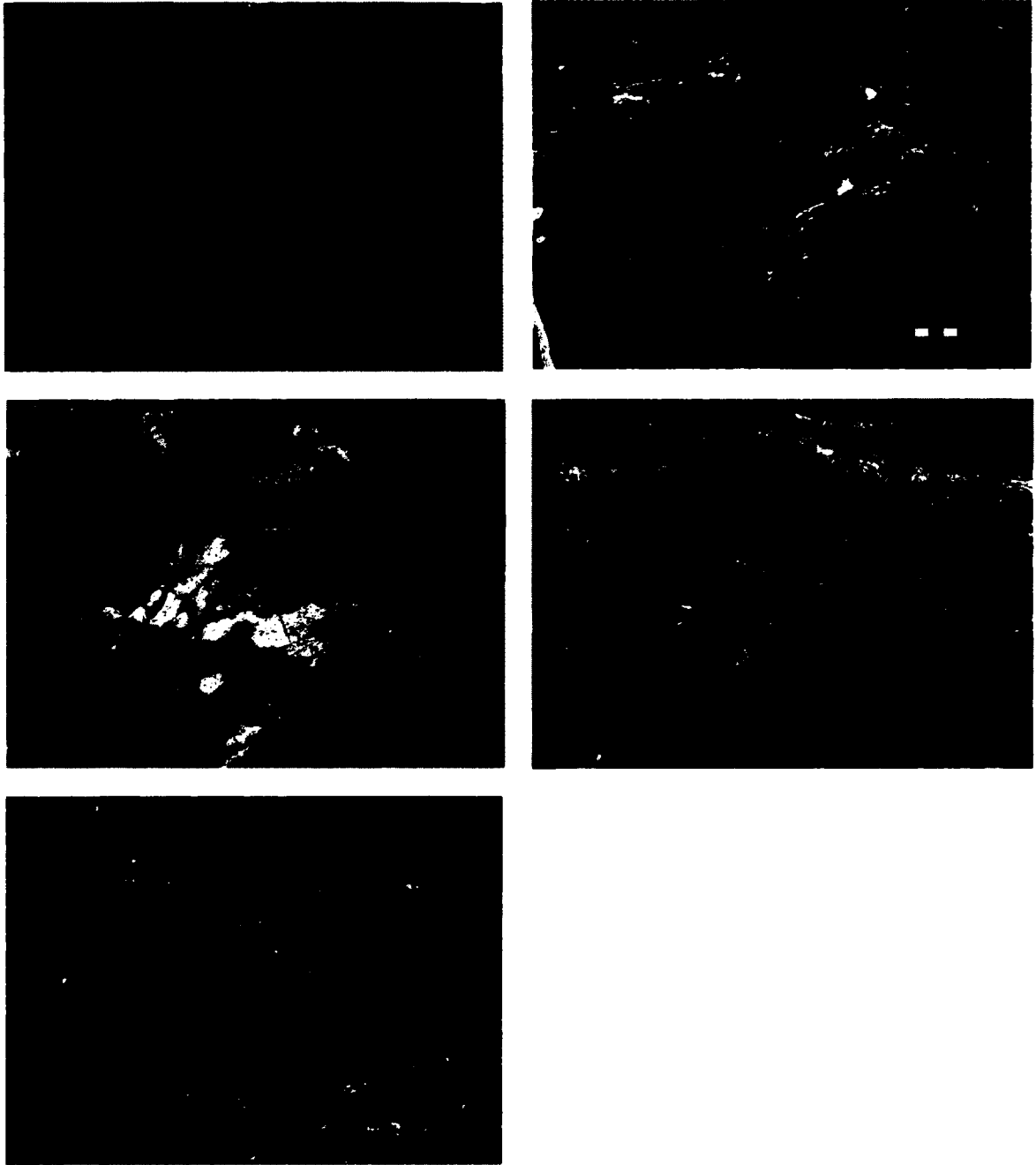
Figure 2.12 A) Quartz filled amygdules in a massive andesite flow of the Amulet Upper member south of the McDougall II fault, B) Intense silicification patch in massive andesite just south of the McDougall II fault, C) Closer view of the intense silicification patch in photo (b). D) Preferentially weathered angular andesitic clasts in a breccia zone within the McDougall II fault to the west of the trenched main mineralized zone. E) Autobrecciated jig-saw fit angular andesitic clasts along the margin to the McDougall II fault.
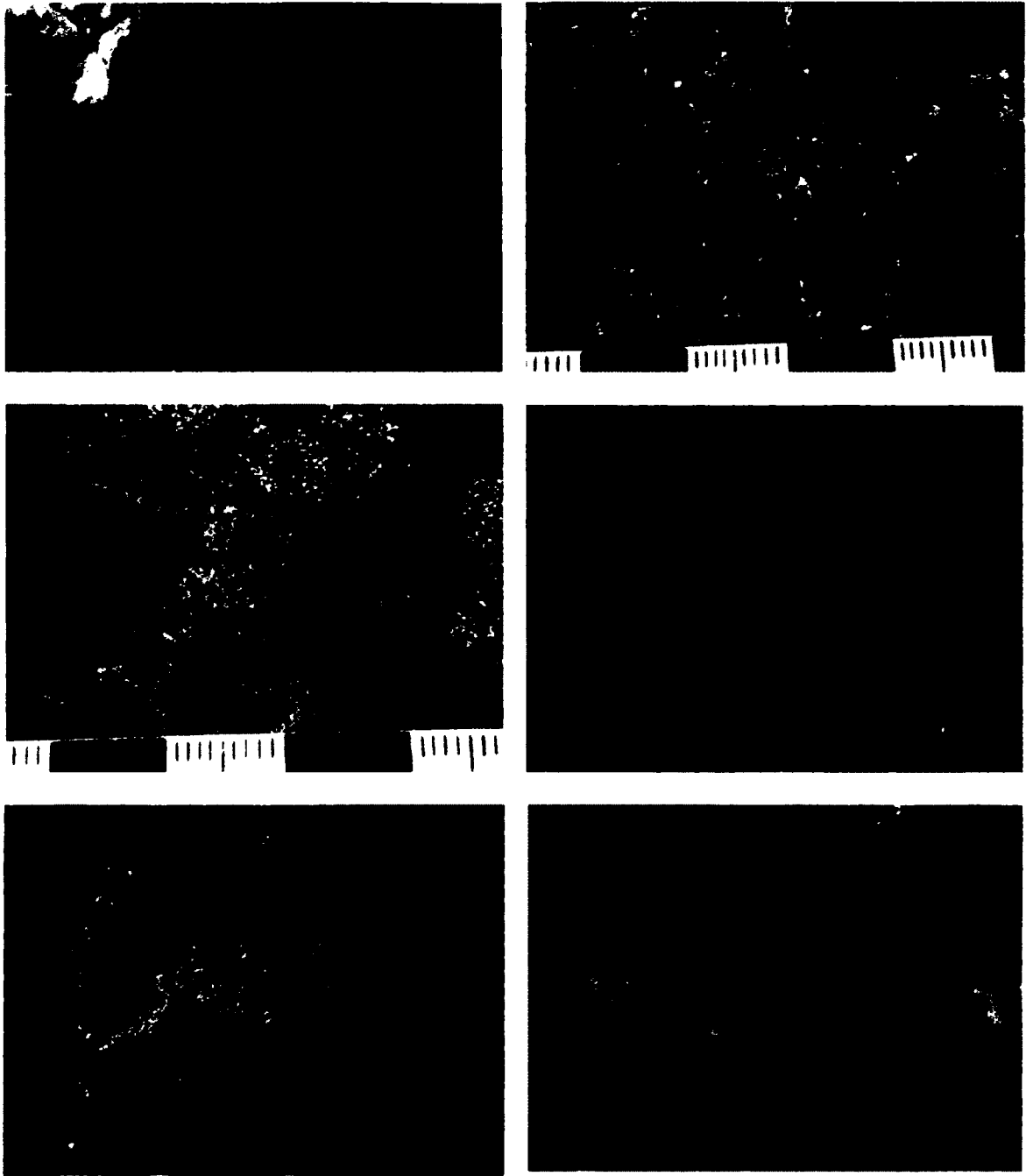
Figure 2.13 A) Flow top breccia in an andesite flow of the Amulet Upper member north of the McDougall II fault. B) and C) Quartz matrix hyaloclastite fragments within the flow breccia of photo A. C) Flow top breccia of "small" andesitic breccia fragments 1-5cm in width. D) Andesitic fragments 5-20cm in size within hyaloclastite matrix. E) Hyaloclastite with quartz matrix similar to B and C. F) Large silicified andesite fragments in a flow top breccia with a quartz matrix.
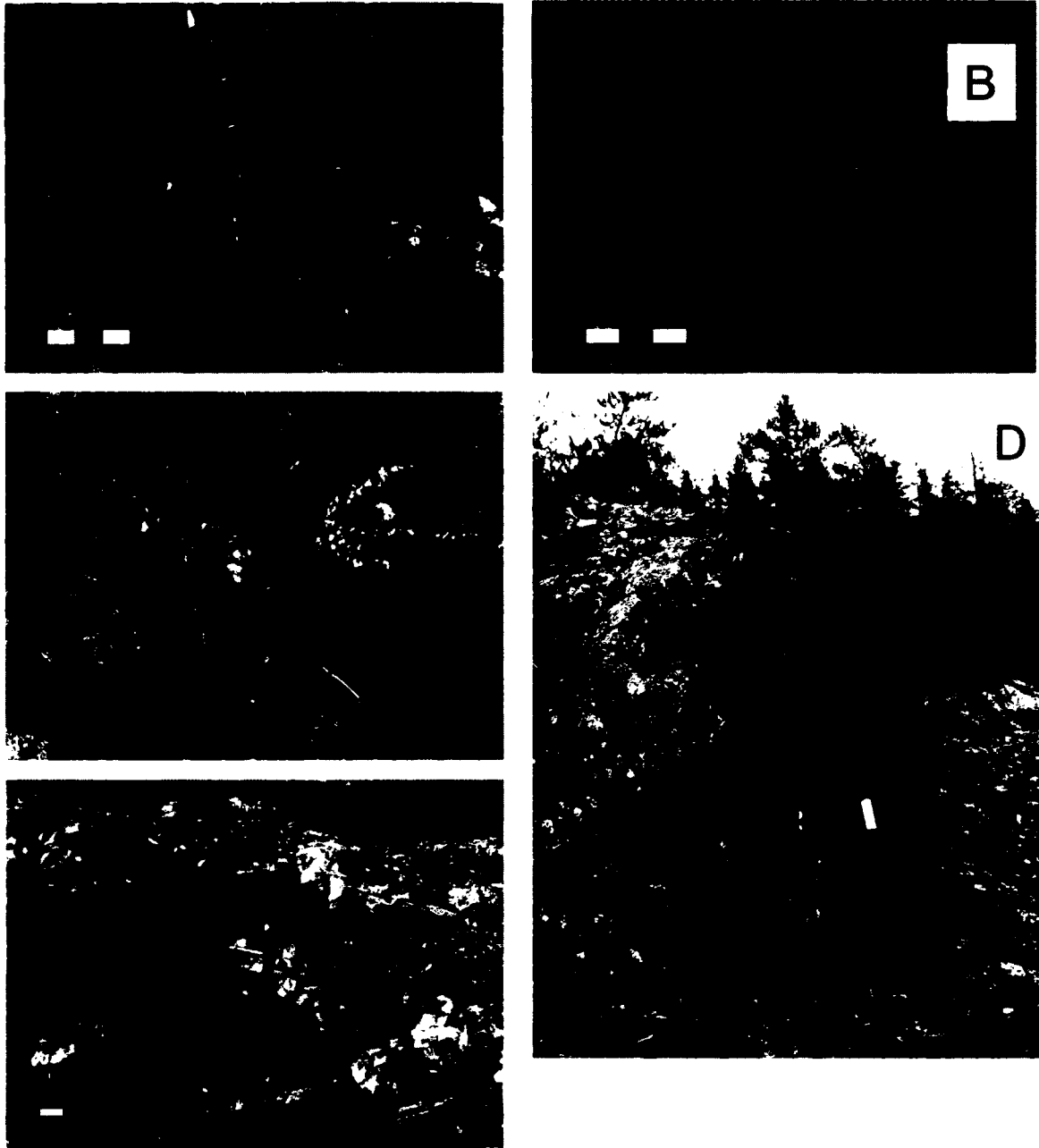
Figure 2.14 A) Gossans along the trend of the McDougall I fault. B) McDougall II fault east of the main mineralized zone. C) Small gossan zone within the C-shaft fault. D) Trenched zone at the McDougall I fault with 2 main mineralized veins exposed on the vertical surface. E) Exposed main mineralized zone within the McDougall II fault.

features were typically obscured by sulfide burn on outcrop exposures. Detailed maps of the McDougall I and II faults (Fig 2.15 & 2.16) also serve to illustrate the variety of veining across and along trend of the faults transitioning from Type I to Type V veins in relatively short distances.

The McDougall I fault locally trends at 274°, dips 68° to the NE, and is interpreted to lie along the main 310° trending main McDougall-Despina fault. On the vertically exposed outcrop exposure of the fault, 3 main mineralized (<20cm wide) Type II quartz-breccia veins are interconnected by minor, <5cm wide anastomosing Type II, Type I and barren Type IV quartz veins. The McDougall I fault is dominantly represented by Type II veins (Fig 2.17 B & C), veins that consist of deformed and fragmented comb and mosaic textured quartz fragments, healed by sulfides and microcrystalline quartz (Fig 2.17 A, E & F), that may have formed by movement along the fault during or prior to mineralization. A minor pyrite bearing "Type V" vein crosscuts chalcopyrite within the McDougall I fault (sample SZMDI-03-15) and is significant in that it contains minor electrum and disseminated sphalerite. Descriptions of vein types I to V are detailed in Table 2.1, which includes the criteria for defining quartz textures.

The McDougall II fault trends at 266°, dips 68° to the NW and is a splay of the main McDougall Fault. The fault appears as a fracture but increases in width to an anastomosing quartz-sulfide-wall rock breccia. The McDougall II fault dominantly consists of Type 1 veins (Fig 2.18 E) across the width of the fault and the andesitic fragments are derived from the immediate wall rocks (Fig 2.20 A-D). Type I veins (Fig 2.18 A) are locally separated by >50cm long, angular enclaves of the wall rock (Fig 2.18 D). Type II, III and IV veins are less common (Fig 2.18 B, C & F). In thin section,

quartz-sulfide veins typically appear as comb-textured quartz rimming angular brecciated

wall rock fragments (Fig. 2.19 A & B), with a centre of microcrystalline and mosaic

textured quartz and chalcopyrite (Fig. 2.19 C & D). Microcrystalline quartz appears

Amulet Andesite Formation
(southern outcrop) fault vein
exposure, geology sketch map,
Rouyn-Noranda, Quebec

Legend

■ Vein Type 1: Breccia Vein.

■ Vein Type 2: Brecciated quartz/
sulfide vein.
☐ Vein Type 3: Massive quartz vein.

■ Vein Type 4: >50% suflide veins.

■ Vein Type 5: Pyrite/Sphalerite veins.

■ Amulet Andesite

0   1m
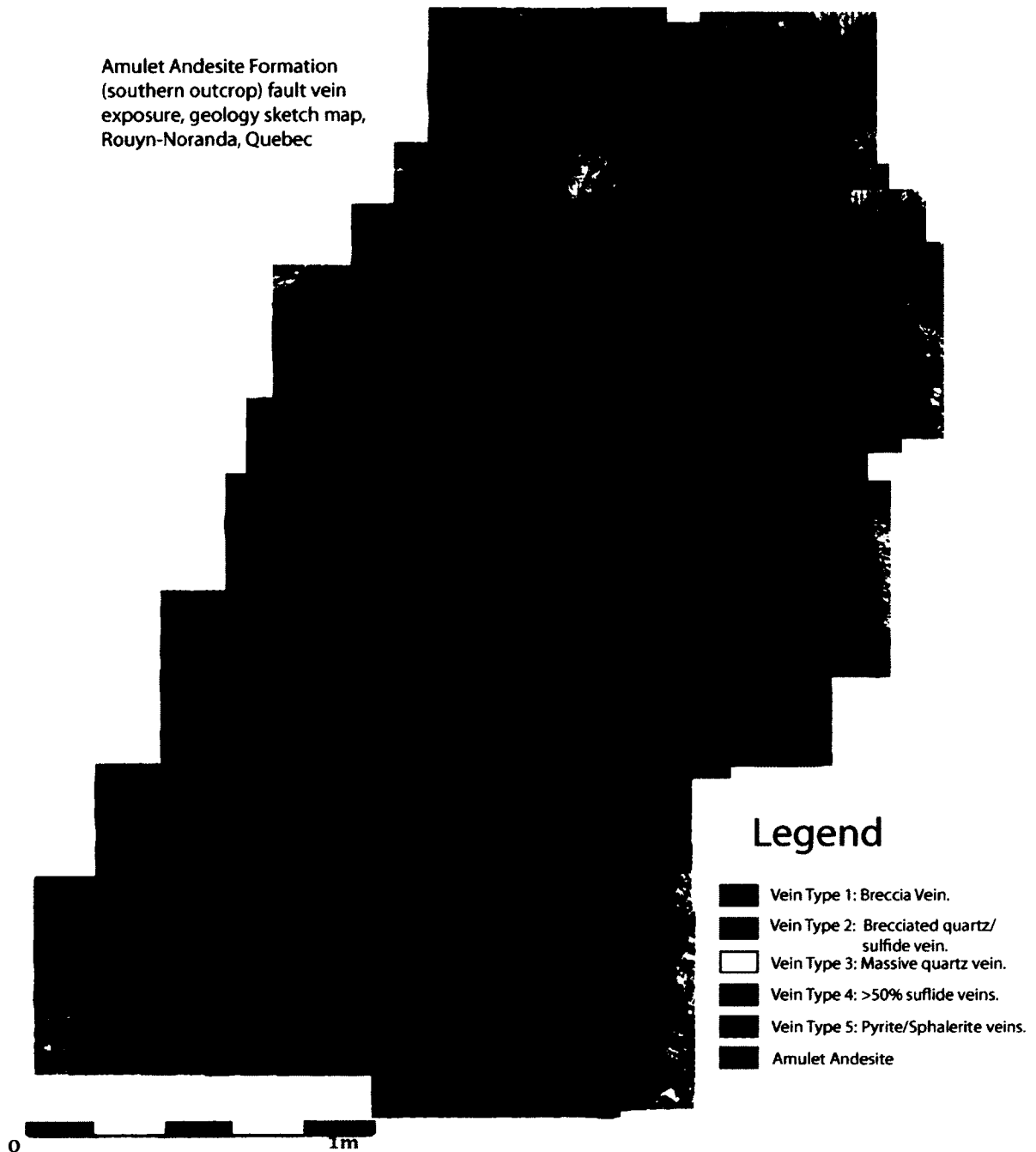
Figure 2.15: Sketch map of the McDougall I fault and vein system.

Legend

Marginal wallrock and wallrock breccia fragments.

Type I vein - Quartz breccia vein with <50% sulfides, <50% <5cm long wallrock breccia angular fragments.

Type IV vein - Quartz/sulfide veins with >50% sulfides.

Type III vein - Massive to comb textured quartz veins.

0   50cm
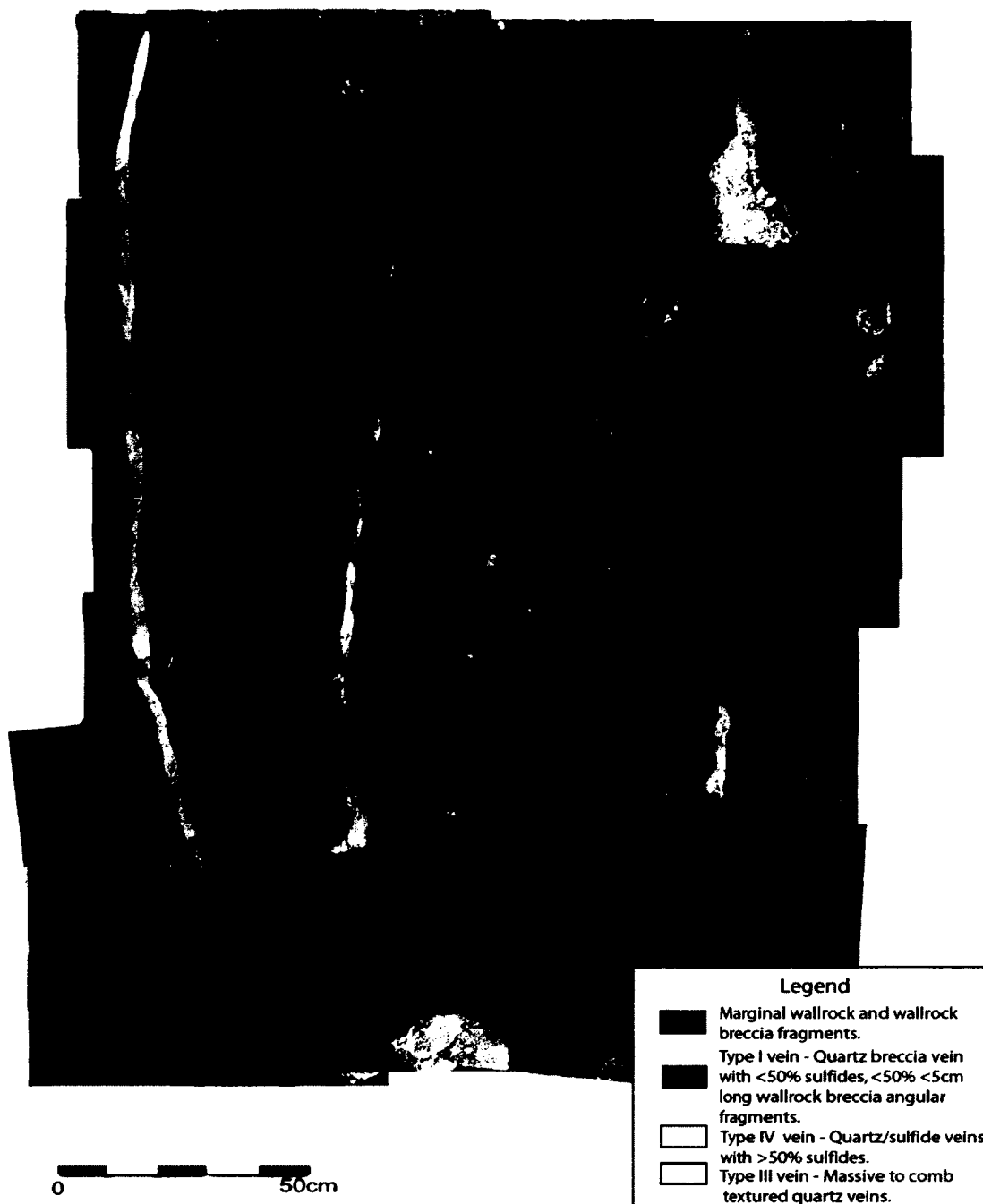
Figure 2.16: Sketch map of a trenched section of the McDougall II fault showing the vein system.
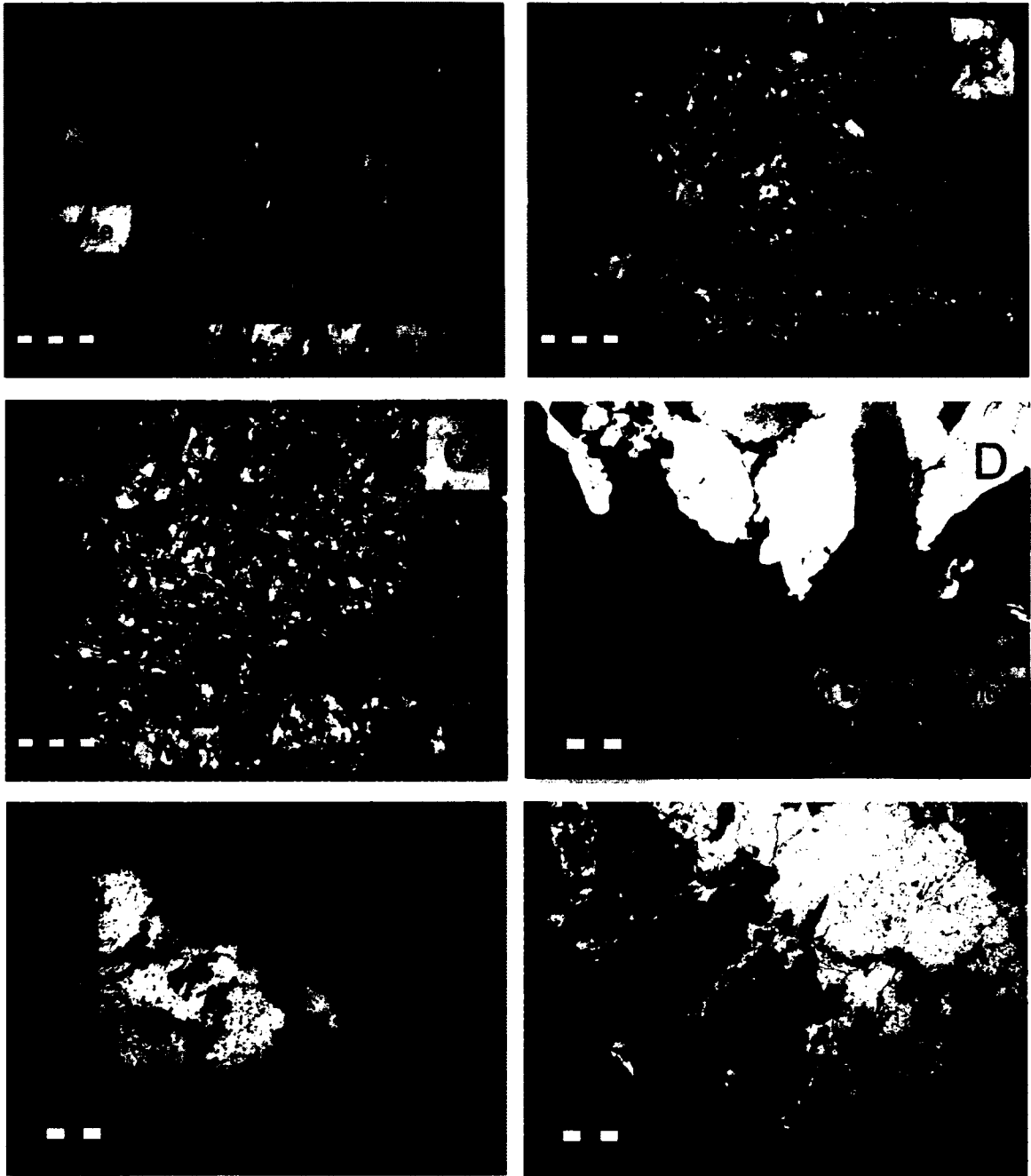
Figure 2.17 Photomicrographs of McDougall I quartz/sulfide veins A) Comb textured quartz centered by sulfide, chlorite and mosaic textured quartz in cross-polarized view. B) Brecciated quartz/sulfide veins typical of veins samples from the McDougall I fault, cross-polarized. C) Brecciated vein with wall rock breccia fragment, cross-polarized. D) Comb textured quartz rimmed/corroded by chalcopyrite, cross-polarized. E) Comb textured quartz centered by a massive chalcopyrite vein with minor veinlets penetrative to quartz/sulfide vein margins in plane polarized light of figure 2.17D. F) Comb textured quartz with interstitial massive chalcopyrite veins in plane polarized light.

36

	Sulfide/Oxide Mineralogy (overall avg. %)	Gangue Mineralogy (overall avg. %)	Breccia (overall avg. %)
ns ~20% of ·ansition) form Type II , that are 2- along large ɔlocks". ns ~80% of ns occurs the fault ar zones of I veins and ock ns 3 parallel ɟ portion of ic 1m long d of the fault.	*McD I*; ~5%; *McD II* ~14%; *C-shaft fault* <5% chalcopyrite in vein centers and penetrative between comb quartz. ±1-4% pyrite (mutual grains boundaries with chalcopyrite) ± tr-<1% covellite ± <1-1% FeOx within breccia fragments. ± <1-1% magnetite within andesite fragments. ± <1 sphalerite with chalcopyrite disease (only the C-shaft fault).	*McD I*; ~73% quartz: comb – 61%; mosaic – 7%; micro – 5% *McD II*; ~54% quartz: comb – 25%; mosaic – 18%; micro – 11% *C-shaft fault* – comb – 10-30%, mosaic - ~ 20%, micro – 15% ± 1-15% chlorite ± tr sericite	~0-5% and up to 40% andesite fragments (typically 2-50mm in length. 0.5-10% quartz ± tr – 4% but up to 28% chlorite ± <1% chalcopyrite ± <1% pyrite ± tr-1% FeOx ± <1% magnetite ± <1% muscovite
·ise~70% of fault. These ;ing and ss the ~2m ɪd consist of 3 ·eins that are hey transition	*McD I*; ~ 16%; *McD II* ~18%; chalcopyrite engulfing quartz within vein centers and as stringers extending to wall contacts. ± <1-5% up to 42% Pyrite	*McD I*; 55% quartz: comb – 8%; mosaic – 31%; micro – 16% *McD II*; 63% quartz: comb – 14%; mosaic – 31%; micro – 20% <1-15% up to 55%	~5-85% andesite fragments. ~5-50% quartz ± <1-25% chlorite ± <1-28% sericite ± <1-3% chalcopyrite ± 2% pyrite

t	Sulfide/Oxide Mineralogy (overall avg. %)	Gangue Mineralogy (overall avg. %)	Breccia (overall avg. %)
ıs with veins in the /. ɔrise <10% of ıt recognized ype II veins e 1 veins % is greater. ı	± tr sphalerite ± tr – 1% covellite ± tr visible gold ± <1% magnetite in breccia ± <1-5% up to 34% FeOx	chlorite locally ± tr muscovite	± <1-2% FeOx ±<1-1% magnetite
ṣ <5% of the s as masses at ithin the ins (eastern- nass in the ẹ vein). rs as a distinct vithin the nd forms contact with rock	No thin sections were prepared from these veins. Chalcopyrite masses are aggregates to interconnecting massive veins.	Appears to be only ~1cm wide irregular massive quartz fragments.	N/A

t	Sulfide/Oxide Mineralogy (overall avg. %)	Gangue Mineralogy (overall avg. %)	Breccia (overall avg. %)
prise ~5% of lt. Massive to connecting relatively ng" veins to ins on the fault. Also, as on point ost Type II irtz veins ff-shooting i structure. elongated s of massive I veins, e filling. A i wide vein ern wall rock mineralized d vug-like in i wide veins fault and as rom the main n. Veins do ut the	No thin sections were prepared of these veins. No sulfides were recognized from hand samples or at the outcrop.	100% quartz.	N/A

	Sulfide/Oxide Mineralogy (overall avg. %)	Gangue Mineralogy (overall avg. %)	Breccia (overall avg. %)
scutting erite. The 1- is only ection ie vein occurs all rock rn-most istomosing	~42% pyrite 5% chalcopyrite 5% FeOx tr sphalerite tr visible electrum	45% quartz <1% chlorite ~3% microcrystalline quartz	N/A

contemporaneous with chalcopyrite mineralization, as both are intergrown and occur

between comb-textured quartz crystals (Fig 2.19 A).
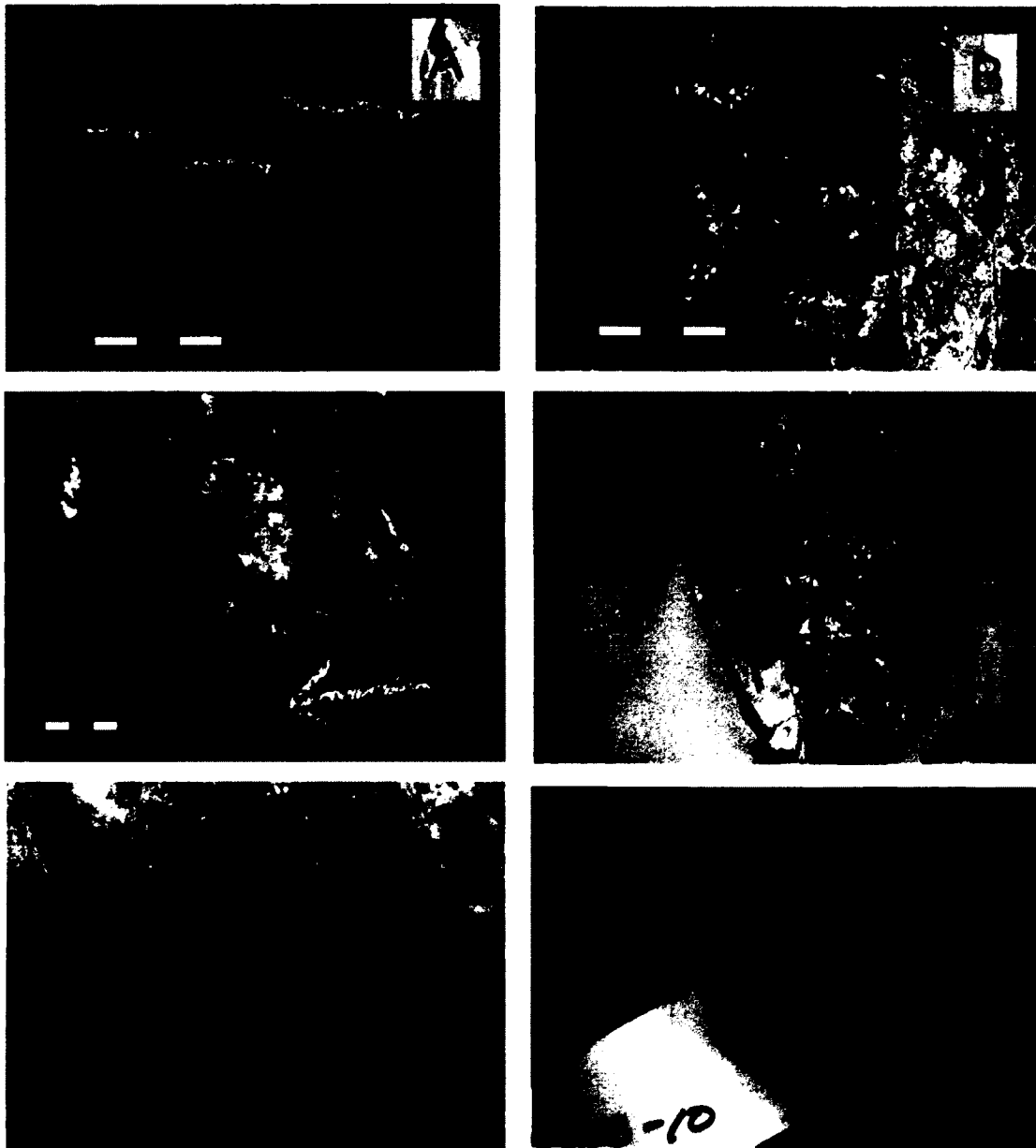
Figure 2.18 A) Outcrop photo of the breccia veins in the McDougall II fault. Yellow line indicates cross-sectional sample in Fig D. B) Photo of the McDougall II fault sulfide rich vein marginal to the breccia veins. C) Photo of the comb-textured quartz vein on the southern margin of the McDougall II fault. D) Cut sample of the breccia vein in the McDougall II fault typical of this texture. Yellow box indicates the location of Fig E. E) Closer view of the McDougall II fault breccia vein with comb-textured quartz rimming breccia wallrock fragments and later infilled by sulfides. F) Cut sample of the sulfide rich vein in the McDougall II fault.
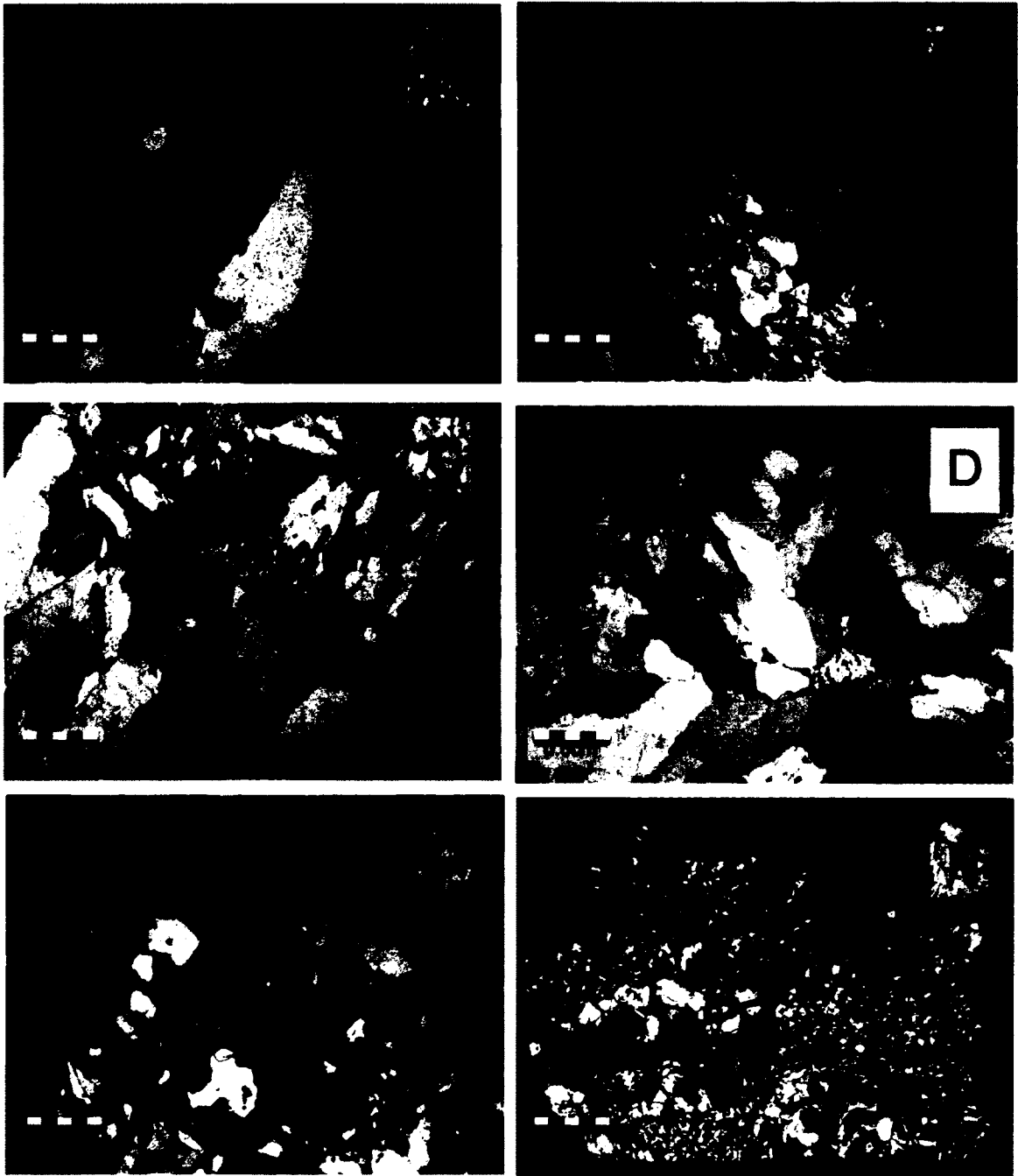
Figure 2.19 A) Photomicrograph of comb textured quartz mantling a wall rock (andesitic) fragments in the McDougall II fault. B) Andesitic wall rock fragments cemented by interconnecting comb-textured quartz and interstitial mosaic textured quartz. C) Comb-textured quartz with interstitial mosaic and microcrystalline quartz. D) Interstitial late infilling chalcopyrite within comb-textured quartz . E) Mutual grain boundaries of chlorite and chalcopyrite. F) Late oxidation in C-shaft fault sample rimming sulfides (indicated by arrows).

42
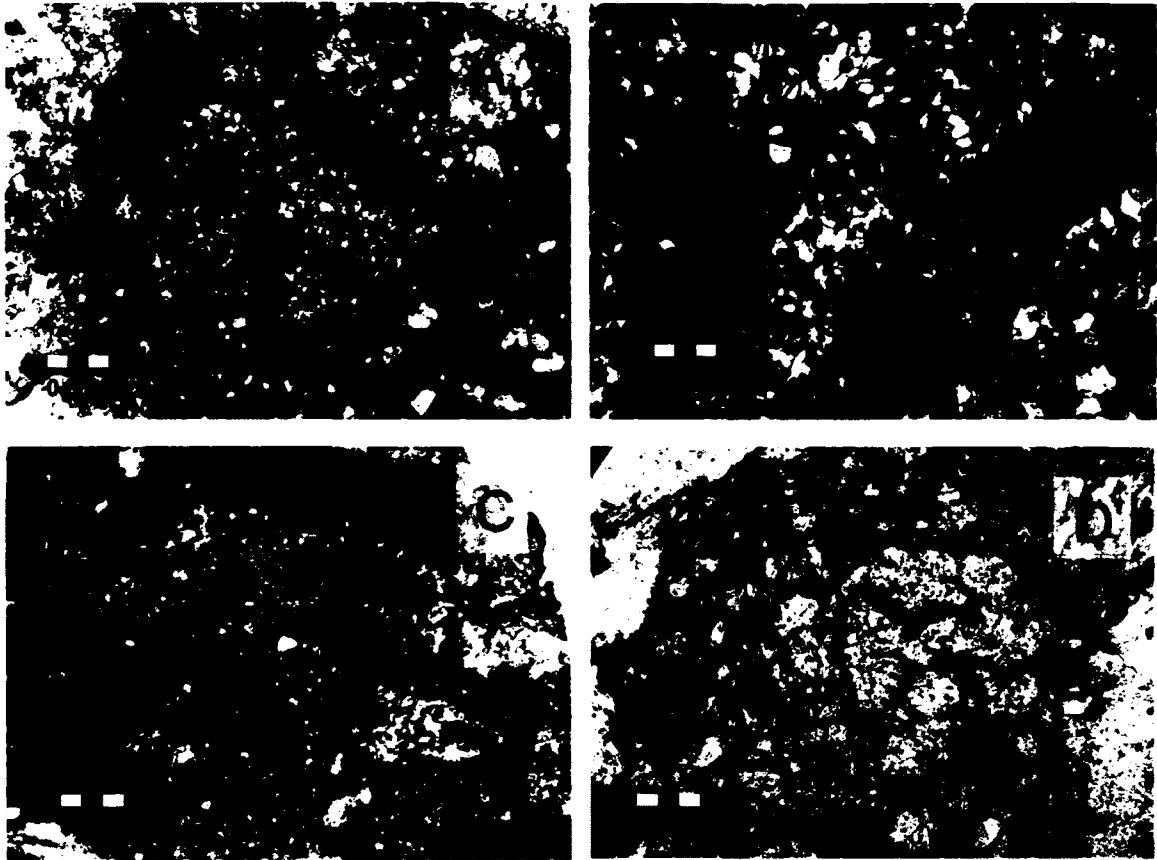
Fig 2.20 A-D) Photomicrographs of andesitic breccia fragments in quartz-sulfide veins of the McDougall II fault.

The C-Shaft Fault

The C-shaft fault trends between 250° and 282° and dips 80° to the N. The fault

ranges in width from <1cm and unmineralized, into randomly spaced single or

anastomosing mineralized veins <5cm in width with minor wall rock fragments to

intensely brecciated areas (10x2m) of anastomosing quartz-sulfide-wall rock veins. Vein

types are similar to the McDougall I/II faults, and are represented by both Type I and II

veins. Unique to the C-shaft fault is chalcopyrite disease within sphalerite, first

recognized by Farr (1984).

43

Alteration

Given that the timing of the McDougall and Despina faults has been shown to be synvolcanic, the most compelling evidence that these, and ancillary faults mapped in this study, are hydrothermal up flow zones is the occurrence of copper-rich mineralization within them. Furthermore, chlorite and sericite alteration of their adjacent volcanic rocks is identical in mineralogy and composition to that described for discordant alteration zones beneath the Noranda VMS deposits (Gibson et al., 1983; Franklin et al., 1995). Systematic sampling across these faults by Gibson et al., 1998, has shown that:

1. They are mantled by an inner zone of chlorite alteration and an outer, less well defined zone of sericite alteration.

2. The chlorite to sericite transition is also shown by litho-geochemical variation such that both the chlorite and sericite zones are depleted in CaO, and Na_2O, but the chlorite zone in more enriched in Fe_2O_3 and MgO and Cu, whereas the sericite zone is enriched in K_2O and Zn.

3. Both the chlorite and sericite alteration zones are characterized by $\delta^{18}O$ depletion (<6 ‰,) relative to the mean $\delta^{18}O$ composition of 7.4 ± 2‰ for the Noranda district. The former is within the range proposed by Cathles (1993) to define hydrothermal up flow zones.

Thus, the alteration surrounding the McDougall I/II and C-shaft faults are identical mineralogically, compositionally and isotopically to chlorite-sericite alteration associated with VMS deposits and is therefore synvolcanic alteration that is associated with copper-rich mineralization within these faults. This alteration and mineralization occurs deeper within a hydrothermal conduit, some 500-700m below the C-contact tuff

horizon (paleo-sea floor) and therefore provides the opportunity to examine fluid

inclusions in a deeper part of a hydrothermal upflow zone that is currently not available

for study in deposits on the modern seafloor or in any other Archean VMS system.

CHAPTER 3
FLUID INCLUSION DATA, ANALYTICAL TECHNIQUES, PROCEDURES, RESULTS AND INTERPRETATIONS

Introduction

In the context of ore deposit research, fluid inclusions may preserve fluids and volatiles present during mineralization or that may have traversed the deposits leaving no trace except for entrapment as inclusions within hydrothermal minerals (Roedder, 1979; Roedder, 1984; Shepherd, T., Rankin, A.H. and Alderton, D.H.M., 1985; Bodnar, R.J., 1994; Goldstein, R.H. and Reynolds, T.J., 1994; Wilkinson, J.J., 2001; Bodnar, R.J., 2003). The study of fluid inclusions provides almost all of the known information on the pressure, temperature, density, chemical (PVTX) and isotopic compositions of hydrothermal fluids, data that are generally unavailable through other techniques (Roedder and Bodnar, 1980). Analysis of fluid inclusions is used to improve our understanding of the source of ore fluids, the mode of ore transport and the potential change in composition enroute (Roedder and Bodnar, 1980). The greatest contribution of fluid inclusions to mineral exploration appears to be the feedback of fluid inclusion data into empirical and conceptual exploration models (Wilkinson, 2001), aiding in delineating mineralized zones, and eliminating vein systems that otherwise may appear attractive (Spooner, 1981). The current variety of analytical techniques to analyse fluid inclusions and their limitations have been summarized in detail by Roedder and Bodnar (1980), Roedder (1984), Shepherd et al. (1985) and Samson et al. (2003), with a number of these techniques effectively applied in this study.

The analytical techniques used to evaluate the PVTX properties of fluid inclusions in transparent quartz consist predominantly of fluid inclusion petrography and

microthermometry with subdivision of inclusion into fluid inclusion assemblages (FIAs). FIAs refers to a group of inclusions that were trapped simultaneously along a single fracture or within a single growth zone and are the finest discriminated groups of petrographically associated fluid inclusions (Goldstein and Reynolds, 1994; Goldstein, 2003). The inclusions within an FIA should have nearly identical characteristics in terms of bulk composition, density and homogenization behaviour (trapped as a single phase fluid), or show phase ratios governed by some immiscibility relationship (e.g., trapped on a solvus).

Fluid inclusion petrography and microthermometry in this study identified FIAs with PVTX properties indicative of a two component H_2O-NaCl system, although the depression of the eutectic temperatures below that expected for the H_2O-NaCl system indicates the presence of other cations. Even though these chemical systems are typically inferred by eutectic temperature measurements for complex multicomponent systems, quick and cost effective techniques can be applied to obtain bulk chemical compositions (Kontak, 2004). The use of breached inclusions, a technique whereby inclusions are opened so that the contents can be exposed for analysis using the scanning electron microscope (SEM) for single fluid inclusion compositional analysis as well as evaporate mounds analysis (SEM) for bulk fluid chemistry within specific parts of the quartz-sulfide veins examined, provided semi-quantitative data on fluid inclusion cation compositions. The use of Laser Ablations – induced coupled plasma mass spectrometry (LA-ICPMS) also provided quantitative but inconclusive data on single fluid/volatile inclusions and was attempted in order to evaluate the chemical systems, the differences between fluid inclusion assemblages, and the potential for sulfide transport with results

47

limited to Appendix 7. As some FIAs are CO_2 dominated, gas chromatography (GC) provides a bulk analysis of these potentially multi-component gas systems, while the application of the Gas Chromatography – isotope ratio mass spectrometry (GC-irms) produced data suggesting potential sources of CO_2 and simple hydrocarbons.

In this study sampling of fluid inclusion bearing material primarily focussed on quartz within the anastomosing quartz-sulfide veins of the McDougall I/II and C-shaft faults in order to compare similar mineralized synvolcanic fault structures at approximately the same stratigraphic interval (same unit) and vertical distance from VMS deposits formed on the paleoseafloor. The style and types of veining between the faults is relatively similar, and can be subdivided into five vein types based on their occurrence, mineralogy, texture and rare crosscutting relationships (Chapter 2). The majority of vein types sampled include types (I) & (II) quartz-chalcopyrite veins. Zones dominated by nearly massive but friable chalcopyrite are representative of type (III) veins, and were typically too oxidized to mount as thin sections of fluid inclusion bearing quartz. Type (V) veins consist of pyrite-quartz and only one vein was identified in thin section within the McDougall I fault where it appears to be either crosscutting type (II) veins as it surrounded by chalcopyrite, or it is a marginal vein or a pyrite mineralized brecciated fragment within the fault (Fig 2.15) that precipitated pre- chalcopyrite mineralization. Type (IV) barren quartz veins were excluded from the fluid inclusion analysis as they are paragenetically early and unrelated to the mineralizing fluids.

The exact location of samples collected from the McDougall I/II and C-shaft faults are illustrated in Figs 3.1, 3.2 and 3.3 respectively, with the exact location of microthermometric measurements documented in Appendix 1. Type (II) quartz-

chalcopyrite comprises the majority of the samples collected from the McDougall I fault,
with most samples collected from the westernmost and central quartz-sulfide vein within
the fault. The McDougall II samples are dominated by vein type (I), with samples
collected across the width of the fault. Although type (IV) veins were visible on the
margin of the McDougall II fault, they were not sampled for microthermometry. The C-
shaft fault samples include both type (I) and (II) veins and were collected from the 3
veins exposed in a vertical trenched portion of the fault (Fig 3.3). Samples from the
Corbet Deposit are from the #2 ore lens and were analyzed for a comparison of
stratigraphic variation of PVTX properties vertically within the hydrothermal system.

Fluid Inclusion Petrography

Standard petrographic techniques for the interpretation of fluid inclusion data
have been described by Roedder (1984), Shepherd et al. (1985), Channer and Spooner
(1994), Van den Kerkhof et al. (2000), Wilkinson (2001) and Goldstein (2003). The
interpretation of fluid inclusion microthermometry and additional data collected from
fluid inclusion analytical techniques is only possible when the textural relationship of the
fluid inclusion to the host mineral is established (Van den Kerkof et al., 2000). In order
to establish or determine this relationship, initial groupings of the fluid inclusions from
specific vein types were based on visual parameters prior to microthermometry, which
include their distribution, shape, size, type and vol % of vapour phase. The distribution
of fluid inclusions in this study is based on the criteria of Roedder (1984), who described
fluid inclusions as primary, secondary and pseudosecondary. A complete list of
observations for all fluid inclusions measured can be found in Appendix 4 with scanned
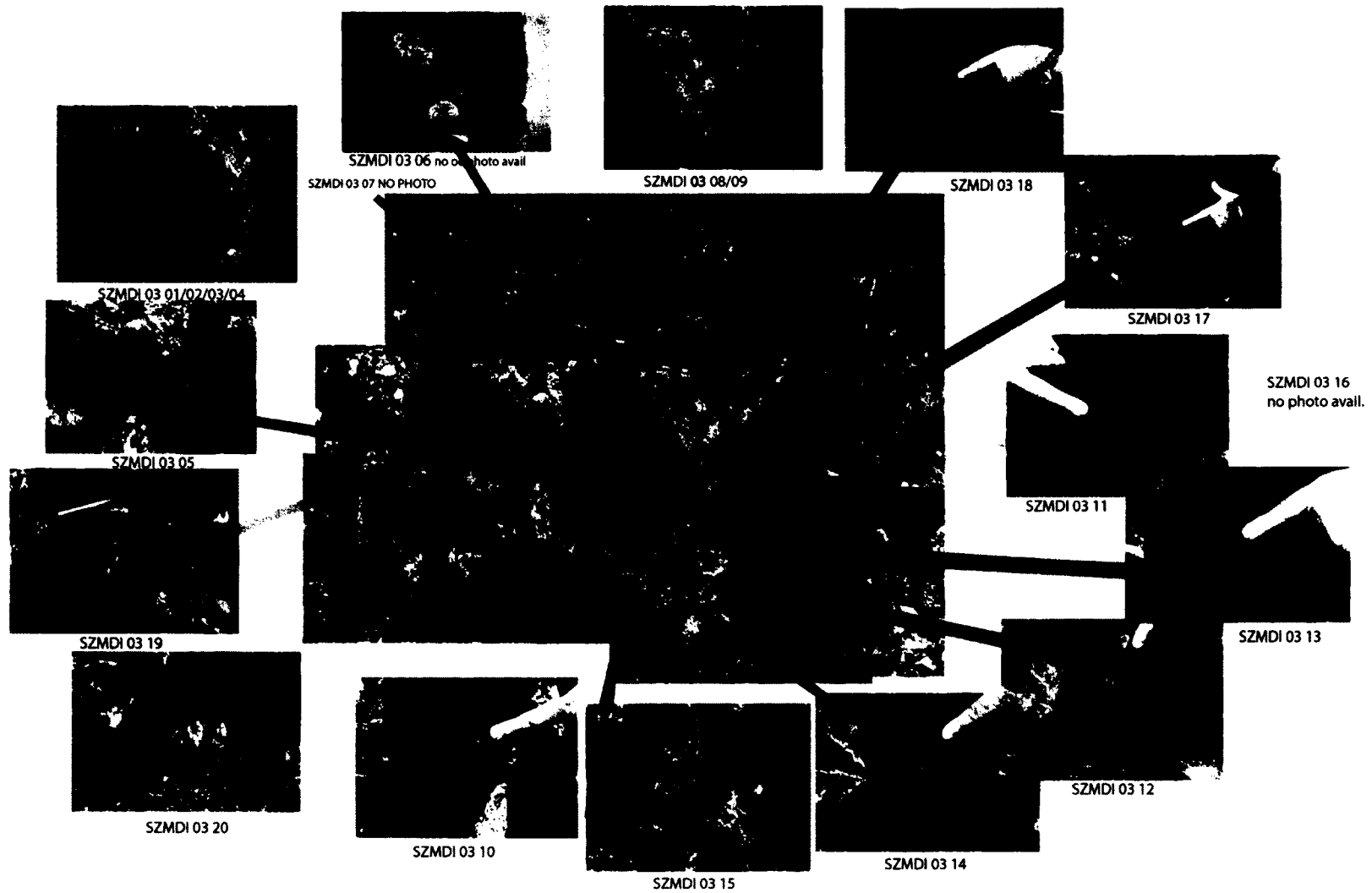
Figure 3.1 Location of samples collected from the southern outcrop of the McDougall I fault. Red hatched lines delineate samples collected from exposed surfaces. Samples delineated by orange, yellow and green hatched lines represent samples progressively taken deeper below surface.
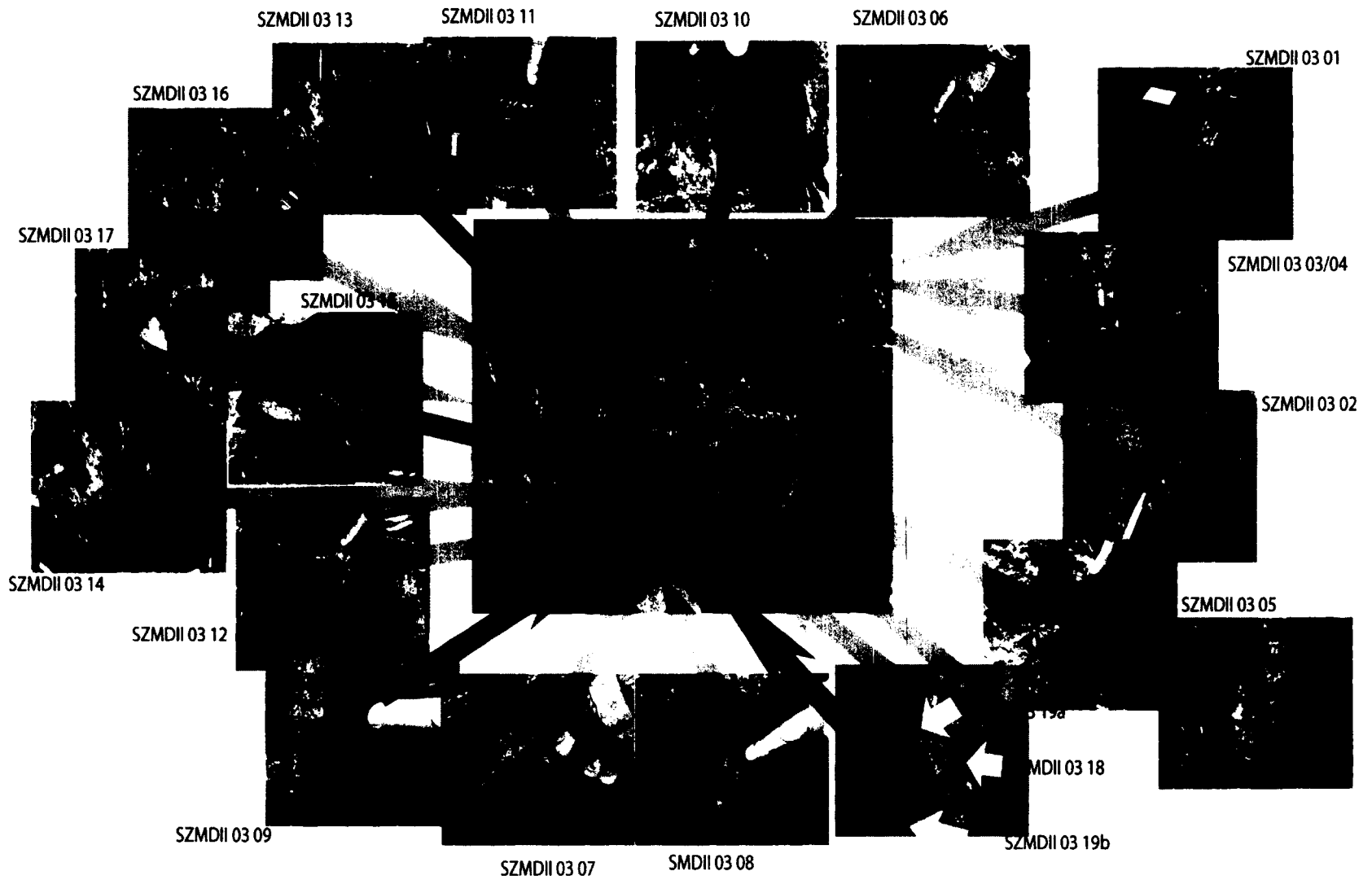
Figure 3.2: Location of samples from the eastern exposure of the McDougall II fault. Red hatched outline are surface samples, and hatched yellow delinaeate samples collected below the surface exposure.
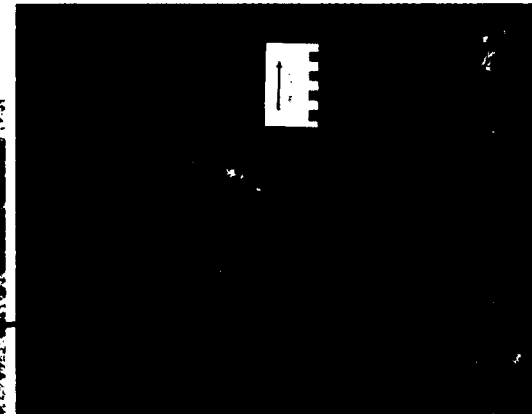
Samples: SZ-C-03-27 & SZ-C-03-28

Samples: SZ-C-03-29 & SZ-C-03-30

Figure 3.3: Location of samples from the trenched section of the C-shaft fault.

images of thin sections that correspond to measurement locations and images of FIAs in Appendix 3.

Fluid inclusions are abundant throughout quartz and are up to ~15 µm in size. Groups of fluid inclusions measured and grouped as part of the mineralization stage occur along trails representing healed fractures in contact with chalcopyrite or chlorite, whereas pre-mineralization fluid inclusions typically occur as pseudosecondary trails locally crosscutting growth zones in quartz or terminating in mosaic and comb textured quartz. Primary fluids inclusions are represented as isolated fluid inclusions, as clusters of inclusions, or along trails in a chevron shape, defining growth zones not visible in cross-polarized light in both mosaic and comb-textured quartz but visible in Hot-CL (Fig 3.4).

Further discrimination of fluid inclusion data to avoid visually indistinguishable re-equilibrated fluid inclusions (ie: necked, varying phase ratios) that resulted in greatly varying T_h/T_m values, was accomplished by eliminating fluid inclusion data that varied >15°C (T_h) and >1.5°C (T_m) as suggested by Goldstein and Reynolds (1994) within each petrographically determined subdivision (FIA plotted data). In addition, single anomalous inclusions that occurred elsewhere within the thin section or within the fault that shared similar T_h and T_m values with defined FIAs were excluded, as they were not trapped along a single fracture or within a single growth zone. The filtering of data using these criteria is the finest level possible for discriminating fluid inclusions forming in a dynamic hydrothermal system, and fall within an acceptable range for T_h and T_m (Goldstein and Reynolds, 1994).

The clustering of plotted fluid inclusions data using the FIA criteria, shows the consistency of this system even though heterogeneous fluids are being trapped. The

53

■ chalcopyrite   ⊙ Type 1-brine (2-phase)   ⟋ quartz grain boundary

■ microcrystalline quartz   ● Type 2-CO_2 + hydrocarbon

■ chlorite   ● Type 2-CO_2 + hydrocarbon + multisolid
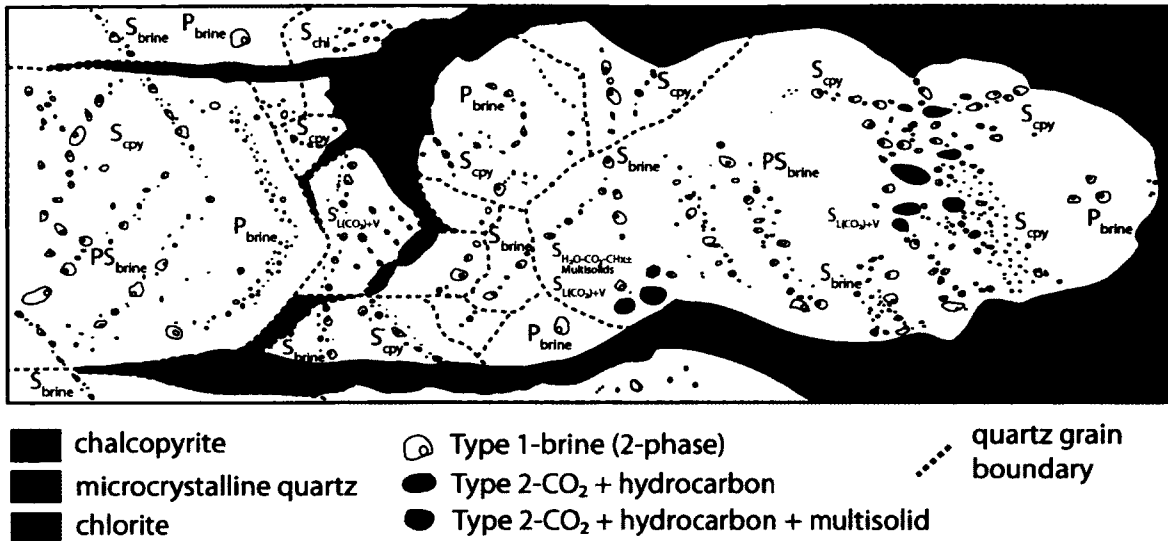
Figure 3.4: Inclusion Map (hypothetical) showing the textural relationship of FIAs in type 1 & 2 quartz veins. The earliest fluid inclusions consists of primary inclusions containing brine (P_{brine}) and vapor, occurring along growth zones in comb textured quartz, in fragments of mosaic textured quartz typically in chevron shaped plains and isolated inclusions suggestive of primary origin. Plains of pseudosecondary inclusions (PS_{brine}) do not intersect grain margins and have similar 2-phase characteristics to primary and secondary inclusions. Two secondary assemblages of S_{brine} inclusions occur either as long trails cross cutting grain margins or intersecting chalcopyrite margins (S_{cpy}). S_{brine} inclusions cross cutting grain margins was avoided since they are not conclusively coeval with mineralization. Secondary hydrocarbon assemblages ($S_{L(CO2)+V}$) only occur as plains intersecting chalcopyrite margins consisting of a $CO_{2(liq)}$, $CO_{2(vap)}$ and brine, with the vapor phase only visible when cooled below -10°C. and locally appear coeval with S_{cpy} assemblages (boiling). $S_{H2O-CO2-CHx±Multisolids}$ trails are in close proximity to chalcopyrite and consist of $CO_2/CH_{4(liq)}$, $CO_2/CH_{4(vap)}$, brine and multisolids of accidentally trapped sulfides and halite.

variability in each FIA likely reflects variable temperature-compositional conditions during entrapment (Loucks, 2000) or temporal variation as to the timing of initial closure of the inclusion (Goldstein, 2003). In a highly dynamic environment such as a VMS hydrothermal discharge conduit, oscillating fluid pressures, fluid mixing and boiling are expected to produce significant variations in composition (salinity) and temperature from one inclusion assemblage to another for a given fluid type, and from one fluid type to another.

54

Quartz in type (I), (II) and (V) veins is subdivided into three types, comb, medium-grained mosaic textured and fine-grained mosaic textured quartz. Comb textured quartz forms symmetrically on the wallrock and surrounding silicified wallrock fragments, whereas medium- and fine-grained mosaic quartz occurs interstitially within the centre of the vein. Due to the geometry of the veins, vertically oriented comb textured quartz terminations may appear as clusters of medium-grained, mosaic quartz forming mutual grain boundaries. Also, medium-grained, subhedral quartz surrounded by chalcopyrite exhibits no deformation or strain and may also represent fragments of comb-textured quartz or engulfed quartz terminations, potentially preserving primary fluid inclusions and secondary inclusions related to mineralization. Therefore, both comb textured quartz and mosaic quartz may be of the same generation and the fluid inclusion microthermometry does not discriminate between the two. In regards to primary growth zones identified within quartz, it should be noted that similar subhedral mosaic textured and comb textured quartz with primary inclusions were preserved in VMS mineralized veins at the Corbet deposit, as shown by "hot-cathode" CL analysis (Ioannou et al., 2004). The Corbet deposit is located 700m stratigraphically below the surface expression of the McD and C faults. Therefore, quartz growth zones potentially hosting primary inclusions in the McD and C faults with similar form to comb-textured quartz at the Corbet deposit, were interpreted to have undergone minimal effects by post-entrapment modification prior to "hot-cathode" CL analysis. In addition, the distance of the McD and C faults from the thermal aureole of the Flavrian and Lac Dufault intrusions avoids post-entrapment modification from re-heating by these intrusions.

Fluid Inclusion Types

Fluid inclusions were classified into 2 <u>basic</u> types: 1) Type I – aqueous, liquid-vapor (L-V), hosted by type (I), (II) and (V) quartz-sulfide veins within the McD I/II and C faults and; 2) Type II – aqueous-carbonic, hosted by type (I) and (II) quartz-sulfide veins within the McD I/II fault. The fluid inclusions have been further subdivided based on spatial mineral association (temporal sense) and proportion of phases present (FIA groupings) as described in greater detail in Table 3.1. Since further subdivision of fluid inclusions based on composition after microthermometry appears to be useless (Van den Kerkfoh et al., 2000), compositional subdivision based on eutectic temperatures of Type I inclusions was not attempted. The volumetric fraction of the aqueous liquid and vapour have been estimated at ambient room temperature using volumetric charts provided by Roedder (1984) and Shepherd et al. (1985). At room temperature the inclusions contain approximately 90 vol % brine and approximately 5-10 vol % vapor. Fluid inclusions with inconsistent phase ratios were avoided and were likely modified by necking or post-entrapment modification. Fig 3.5 A - Q are representative of Type 1 & 2 fluid inclusion with their sub-types.

Type I - Aqueous L-V ((H?)-trapped) inclusions occur as H_2O-NaCl +/- $CaCl_2$, KCl inclusions with a two phase assemblage at room temperature. Variability in shape and size within and between FIAs of Type 1 inclusions are random, generally appearing <10 microns in size and spheroidal. The majority of the inclusions appear small, generally ranging from 5-10um in diameter. The inclusions habit is sub-divided in Appendix 4, typically appearing as spheroidal (1a) or oblate (1b) as described by Shepherd et al. (1985), with rare negative crystals of cubic (1d) or hexagonal (1e) shapes

that may be of primary origin. Fluid inclusions occurring with excessively irregular

morphologies (1c) are rare and avoided as they may have necked during post-entrapment

modification. Three phase fluid inclusions appear elongated and spheroidal to oblate in

form with solid phases occurring as thin "sheet-like" (2c) or "spike-like" (2b) forms with
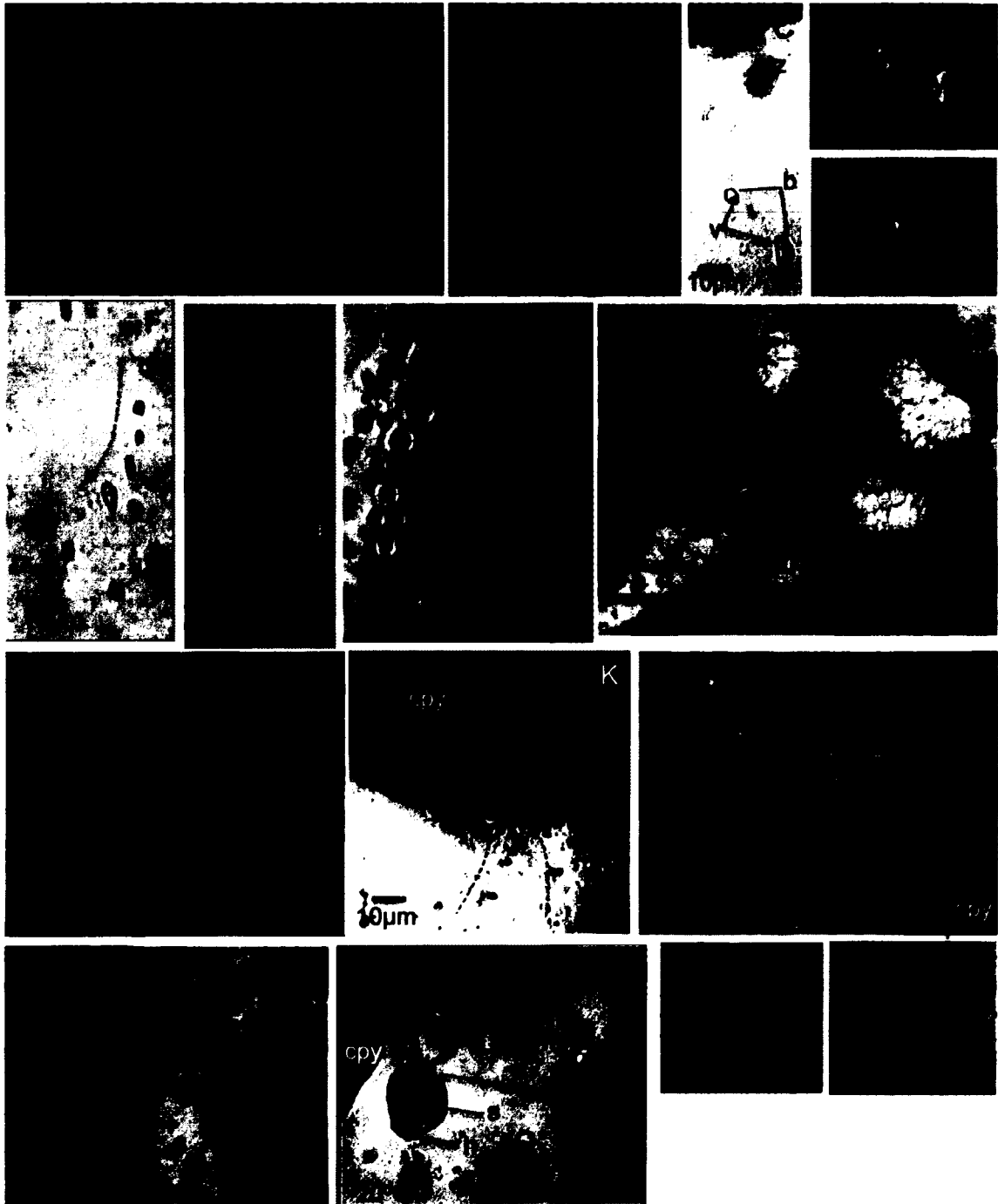
Figure 3.5: Photomicrographs (plane-polarized transmitted light) of representative brine (Type 1) and hydrocarbon (Type 2) bearing inclusion assemblages in quartz. Abbreviations: v vapor; b brine; liq liquid; h halite; s accidental solid; qtz quartz; cpy chalcopyrite. **a & b** Primary inclusions (Type 1-p) showing alignment in the inferred direction of quartz growth. Quartz growth direction is indicated by dashed arrows. **c,d & e** Primary 2-phase brine inclusions (Type 1-p) isolated or in clusters distal from trails or growth zones. These inclusions are suggestive of primary origin since evidence of trails or a secondary origin is also lacking. **f** A trail of pseudosecondary inclusions (Type 1-ps) terminating within the quartz grain and distal from quartz grain margins. **g & h** Secondary two phase brine inclusion (Type 1-s-chl) trapped along trails intersecting and tapering from chlorite grain margins. **i** Thin section photomicrograph showing the secondary chalcopyrite infiltrating fractures and spaces in the quartz vein. Secondary inclusions may potentially contain fluids that were precipitating sulfide minerals. **j & k** Secondary two phase brine inclusions (Type 1-s-cpy) in trails tapering from chalcopyrite margins. **l** Secondary two phase (Type 1-s-cpy) and three phase CO_2 bearing Type 2 inclusions (Type 2-s-L(CO_2)+V) tapering from chalcopyrite margins and cross cutting the quartz grain. Visible $CO_{2(vap)}$ only occurs when the temperature is below $-10°C$. **m** Type 2-s-L(CO_2)+V inclusions forming parallel fluid inclusions trails (bounded by the arrows) from infiltrating chalcopyrite along crystal margins. **o** Coexisting Type 2-s-L(CO_2)-V and Type 2-s-H_2O-CO_2-CH_4-CH_x±Multisolid in close proximity to chalcopyrite. Solid accidentals (chalcopyrite and halite) did not dissolve upon heating suggestive that quartz and sulfides was being precipitated when sulfides were also a saturated phase. This constrains Type 2 inclusions coeval with mineralization. **p & q** Type 2-s-H_2O-CO_2-CH_4-CH_x±Multisolid with accidental halite (possible boiling).

a green birefringence and they may represent trapped solid inclusions of

(muscovite/sericite, chlorite, halite or sylvite). Three phase fluid inclusions were also

recognized at the Corbet deposit, where they were described as spheroidal in habit and

containing a 5-10 vol% vapour phase and a 5-10 vol% halite crystal (2a) (Zubowski,

2001). The distribution of the inclusions measured appear isolated, aligned along growth

zones, as irregular (non array) densely packed clusters near sulphide minerals, as

discontinuous planar (pseudosecondary) arrays, and as secondary planar arrays

intersecting sulphide margins. Type I inclusions have been further subdivided based on

FIA groupings.

Type 2 – aqueous-carbonic+/-multisolid containing varying amounts of CO_2,

CH_4, N_2 and trace amounts of complex hydrocarbons (confirmed by gas chromatography;

see below and Appendix 6) were first identified based on eutectic temperatures measured below the CO_2 eutectic of -56.6°C with possible trapped multisolids. Type 2 inclusions have been subdivided into two FIA groupings based on the visibility of an aqueous phase at room temperature, with or without the presence of likely trapped multiphase solids, appearing as halite/sylvite crystals and rare sulfides. Fluid inclusions within both subsets range in size from 5-20μm in diameter, somewhat larger than Type 1 inclusions. All type 2 inclusions are oblate to equant to spheroidal in form (Shepherd et al., 1985), and are generally more rounded than Type 1 inclusions. Type 2 inclusions only occur as secondary inclusions that are spatially associated with chalcopyrite. The inclusions occurs as planar arrays located away from the contact of the host quartz with chalcopyrite and where the inclusion array terminates within single quartz crystals or completely traverse the quartz crystal along one plane, then it is completely surrounded by chalcopyrite. The CO_2 inclusions are rare within all vein types of the McD I and II faults (<5% abundance), but largely occurring within the McD II fault. There abundance may be underestimated due to the difficulty in recognizing CO_2 inclusions, which requires cooling to 5°C before the CO_2 vapor formed in what appears to be 100 vol% liquid filled inclusions. All type 2 inclusions appear to have formed cogenetically along well defined planar arrays, and locally occur in planar arrays with Type 1-s-cpy inclusions suggestive of immiscibility or boiling. Commonly, fluid inclusions along planar arrays suggestive of boiling appear to be almost pure CO_2 inclusions based on eutectic temperatures. Type 2-s L-V-multisolid inclusions with a halite crystal and Type 1-s-cpy inclusions with variability of phase ratios is suggestive of heterogeneous entrapment as inclusions

appeared rounded with no indication of necking (ie: micro-inclusions haloes around larger inclusions).

Fluid Inclusion Microthermometry
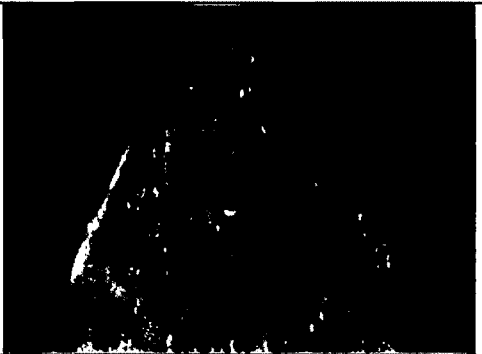
Analytical Procedure
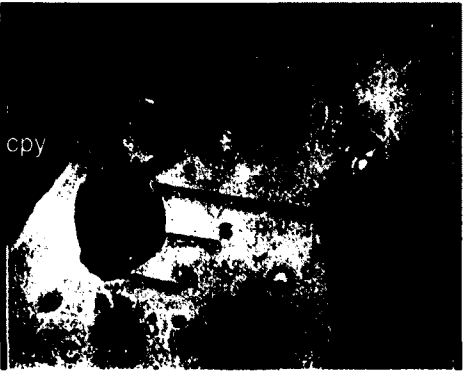
Standard microthermometric analytical techniques as described by Roedder (1984) and Shepherd et al. (1985) were applied using a Linkam THMS600 heating-cooling stage coupled to an automated controller on a Nikon Optiphot microscope at equipped with 5x, 10x, 50x and 100X long working distance Nikon objectives at Laurentian University. Additional microthermometry was also completed at the F.G. Smith Fluid Inclusion Laboratory at the University of Toronto using a Linkam THMS600 on an Olympus BX50 microscope equipped with 5x, 50x, 100x long working distance Olympus objectives. Accuracy of the measurements was ensured by calibration of the invariant triple point of CO_2 (-56.6°C), freezing point of water (0.0°C) and the critical point of water (374.6°C) of calibration quality synthetic fluid inclusions purchased from Bubbles Inc. of Blacksburg, Virginia, USA. The fluid inclusion stage was periodically checked against the standards and the uncertainty of microthermometric results is generally within +/-0.1°C (usually 0.2°C) with higher temperature phase transitions within +/- 5°C. All fluid inclusions were cycled as described by Collins (1979) and Shepherd et al. (1985) to ensure accurate final (Tm_{ice}) measurements.

Fluid Inclusion Types: Table 3.1

Type 1 Inclusions	Aqueous L-V -(H?)-trapped inclusions as $H_2O-NaCl\pm CaCl_2$			
Types	**Image**	**Relationship/Host**	**Location/Form**	**Comment**
Type 1-p Type -1 - Primary		Occur in comb and medium grained quartz, and inward from grain margins.	Forms planes in "chevron" shaped arrays, isolated as single inclusions or isolated as clusters on a single plane. Inclusions are two-phase at room temperature.	Inclusions have varying morphologies and relatively similar phase ratios (~5-10 vol%) vapor and sizes that range from 5-15μm. Inclusions are tentatively considered to be of primary origin, but an unequivocal primary origin could not be determined.
Type 1-ps Type – 1- Pseudosecondary		Located throughout comb and mosaic textured quartz and inward from grain margins.	Occur as discontinuous isolated planar arrays.	Inclusions have varying morphologies similar to primary inclusions with similar phase ratios and sizes. Inclusion trails generally consist of 5-10 measureable fluid inclusions within individual FIAs.

Type 1-s-cpy Type 1-secondary-chalcopyrite		These inclusions are associated with chalcopyrite mineralization, either within the centre of veins and in contact with mosaic-textured quartz or at the termination of comb-textured quartz. Trails of inclusions also occur in comb-quartz where chalcopyrite was penetrative along grain margins.	Trails of inclusions intersect quartz-chalcopyrite grain margins or occur as clusters of inclusions defining planar arrays away from the quartz-chalcopyrite grain margins.	Inclusions range in size and shape similar to primary and pseudosecondary inclusions. These secondary inclusions are significant because they are spatially associated with chalcopyrite and pyrite mineralization that is late within quartz veins, and their measurement is critical to understanding the fluid types within the veins.
Type 1-s-chl Type 1-secondary-chlorite		The inclusions are spatially associated with late chlorite that form mutual grain boundaries with chalcopyrite.	The inclusions form trails in contact with chlorite and occurs as clusters near the quartz/chlorite margin.	Similar in form and shape to Type-1-s-cpy assemblages. Some inclusion trails also appear to crosscut grain margin contacts of comb-textured quartz crystals.

Type 1-s-py Type -1-secondary-pyrite		The inclusions are spatially associated with mosaic-textured quartz in type V veins. (containing late crosscutting pyrite with minor sphalerite and gold).	The inclusions typically form planar arrays within quartz away from contacts with pyrite margin.	The form and shape is similar to other Type-1 inclusions but occur within FIA's having eutectic temperature below - 21.1°C (Na bearing systems). This eutectic temperature was modeled in the NaCl-CaCl$_2$ system. (Ca^{2+} cations).
Type 2 Inclusions	CO$_2$ bearing inclusions.			
Type 2-s-L(CO$_2$)-V Type 2-secondary-Liquid (CO$_2$) -Vapor		These inclusions are spatially associated with Type 1-s inclusions (boiling?) in mosaic-textured quartz that us surrounded by chalcopyrite. The inclusions also form trails associated with Type 2-s-H$_2$O-CO$_2$-CH$_x$±M inclusions or away from contacts with adjacent chlorite.	The inclusions appear subrounded and are typically <20μm in length. The FIAs form planar arrays away from contacts with chalcopyrite or chlorite.	Eutectic temperatures are close to -56.6°C, suggestive of minor dissolved gases other than CO$_2$. This assemblage at room temperature is liquid CO$_2$, requiring cooling to ~5°C before the vapor is visible. Likely ~5-10 vol% of an aqueous phase since it is only visible when occupying 20% by volume (Roedder, 1984) making salinity determination unattainable and causing slight variation in microthermometric results. Minor ice crystals formed on inclusion wall during cycling at low temperatures

Type 2 Inclusions	CO₂ bearing inclusions. *Con't*			

Type 2-s-H₂O-CO₂-CH±M
 	
Type 2-secondary-H₂O-CO₂-CHₓ ± Multisolids
		The inclusions occur along planes away from quartz-chalcopyrite grain margins in mosaic-textured quartz. They are typically associated with Type-1-s-cpy and Type-2-s-L(CO2)-V inclusions.
		Abbreviations: *vap* vapor; *h* halite; *s* accidental solid.
			Inclusions are <20μm in length with a CO₂ liquid phase (30-40 vol%), a CO₂ vapor visible upon cooling at 5°C w/~10-60 vol%, a pale green birefringent cubic halite/sylvite (possibly accidental) and a sulfide phase (also possibly accidental).	The eutectic temperature is depressed below -56.6°C suggestive of gases such as CH₄ and N₂ (GC – Appendix 6).
				  Solids are likely trapped due to their volume within inclusions.
				  The presence of halite/sylvite crystals within inclusions suggests that a brine and a hydrocarbon phase was present during entrapment.

Microthermometry Results

The microthermometric measurements are summarized within Tables 3.2 through 3.10, with complete microthermometric data and graphs provided in Appendix 4. Tables 3.2-3.5 represent all fluid inclusions measured where pairs of salinities and total homogenization temperatures were determined. Tables 3.6-3.9 contain a summary of FIAs, and Table 3.10 summarizes the CO_2 microthermometric data.

Type 1 - Liquid-Vapor (LV) Inclusions

All low temperature phase transitions were measured before the inclusions were homogenized to avoid decrepitation of Type 1 fluid inclusions and to determine eutectic temperatures. The fluid inclusions were significantly undercooled (-90 to -100°C) to ensure complete freezing and slowly heated to determine the eutectic temperature (Te_{ice}) of ice. Due to the small size of Type 1 inclusions and the difficulty in determining eutectic temperatures for low salinity fluid inclusions, Te_{ice} was not obtained for all inclusions. The eutectic melting temperatures (Te_{ice}) exhibits a "multi" modal distribution predominantly consisting of Te_{ice} measurements close to -21.2°C, between -40 to -55°C and as low as -65 to -75°C (Fig 3.6). Type 1 inclusions Te_{ice} suggest fluid compositions predominantly consisting of H_2O-NaCl-KCl, H_2O-NaCl-$CaCl_2$ or H_2O-NaCl-CO_2 mixtures with varying cation/solute proportions that would probably be best expressed using the H_2O-NaCl-$CaCl_2$ system from Oakes et al. (1990) due to the range of Te_{ice}. However, due to the size of Type 1 inclusions and the difficulty in distinguishing salt hydrates (hydrohalite), the bulk composition of the fluid modelled in a H_2O-NaCl-$CaCl_2$ system could not be determined and the salinity of the inclusions are expressed in
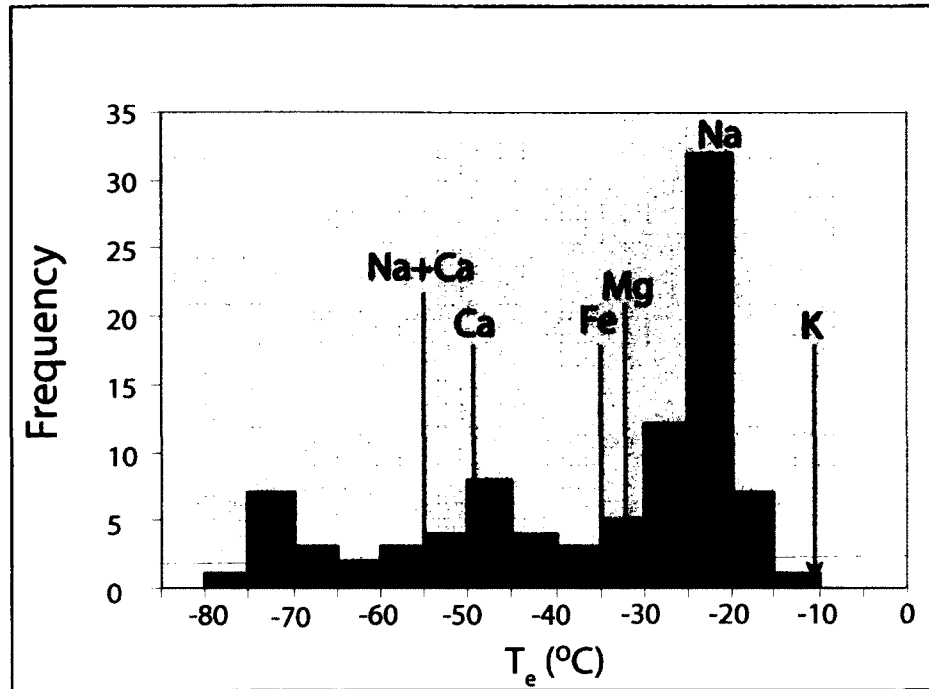
Figure 3.6: Frequency of eutectic temperatures of Type 1 inclusions. Cations indicate the exact "expected" temperature of first melting for the salt systems: K H_2O-KCl (-10.6°C); Na H_2O-NaCl (-21.2°C); Mg H_2O-$MgCl_2$ (-33.6°C); Fe H_2O-$FeCl_2$ (-35.0°C); H_2O-$CaCl_2$ (-49.5°C); Na+Ca H_2O-NaCl-$CaCl_2$ (-55°C). Shepherd, Ranking and Alderton, 1985.

terms of NaCl equivalent in the H_2O-NaCl system (ie: wt% NaCl equiv.). The summary

of fluid inclusion data in Appendix 4 also provides salinities expressed in terms of H_2O-

NaCl-$CaCl_2$ for comparison to the H_2O-NaCl system, calculated using an estimated

weight ratio as described by Ioannou (2004) in order to calculate the Oakes equation.

Microthermometric data from Appendix 4 expressed using the two systems described

above indicate that the variations in salinities between these two systems is minor, and

that the H_2O-NaCl system should be adequate to describe all inclusions. All Type I

inclusions were modelled in the H_2O-NaCl system using the V-X equation of Bodnar and

Vityk (1994) that was calculated using the MacFlinCor software provided by Baker

(2003). Fluid inclusions within assemblages suggestive of containing $CaCl_2$ were

modelled in the H_2O-$CaCl_2$+/-CO_2 using the V-X equation of Zhang and Frantz (1987),

and are noted in the data since inclusion with T_m values less than -21.21°C cannot be modelled in the H_2O-$NaCl$ system.

Type 1-p (primary) fluid inclusions within vein types (I) and (II) of the McD I and II faults exhibit similar behaviour during heating and freezing runs. Heating of these fluid inclusions after deep freezing produced eutectic temperatures between -73.5°C and -13.8°C. The temperature of final melting of ice (T_m) ranged from -7.8°C and -0.3°C for FIA inclusions within the McD I fault (Fig 3.8), indicating that salinities ranged from 0.5 to 11.2 wt% NaCl equiv. (individual FIA <2.0°C) using the equation of Bodnar and Vityk (1994). The McD II fault T_m ranged from -18.0 °C and -3.1°C (Fig. 3.9) indicating a similar overlapping range in salinities as in the McD I fault of 5.0 to 20.9 wt% NaCl equiv. (individual FIA <1.4°C). A small population of fluid inclusions within the McD I fault have a salinity range between 0.5 to 3.6 wt% NaCl equiv., suggesting that the sluggish final dissolution may not be ice but hydrohalite (Bodnar, 2003) and that some inclusions may contain a mixture of CO_2 (Hedenquist and Henley, 1985). All of the Type 1-p, L-V inclusions homogenize to the liquid phase with total homogenization (T_h) occurring between 125 to 244°C (individual FIA <15°C) within the McD I fault and between 171 to 227°C in the McD II fault (individual FIA <19°C). As shown in Figure 3.7, the trend of the T_h versus salinity is comparable for Type 1-p, L-V inclusions within both the McD I and II faults with only slightly lower T_h for the McD I fault and slightly higher T_m values for the McD II fault. Considerably higher salinities and lower temperatures were observed for Type 1-p (py) inclusions occurring within a crosscutting type (v) vein within the McD I fault. Type I-p (py) inclusions have eutectic temperatures between -76.6°C to -58.5°C indicating the presence of Mg/$CaCl_2$. The salinity range of

Type 1-p (py) inclusions is between 24.6 to 27.2 wt% $CaCl_2$ equiv. (individual FIA <0.6°C) and homogenization temperatures range between 88.3 to 130.3°C (individual FIA <11°C) (Fig. 3.8).

Pseudosecondary inclusions (Type 1-ps) within type (I) and (II) veins of the McD I and II faults overlap in total homogenization and salinity ranges with primary inclusions of similar chalcopyrite bearing veins. The temperatures of final ice melting within pseudosecondary inclusions of the McD I fault fall within the range of -12.9°C and -5.2°C, indicating salinities of 8.1 to 16.9 wt% NaCl equiv. (individual FIA <1.3). Upon further heating, the vapour bubble disappeared at temperatures between 138.6 to 192.9°C (individual FIA <8.3°C). Pseudosecondary inclusions within the McD II fault reached higher total homogenization temperatures in comparison to similar inclusions in the McD I fault with T_h values ranging from 150.6 to 210.9°C (individual FIA <13.5°C). The salinities of pseudosecondary inclusions within the McD II fault range from 5.6 to 14.3 wt% NaCl equiv. (individual FIA <1.6) and are similar to primary inclusions within the same fault. Pseudosecondary, Type 1-ps (py) inclusions within the type (V) vein of the McD I fault are consistent with the range of salinities in Type 1-p (py) inclusions, and overlap in homogenization temperatures by 20°C on either side of the T_h range of primary inclusions within this pyrite dominated vein. Final ice melting was observed at approximately -76.6 to -58.5°C, indicating that Type 1-ps (py) inclusions have salinities ranging from 24.7 to 26.6 wt% NaCl equiv. +/- $CaCl_2$/$MgCl_2$ (individual FIA <1.8). Homogenization to the liquid phase for these inclusions occurred between 87.8 to 156.8°C (individual FIA<7.8°C).

Secondary Type 1-s-cpy inclusions, in close spatial association with sulfides,

exhibit a range of eutectic melting temperatures (Te_{ice}) as low as -64.1°C, but

predominantly between -27.4 and -16.4°C. Although Tm_{ice} values were as low as -

48.9°C, no hydrohalite was observed during melting (T_m range ~-11.0°C to -5.0°C), thus

salinities were calculated using the $NaCl-H_2O$ system. The sulfide-related secondary

inclusions (Type 1-s-cpy) in the McD I fault are characterized by a salinity range of 7.8 to

15.1 wt% NaCl equiv. (individual FIA <1.5) for type (I) and (II) veins of the McD I fault.

The same Type 1-s-cpy inclusions all homogenized to a liquid phase upon heating

resulting in T_h values of 138.1-188.8°C. Similar Type 1-s-cpy inclusions within the McD

II fault have salinities ranging between 4.6 to 25.9 wt% NaCl +/- $CaCl_2/MgCl_2$

(individual FIA <4.5) and total homogenization temperatures ranging from 140.0 to

232.7°C (individual FIA <13.5°C). Fluid inclusions closely associated with chlorite

comprise only a small subset of the total secondary inclusions measured and were only

measured to confirm their similarities to chalcopyrite related inclusions due to their co-

precipitation. Type 1-s-chl inclusions in the McD II fault FIAs suggest a salinity range of

6.8 to 7.7 wt% NaCl equiv. and T_h of 177.2 to 210.8°C. Secondary inclusions in the

pyrite (type V) vein within the McD I fault have salinity and total homogenization ranges

that are similar to the pseudosecondary and primary inclusions within the same vein: 15.5

to 28.0 wt% NaCl equiv. +/- $CaCl_2/MgCl_2$ (individual FIA <3.3) and T_h of 80.8 to

144.2°C (individual FIA <8.6°C). Primary inclusions to secondary inclusions within the

quartz-pyrite vein of the McD I fault likely formed from the same fluid with no cooling at

the time of pyrite mineralization. Fluid inclusion data is plotted in Figures 3.7 – 3.11.

Figure 3.11 includes all individual inclusions measured including those used as FIAs and

illustrates the importance of indentifying FIAs demonstrated by the large scattered range in T_h vs. T_m data.

Type 2-s-L-V and H_2O-CO_2 ± Complex Hydrocarbons (CH) ± Multisolids (M)

In order to establish the volatile species within Type 2-s-L(CO_2)-V and Type 2-s-H_2O-CO_2-CH±M fluid inclusions, significant undercooling is required to induce complete freezing that occurred at temperatures between -100 to -105°C. Prior to reaching this temperature range, the phase changes recognized after the vapor bubble formed (generally at 5°C) from the L_{CO2} at room temperature is a slowly expanding inner bubble of vapor that reaches ~20-25 vol% maximum. Within Type 2-s-L(CO_2)-V inclusions, the vapor is surrounded by a high refractive index (darker grey) liquid CO_2 (~75-80% vol %) with no visible H_2O. Once the inclusion reaches the freezing temperature range, the CO_2 L-V collapses, expands to fill the entire inclusion with a higher refractive index solid CO_2. The freezing of Type-2-s-H_2O-CO_2-CH±M inclusions occurred within the same temperature range as Type-2-s-L(CO_2)-V inclusions but differs in that the liquid L-V CO_2 is surrounded by H_2O (~10-15 vol%), which petrographically defines the two assemblages within Type 2 inclusions. Upon freezing, the phase changes are similar to Type 2-s-L(CO_2)-V inclusions, the L-V CO_2 collapses and forms a CO_2 mass that is distinguished by a higher refractive index and appears fragmented, visually distinctive from the lower refractive solid H_2O. Upon heating, the $T_m(CO_2)$ temperature of Type 2-s-L(CO_2)-V inclusions ranges between -56.0 and -56.3°C, suggesting that these are likely pure CO_2 ($T_m(CO_2)$ -56.6°C) inclusions with the T_m variation representing instrumental error. In comparison, Type 2-s-H_2O-CO_2-CH±M inclusions have a $T_m(CO_2)$

between -58.2 to -60.9°C, indicating that additional volatile species are present, most likely CH_4 and N_2 (GC data - see below).

The freezing point depression within both carbonic fluid inclusion assemblages indicates that one assemblage has a bulk composition of primarily pure CO_2, whilst the other contains CO_2 with other volatile species. With further heating beyond the $T_m(CO_2)$ of Type 2-s-L(CO_2)-V inclusions, the phase change associated with the final melting of the ice along the inclusion wall ($T_m(ice)$) could not be identified due to the difficulty in identifying a low volume % of H_2O and a thin meniscus along the inclusions wall. Hence, the salinity of Type 2-s-L(CO_2)-V inclusions could not be determined, but are assumed to be low since Type 1-s-cpy inclusions within the same assemblage have salinities of ~10.8wt% NaCl equiv. and T_h of ~180°C equivalent, and visually appear to be phase separated (or heterogeneous entrapment). The homogenization of Type 2-s-L(CO_2)-V inclusions always homogenized to the liquid at temperatures between 5 to 14.1°C (mostly 10-14.1°C), which corresponds to a density of between 0.83-0.89 g/cm^3. Type 2-s-L (CO_2) -V inclusions were used to obtain compositional data on CO_2 bearing inclusions using LA-ICPMS analysis, as a result total homogenization measurements ($T_h(tot)$) were not acquired due to potential decrepitation at high temperatures.

Similar to Type 2-s-L (CO_2) -V inclusions, Type 2-s-H_2O-CO_2-CH±M inclusions are relatively rare and larger than Type 1-s-cpy inclusions, forming secondary trails extending inwards from the quartz-chalcopyrite grain margins. The morphology of Type 2-s-H_2O-CO_2-CH±M is distinctive in that they have a rim of H_2O (~30-50 vol %) with a higher refractive index, around liquid CO_2, with or without a trapped halite or pyrite/chalcopyrite crystals. Microthermometric measurements were obtained from only

14 Type 2 inclusions due to the difficulty in locating and identifying these inclusions as CO_2 vapor is not visible until cooled (at ~ 5°C). As previously suggested, the melting temperature (T_mCO_2) indicates other dissolved gases are present in addition to CO_2. Upon further heating, the salinity of Type 2-s-L (CO_2) –V inclusions were determined by final melting of clathrate (T_mclath) (4.5-9.6°C), indicating salinities in the range of 0.8-21.3wt% NaCl equiv. Homogenization of the CO_2 (T_hCO_2) to a liquid occurs within the 9.0 to 21.1°C temperature range, with a carbonic density of 0.83 to 0.90 g/cm^3. Continued heating of these inclusions typically resulted in decrepitation of the inclusion (T_d) between temperatures of 294.3 - 477.4°C with one individual assemblage reaching temperatures of 600°C (2 inclusions) without decrepitating. Dissolution of the halite and pyrite-chalcopyrite amorphous solids did not occur before decrepitation was reached and this suggests these may be trapped solids. Only one inclusion within Type 2-s-L- (CO_2) –V reached a total homogenization to a liquid (T_htot) at a temperature of 331°C and decrepitated at 341.7°C. Interpretation of the fluids inclusion data is located at the end of Chapter 3 in order to incorporate additional fluid inclusion analysis results.

Table 3.2: Fluid Inclusion Data Summary of all measured inclusions[1].

Group	Inclusion Type	T_h (°C)	T_m (°C)	Salinity[3] (wt% NaCl equiv.)	Salinity[4] (wt% NaCl+CaCl$_2$)	Density (g/cm^3)
McD I						
Fault	Type 1-p	177.1 ± 46.3	-4.81 ± 3.7	7.1 ± 4.8	7.6	0.943
		(125.4:378.9)	(-15.9:-0.3)	(0.5:19.4)	(0.7:18.6)	(0.5:1.06)
		n = 40	n = 40	n = 40	n = 40	n = 40
	Type 1-p[2]	317.3 ± 263.2	-33.3 ± 5.6	26.5 ± 1.3	26.1 ± 1.1	0.94 ± 0.3
	Ca^{2+} system	(88.3:598.1)	(-43.5:-26.5)	(24.7:28.7)	(24.2:27.3)	(0.58:1.2)
		n = 7	n = 7	n = 7	n = 7	n = 7
	Type 1-ps	169.9 ± 36.7	-6.7 ± 4.1	9.58 ± 4.9	10.0 ± 4.6	0.96 ± 0.07
		(114.7:282.6)	(-18.9:-0.8)	(1.3:21.6)	(1.7:20.4)	(0.75:1.10)
		n = 24	n = 24	n = 24	n = 24	n = 24
	Type 1-ps[2]	158.8 ± 76.4	-23.6 ± 8.8	22.4 ± 4.7	22.2 ± 4.6	1.1 ± 0.07
	Ca^{2+} system	(66.8:259.5)	(-33.0:-12.5)	(16.3:26.5)	(16.2:26.6)	(1.07:1.22)
		n = 6	n = 6	n = 6	n = 6	n = 6
	Type 1-s-cpy	167.1 ± 24.8	-7.9 ± 4.0	11.1 ± 4.4	11.1 ± 3.8	0.98 ± 0.06
		(117.4:244.6)	(-20.5:-1.0)	(1.7:22.7)	(2.1:21.3)	(0.82:1.12)
		n = 28	n = 28	n = 28	n = 28	n = 28
	Type 1-s-cpy[2] Ca^{2+} system	111.9 na	-29.5 na	25.6 na	25.4 na	1.2 na
		n = 1	n = 1	n = 1	n = 1	n = 1
	Type 1-s-chl	173.4 ± 16.9	-5.3 ± 5.5	7.45 ± 7.3	7.7 ± 7.2	0.95 ± 0.06
		(150.4:189.9)	(-12.2:-0.4)	(0.66:16.2)	(0.8:15.9)	(0.90:1.0)
		n = 4	n = 4	n = 4	n = 4	n = 4
	Type 1-s-py[2]	114.4 ± 24.5	-24.1 ± 11.7	22.2 ± 5.0	21.8 ± 5.0	1.1 ± 0.06
	Ca^{2+} system	(80.8:144.2)	(-40.3:-11.6)	(15.5:28.1)	(15.4:27.6)	(1.1:1.2)
		n = 7	n = 7	n = 7	n = 7	n = 7

[1] The top number corresponds to the mean (± corresponds to 1σ), bracketed numbers give the range, n = the number of measurements, Th = temperature of homogenization, Tm = temperature of final ice melting.

[2] Tm measurements were below -21.1 °C suggestive of other cations. Measurements were calculated using the H$_2$O-CaCl$_2$ ± CO$_2$ system of (Bodnar et al., 1989). Possible Ca^{2+} bearing inclusions were plotted with NaCl-H$_2$O inclusions given that the difference between the two systems is insignificant.

[3] McD I Fault salinity data above -21.1°C in the NaCl-H$_2$O system calculated using Brown and Lamb, 1989.

[4] McD I Fault salinity (eq. NaCl-CaCl$_2$) determined using the NaCl-CaCl$_2$-H$_2$O system of Oakes et al. (1990). (X_{NaCl} = 0.27, Pyrite vein X_{NaCl} = 0.08) where X_{NaCl} is the molar volume.

Table 3.3: Fluid Inclusion Data Summary of all measured inclusions[1].

Group	Inclusion Type	T_h (°C)	T_m (°C)	Salinity[3] (wt% NaCl equiv.)	Salinity[4] (wt% NaCl+CaCl$_2$)	Density (g/m^3)
McD II Fault	Type 1-p	188.9 ± 48.8	-6.8 ± 3.4	10.0 ± 3.8	10.5 ± 3.8	0.9 ± 0.09
		(68.5:413.7)	(-18.0:1.3)	(1.8:20.9)	(-3.2:19.7)	(0.41:1.12)
		n = 92	n = 92	n = 92	n = 92	n = 92
	Type 1-p[2] Ca^{2+} system	135.5 ± 20.3	-25.5 ± 0.8	24.3 ± 0.3	23.4 ± 0.4	1.15 ± 0.01
		(122.3:158.9)	(-26.2:-24.6)	(24.0:24.6)	(23.0:23.7)	(1.14:1.16)
		n = 3	n = 3	n = 3	n = 3	n = 3
	Type 1-ps	177.4 ± 20.4	-7.3 ± 2.5	10.7 ± 3.0	11.3 ± 2.6	0.97 ± 0.03
		(131.9:221.9)	(-15.5:-2.0)	(3.3:19.0)	(4.1:18.2)	(0.90:1.10)
		n = 48	n = 48	n = 48	n = 48	n = 48
	Type 1-ps[2] Ca^{2+} system	145.3 ± 0.2	-23.6 ± 3.3	22.4	23.6	1.14 ± 0.01
		(145.1:145.4)	(-25.9:-21.3)	NA	NA	(-1.15:-1.1)
		n = 2	n = 2	n = 1	n = 1	n = 2
	Type 1-s-cpy	177.6 ± 27.3	-8.0 ± 3.5	11.3 ± 3.9	11.8 ± 3.5	0.98 ± 0.05
		(106.1:236.7)	(20.0:-1.0)	(1.7:22.3)	(2.2:20.8)	(0.85:1.12)
		n = 86	n = 86	n = 86	n - 86	n = 86
	Type 1-s-cpy[2] Ca^{2+} system	169.7 ± 97.5	-29.9 ± 4.6	25.6 ± 1.3	25.4 ± 1.7	1.1 ± 0.1
		(63.7-427.8)	(-36.9:-22.2)	(22.9:27.4)	(23.5:27.6)	(0.86:1.23)
		n = 13	n = 13	n = 13	n = 9	n = 13
	Type 1-s-chl	185.1 ± 16.8	-6.0 ± 2.8	9.0 ± 3.4	9.8 ± 3.0	0.9 ± 0.03
		(166.4:210.2)	(-11.1:-4.3)	(6.8:15.1)	(7.8:15.0)	(0.92:1.00)
		n = 5	n = 5	n = 5	n = 5	n = 5

[1] The top number corresponds to the mean (± corresponds to 1σ) , bracketed numbers give the range, n = the number of measurements, Th = temperature of homogenization, Tm = temperature of final ice melting.

[2] Tm measurements were below -21.1 °C suggestive of other cations. Measurements were calculated using the H_2O-$CaCl_2$ ± CO_2 system of (Bodnar et al., 1989). Possible Ca^{2+} bearing inclusions were plotted with $NaCl$-H_2O inclusions given that the difference between the two systems is insignificant.

[3] McD II Fault salinity data for eutectic temperatures above -21.1°C in the $NaCl$-H_2O system calculated using Brown and Lamb, 1989.

[4] McD II Fault salinity (eq. $NaCl$-$CaCl_2$) determined using the $NaCl$-$CaCl_2$-H_2O system of Oakes et al. (1990). (X_{NaCl} = 0.13) where X_{NaCl} is the molar volume.

Table 3.4: Fluid Inclusion Data Summary of all measured inclusions[1].

Group	Inclusion Type	T_h (°C)	T_m (°C)	Salinity[3] (wt% NaCl equiv.)	Salinity[4] (wt% NaCl+CaCl₂)	Density (g/m³)
Corbet Deposit	Type 1-p	185.6 ± 45.4	-7.1 ± 4.7	10.0 ± 4.5	10.5 ± 4.5	0.95 ± 0.07
		(104.2:283.6)	(-17.5:-1.7)	(3.6:19.3)	(3.6:19.3)	(0.76:1.05)
		n = 19	n = 19	n =19	n = 19	n = 18
	Type 1-p Ca^{2+} system	163 ± 17.1	-26.3 ± 5.7	NA	23.4 ± 2.5	0.91 ± 0.02
		(150.9:175.1)	(-30.4:-22.1)		(21.7:25.2)	(0.90:0.92)
		n = 2	n = 2		n = 2	n = 2
	Type 1-ps	217.0 ± 55.0	-6.3 ± 3.8	8.7 ± 4.6	9.8 ± 3.9	0.90 ± 0.07
		(108.8:350.6)	(-20.6:-2.2)	(3.6:22.8)	(4.5:21.0)	(0.74:1.01)
		n = 39	n = 39	n = 38	n = 39	n = 39
	Type 1-ps Ca^{2+} system	212.1 ± 60.4	-34.9 ± 3.2	NA	26.8 ± 1.1	0.84 ± 0.10
		(170.9:281.5)	(-38.0:-32.0)		(25.8:28.0)	(0.73:0.90)
		n = 3	n = 3		n = 3	n = 3
	Type 1-s-cpy	200.1 ± 51.4	-8.8 ± 6.2	11.1 ± 6.6	11.7 ± 5.7	0.93 ± 0.09
		(109.7:297.7)	(-24.1:-2.1)	(3.42:22.7)	(4.3:20.4)	(0.77:1.06)
		n = 39	n = 39	n = 38	n = 39	n = 38
	Type 1-s-cpy Ca^{2+} system	177.0 ± 9.3	-29.3 ± 2.5	NA	24.8 ± 0.9	0.89 ± 0.01
		(167.3:188.7)	(-31.0:-26.0)		(23.6:25.6)	(0.88:0.91)
		n = 4	n = 4		n = 4	n = 4

[1] The top number corresponds to the mean (± corresponds to 1σ), bracketed numbers give the range, n = the number of measurements, Th = temperature of homogenization, Tm = temperature of final ice melting.

[2] Tm measurements were below -21.1 °C suggestive of other cations. Measurements were calculated using the H_2O-$CaCl_2$ ± CO_2 system of (Bodnar et al., 1989). Possible Ca^{2+} bearing inclusions were plotted with $NaCl$-H_2O inclusions given that the difference between the two systems is insignificant.

[3] Corbet Deposit salinity data for eutectic temperatures above -21.1°C in the $NaCl$-H_2O system calculated using Brown and Lamb, 1989.

[4] Corbet Deposit salinity (eq. $NaCl$-$CaCl_2$) determined using the $NaCl$-$CaCl_2$-H_2O system of Oakes et al. (1990). (X_{NaCl} = 0.09) where X_{NaCl} is the molar volume.

Table 3.5: Fluid Inclusion Data Summary all measured inclusions[1].

Group	Inclusion Type	T_h (°C)	T_m (°C)	Salinity[2] (wt% NaCl equiv.)	Salinity[3] (wt% NaCl-CaCl₂)	Density (g/m³)
C-Shaft	Type 1-s-cpy	196.4 ± 51.4	-10.7 ± 6.1	13.9 ± 5.8	13.9 ± 5.0	0.97 ± 0.08
		(101.9:367.4)	(-21.2:-3.8)	(6.0:23.1)	(7.0:22.6)	(0.97:1.12)
		n = 25	n =25	n = 25	n = 25	n = 25

[1] The top number corresponds to the mean (± corresponds to 1σ) , bracketed numbers give the range, n = the number of measurements, Th = temperature of homogenization, Tm = temperature of final ice melting.

[2] C-Shaft Fault salinity data for eutectic temperatures above -21.1°C in the NaCl-H₂O system calculated using Brown and Lamb, 1989.

[3] C-Shaft Fault salinity (eq. NaCl-CaCl₂) determined using the NaCl-CaCl₂-H₂O system of Oakes et al. (1990). (X_{NaCl} = 0.27) where X_{NaCl} is the molar volume.

Table 3.6: Fluid Inclusion Data Summary for FIA data[1]

Group	Inclusion Type	T_h (°C)	T_m (°C)	Salinity (wt% NaCl equiv.)	Salinity (wt% NaCl-CaCl$_2$)	Density (g/m^3)
McD I Fault	Type 1-p	173.5 ± 24.9 (125.4:244.6) n = 21	-3.5 ± 2.5 (-7.6:-0.3) n = 21	5.4 ± 3.8 (0.5:11.2) n = 21	6.0 ± 3.9 (0.7:11.7) n = 21	0.93 ± 0.04 (0.86:1.00) n = 21
	Type 1-p [2] Ca^{2+} system	106.6 ± 21.5 (88.3:130.3) n = 4	-31.3 ± 4.6 (-36.2:-26.5) n = 4	26.0 ± 1.2 (24.7:27.2) n = 4	25.8 ± 1.51 (24.2:27.3) n = 4	1.19 ± 0.03 (1.16:1.2) n = 4
	Type 1-ps	165.4 ± 18.6 (138.6:192.9) n = 12	-7.6 ± 2.8 (-12.9:-5.2) n = 12	10.9 ± 3.1 (8.1:16.9) n = 12	11.4 ± 2.8 (8.9:16.5) n = 12	0.98 ± 0.04 (0.94:1.02) n = 12
	Type 1-ps [2] Ca^{2+} system	161.6 ± 98.4 (66.8:259.5) n = 4	-28.9 ± 3.4 (-33.0:-25.6) n = 4	25.4 ± 1.0 (24.3:26.5) n = 4	25.1 ± 1.3 (23.8:26.6) n = 4	1.14 ± 0.08 (1.07:1.22) n = 4
	Type 1-s-cpy	163.7 ± 16.1 (138.1:188.8) n = 14	-7.2 ± 2.1 (-11.1:-5.0) n = 14	10.6 ± 2.5 (7.8:15.1) n = 14	11.1 ± 2.2 (8.5:15.0) n = 14	0.98 (0.95:1.04) n = 14
	Type 1-s-chl	NA	NA	NA	NA	NA
	Type 1-s-py	114.4 ± 24.5 (80.8:144.2) n = 7	-24.1 ± 11.7 (-40.3:-11.6) n = 7	22.2 ± 5.0 (15.5:28.1) n = 7	21.8 ± 5.0 (15.4:27.6) n = 7	1.1 ± 0.06 (1.1:1.2) n = 7

[1] The top number corresponds to the mean (± corresponds to 1σ for the Type - for each individual FIA, 1σ can be found in Appendix 4 under each sample file), bracketed numbers give the range, n = the number of measurements, Th = temperature of homogenization, Tm = temperature of final ice melting.

[2] Tm measurements were below -21.1 °C suggestive of other cations. Measurements were calculated using the H_2O-$CaCl_2$ ± CO_2 system of (Bodnar et al., 1989). Possible Ca^{2+} bearing inclusions were plotted with NaCl-H_2O inclusions given that the difference between the two systems is insignificant.

[3] McD I Fault salinity data for eutectic temperatures above -21.1°C in the NaCl-H_2O system calculated using Brown and Lamb, 1989.

[4] McD I Fault salinity (eq. NaCl-$CaCl_2$) determined using the NaCl-$CaCl_2$-H_2O system of Oakes et al. (1990). (X_{NaCl} = 0.27, Pyrite vein X_{NaCl} = 0.08) where X_{NaCl} is the molar volume.

Table 3.7: Fluid Inclusion Data Summary for FIA data[1]

Group	Inclusion Type	T_h (°C)	T_m (°C)	Salinity [3] (wt% NaCl equiv.)	Salinity [4] (wt% NaCl-CaCl$_2$)	Density (g/m^3)
McD II Fault	Type 1-p	193.2 ± 12.5 (171.2:226.6) n = 35	-7.1 ± 3.3 (-18.0:-3.1) n = 35	10.2 ± 3.6 (5.0:20.9) n = 35	10.9 ± 3.1 (6.0:19.7) n = 35	0.95 ± 0.04 (0.91:1.08) n = 35
	Type 1-p Ca^{2+} system	NA	NA	NA	NA	NA
	Type 1-ps	181.5 ± 13.8 (150.6:210.9) n = 23	-6.8 ± 1.6 (-10.3:-3.5) n = 23	10.2 ± 2.1 (5.6:14.3) n = 23	10.9 ± 1.8 (6.6:14.4) n = 23	0.96 ± 0.02 (0.93:1.00) n = 23
	Type 1-ps Ca^{2+} system	NA	NA	NA	NA	NA
	Type 1-s-cpy	180.8 ± 19.8 (140.0:232.7) n = 40	-7.1 ± 2.8 (-13.6:-2.8) n = 40	10.3 ± 3.5 (4.6:17.4) n = 40	10.9 ± 3.1 (5.5:16.9) n = 40	0.96 ± 0.04 (0.88:1.04) n = 40
	Type 1-s-cpy Ca^{2+} system	154.7 ± 8.9 (145.0:167.4) n = 4	-29.8 ± 0.7 (-30.5:-29.1) n =2	NA	25.1 ± 0.7 (24.1:25.9) n = 4	1.15 ± 0.00 (1.15:1.19) n = 2
	Type 1-s-chl	189.7 ± 13.2 (177.2:210.8) n = 4	-4.8 ± 0.28 (-5.0:-4.3) n = 4	7.5 ± 0.40 (6.8:7.7) n = 4	8.5 ± 0.38 (7.8:8.8) n = 4	0.93 ± 0.01 (0.92:0.95) n = 4

[1] The top number corresponds to the mean (± corresponds to 1σ for the Type - for each individual FIA, 1σ can be found in Appendix 4 under each sample file), bracketed numbers give the range, n = the number of measurements, Th = temperature of homogenization, Tm = temperature of final ice melting.

[2] Tm measurements were below -21.1 °C suggestive of other cations. Measurements were calculated using the H_2O-CaCl$_2$ ± CO_2 system of (Bodnar et al., 1989). Possible Ca^{2+} bearing inclusions were plotted with NaCl-H_2O inclusions given that the difference between the two systems is insignificant.

[3] McD II Fault salinity data for eutectic temperatures above -21.1°C in the NaCl-H_2O system calculated using Brown and Lamb, 1989.

[4] McD II Fault salinity (eq. NaCl-CaCl$_2$) determined using the NaCl-CaCl$_2$-H_2O system of Oakes et al. (1990). (X_{NaCl} = 0.13) where X_{NaCl} is the molar volume.

Table 3.8: Fluid Inclusion Data Summary for FIA data[1]

Group	Inclusion Type	T_h (°C)	T_m (°C)	Salinity [3] (wt% NaCl equiv.)	Salinity [4] (wt% NaCl-CaCl$_2$)	Density
Corbet Deposit	Type 1-p	177.8 ± 16.5	-9.87 ± 6.7	12.8 ± 7.4	12.8 ± 7.4	0.98 ± 0.06
		(154.1:190.2)	(-15.8:-3.4)	(5.5:19.3)	(5.5:19.3)	(0.92:1.04)
		n = 4	n = 4	n = 4	n = 4	n = 4
	Type 1-p Ca^{2+} system	NA	NA	NA	NA	NA
	Type 1-ps	227.6 ± 40.1	-4.4 ± 2.0	6.8 ± 2.8	7.5 ± 2.9	0.89 ± 0.06
		(151.5:289.2)	(-8.8:-2.2)	(3.6:12.6)	(3.6:13.0)	(0.77:0.98)
		n = 18	n = 18	n = 18	n = 18	n = 18
	Type 1-ps Ca^{2+} system	190.5 ± 25.7	-28.6 ± 5.5	NA	24.4 ± 2.1	0.89 ± 0.01
		(170.9:228.2)	(-35.0:-24.0)		(22.5:26.8)	(0.87:0.90)
		n = 4	n = 4		n = 4	n = 2
	Type 1-s-cpy	216.5 ± 52.5	-7.4 ± 5.1	10.1 ± 6.2	10.4 ± 5.9	0.91 ± 0.1
		(150.0:297.7)	(-16.6:-2.5)	(4.1:17.9)	(5.0:19.9)	(0.77:1.0)
		n = 16	n = 16	n = 16	n = 14	n = 14
	Type 1-s-cpy Ca^{2+} system	177.0 ± 9.3	-29.3 ± 2.5	NA	24.8 ± 1.0	0.89 ± 0.02
		(167.3:188.7)	(-31.0:-26.0)		(23.6:25.6)	(0.88:0.91)
		n = 4	n = 4		n = 4	n = 4

[1] The top number corresponds to the mean (± corresponds to 1σ for the Type - for each individual FIA, 1σ can be found in Appendix 4 under each sample file), bracketed numbers give the range, n = the number of measurements, Th = temperature of homogenization, Tm = temperature of final ice melting.

[2] Tm measurements were below -21.1 °C suggestive of other cations. Measurements were calculated using the H_2O-$CaCl_2$ ± CO_2 system of (Bodnar et al., 1989). Possible Ca^{2+} bearing inclusions were plotted with NaCl-H_2O inclusions given that the difference between the two systems is insignificant.

[3] Corbet Deposit salinity data for eutectic temperatures above -21.1°C in the NaCl-H_2O system calculated using Brown and Lamb, 1989.

[4] Corbet Deposit salinity (eq. NaCl-$CaCl_2$) determined using the NaCl-$CaCl_2$-H_2O system of Oakes et al. (1990). (X_{NaCl} = 0.09) where X_{NaCl} is the molar volume.

Table 3.9: Fluid Inclusion Data Summary for FIA data[1]

Group	Inclusion Type	T_h (°C)	T_m (°C)	Salinity[2] (wt% NaCl equiv.)	Salinity[3] (wt% NaCl-CaCl2)	Density (g/m³)
C-shaft fault	Type 1-s-cpy	201.0 ± 27.2 (157.2:250.5) n = 14	-11.3 ± 6.1 (-21.2:-4.0) n =14	14.5 ± 5.7 (7.3:23.2) n = 14	14.4 ± 5.0 (7.2:22.6) n = 14	1.0 ±0.04 (0.93:1.06) n = 14

[1] The top number corresponds to the mean (± corresponds to 1σ for the Type - for each individual FIA, 1σ can be found in Appendix 4 under each sample file), bracketed numbers give the range, n = the number of measurements, Th = temperature of homogenization, Tm = temperature of final ice melting.

[2] C-shaft Fault salinity data for eutectic temperatures above -21.1°C in the NaCl-H_2O system calculated using Brown and Lamb, 1989.

[3] C-shaft Fault salinity (eq. NaCl-$CaCl_2$) determined using the NaCl-$CaCl_2$-H_2O system of Oakes et al. (1990). (X_{NaCl} = 0.27) where X_{NaCl} is the molar volume.

Table 3.10: Fluid Inclusion Data for CO_2 bearing inclusions.

Group	Inclusion Type	Sample Number	Zone in section	Flinc #	Tm_{CO2}[1] (°C)	$Tm_{clathrate}$[2] (°C)	wt% NaCl equiv.	T_{h-CO2}[3] (°C)	T_{htot}[4] (°C)
McD I Fault	Type 2-s-$L_{(CO2)}$-V	SZMDI 03 02	17	14	-57.2	9.6	0.8	21.1	NA
McD II Fault	Type 2-s-$L_{(CO2)}$-V	SZMDII 03 06	40	1	-60.3	8.9	2.2	18.3	Td[5]> 600
		SZMDII 03 06	40	2	-59.5	9.1	1.8	18.5	Td = 294.3
		SZMDII 03 06	52	3	-60.2	6.3	6.9	9.9	Td = 477.4
		SZMDII 03 06	52	4	-60.5	6.7	6.2	9	Td = 431.2
		SZMDII 03 19a1	33	1	-60.3	7.2	5.3	9.8	Td > 600
		SZMDII 03 19a1	33	2	-59.9	7.7	4.4	9.6	Td > 600 Th ~ 331 & Td =
		SZMDII 03 20	66	7	-59.1	6.9	5.8	7.7	341.7
		SZMDII 03 20	115	26	-59.2	9.1	21.3	14.2	Td = 324.7
		SZMDII 03 16 2	62	32	-58.3	8.6	2.8	9.5	Td = 372.4
		SZMDII 03 16 2	7	57	-58.2	4.6	19.4	10.3	Td = 334.5
		SZMDII 03 16 2	7	65	-63.5	9.3	1.4	11.7	Td > 600
		SZMDII 03 19b3	59	16	-60.9	9.6	0.8	10.9	NA
		SZMDII 03 19b3	51	39	-59.9	6.7	6.2	17.8	NA

[1] Tm_{CO2} – Melting temperature of CO_2.
[2] $Tm_{clathrate}$ – melting temperature of the clathrate.
[3] T_{hCO2} – homogenization temperature of CO_2.
[4] T_{htot} – total homogenization of the liquid.
[5] T_d - decrepitation temperature of the fluid inclusion.

Ranges of FIAs of the McDougall I/II, C-shaft faults and the Corbet Deposit
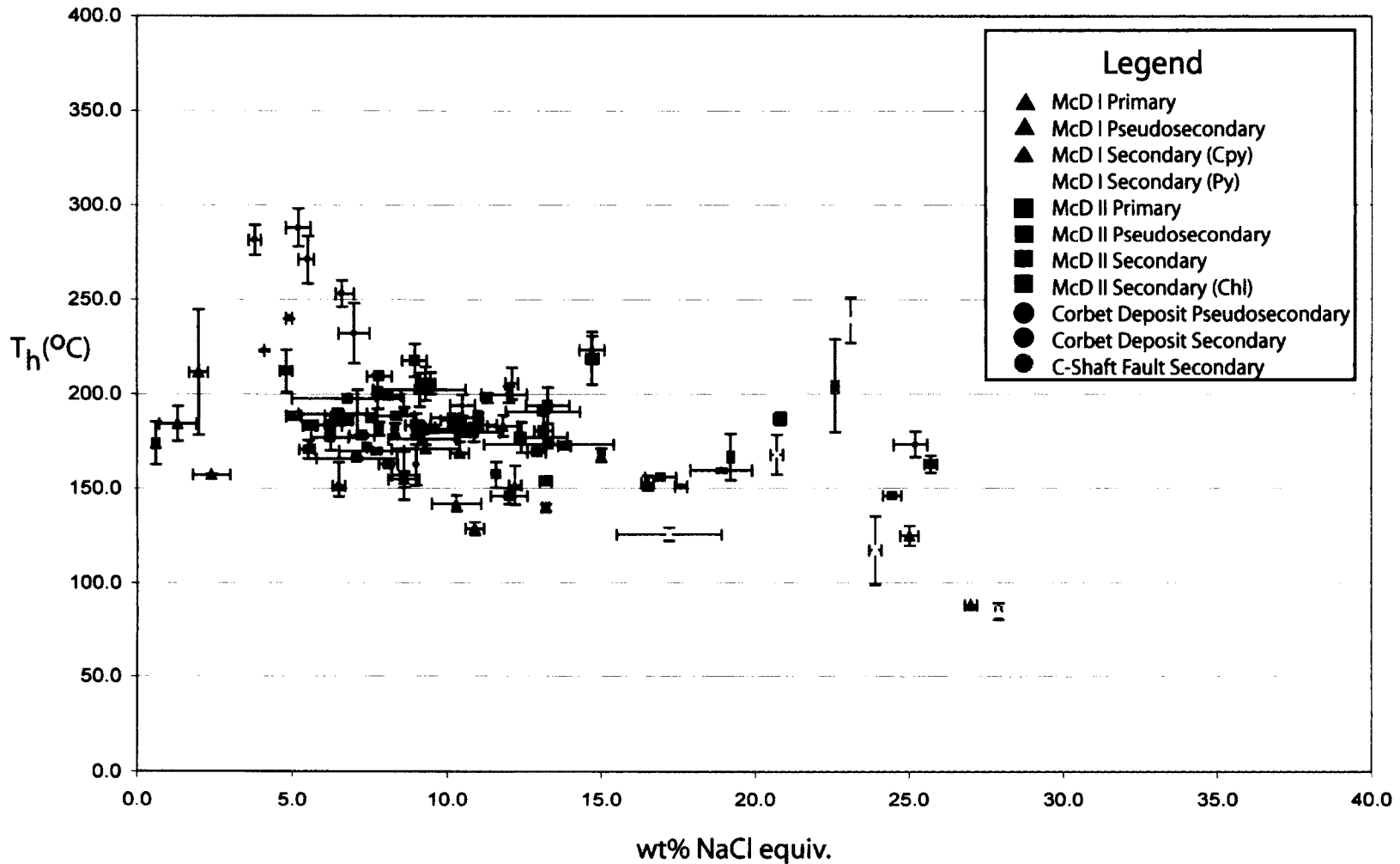
Figure 3.7: Ranges of FIAs for the McDougall I, II, C-Shaft Faults and the Corbet Deposit. Uncertainty bars represent the entire range of data for each individual FIA.

FIAs for the McDougall I Fault
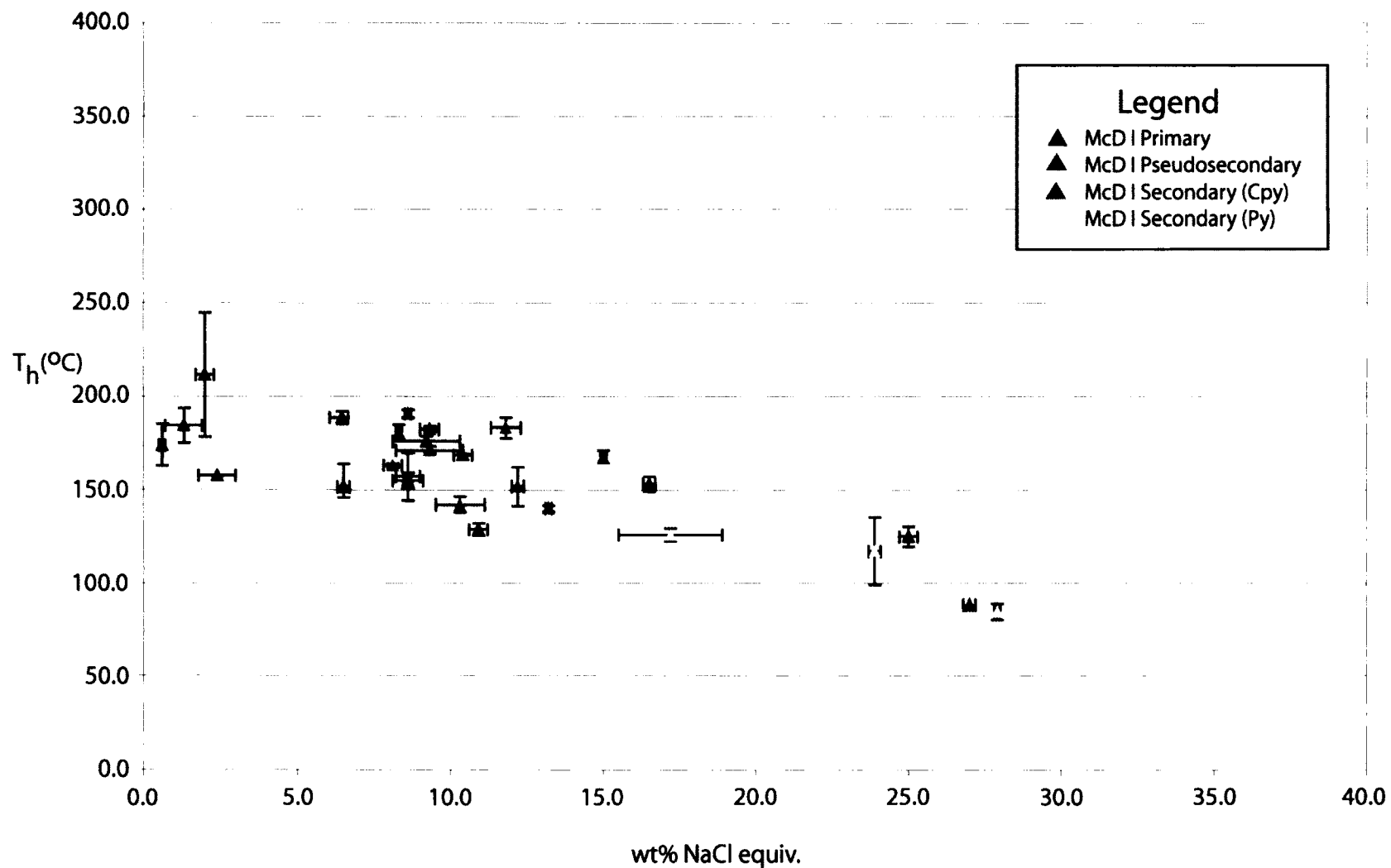
Figure 3.8: Ranges of FIAs for the McDougall I Fault. Uncertainty bars represent the entire range of data of each individual FIA.

FIAs for the McDougall II Fault
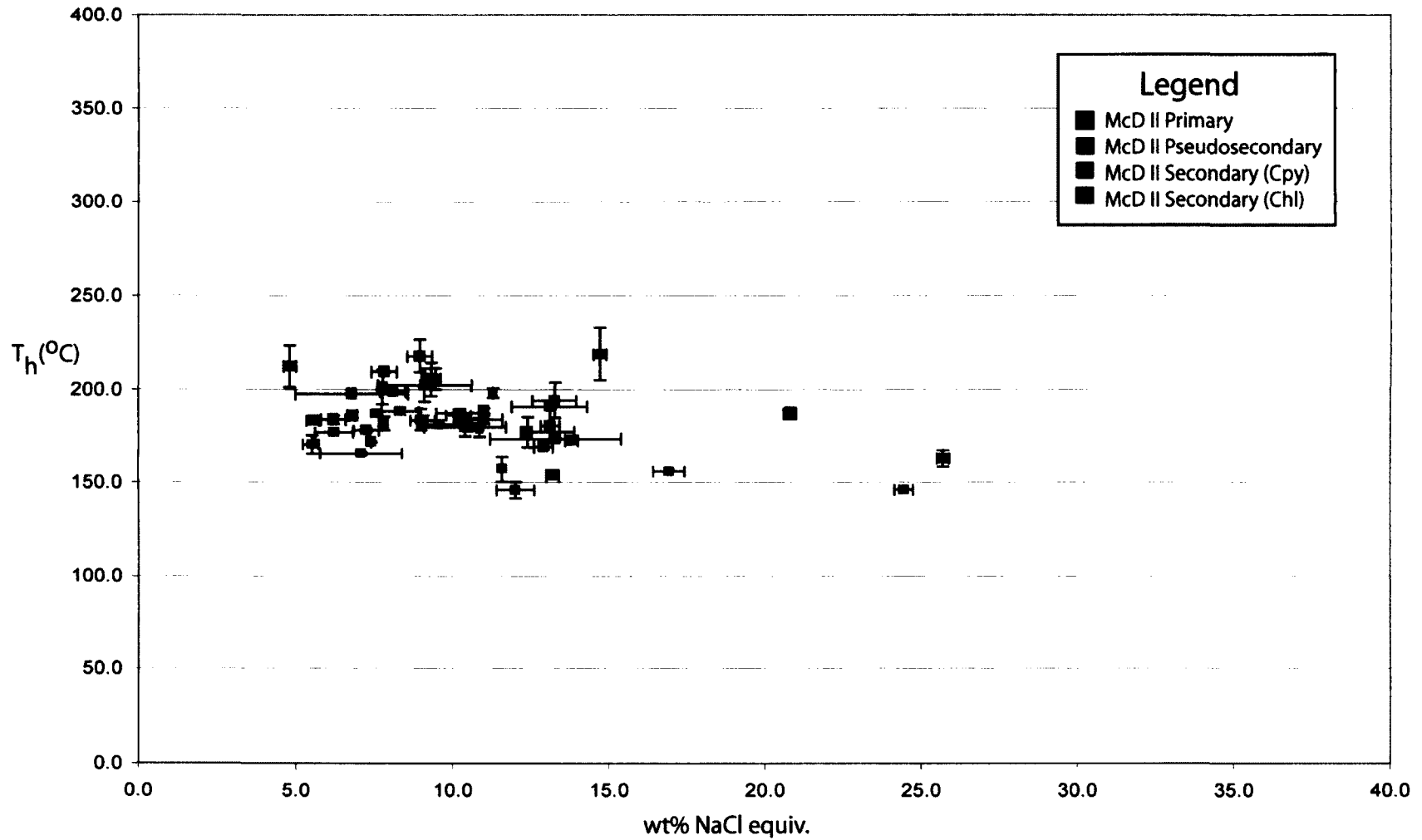
Figure 3.9: Ranges of FIAs for the McDougall II Fault. Uncertainty bars represent the entire range of data for each individual FIA.

FIAs for the Corbet Deposit and the C-Shaft Fault
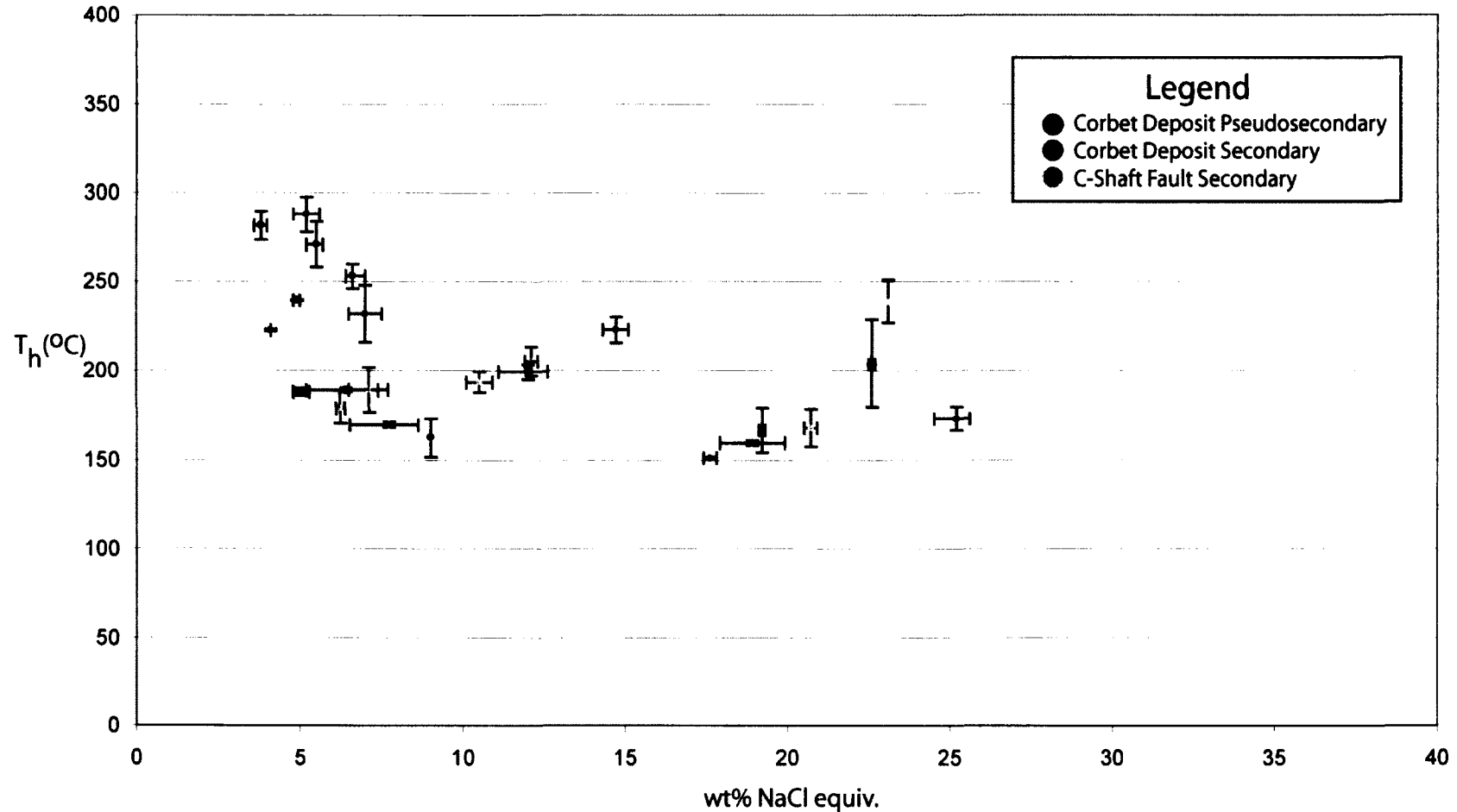
Figure 3.10: Ranges of FIAs for the Corbet Deposit and C-Shaft Fault. Uncertainty bars represent the entire range of data for each individual FIA.

All FIAs and non-FIA Data from the McDougall I, II, Corbet Deposit and C-Shaft Fault
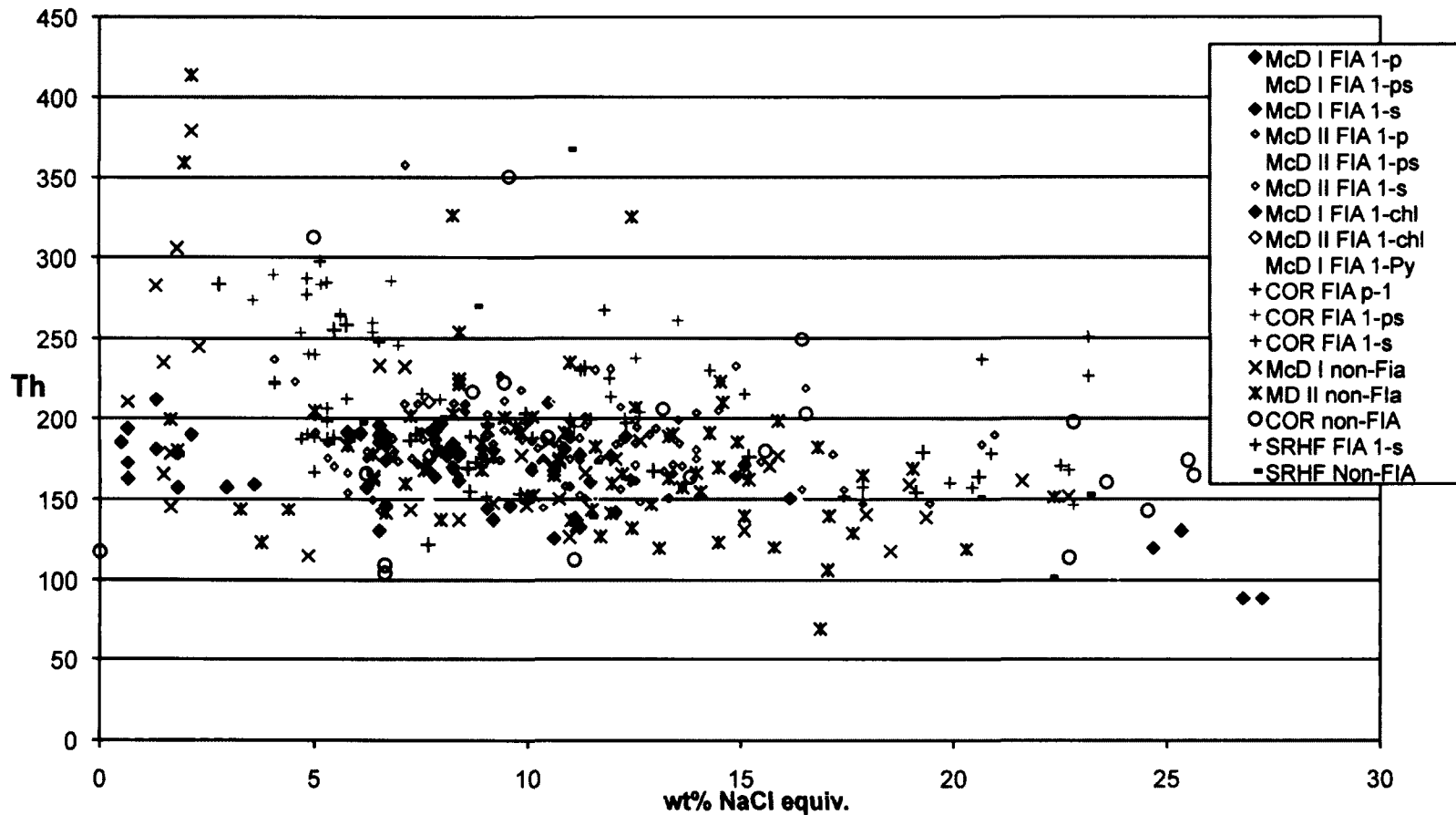
Figure 3.11 Salinity vs. Th plot for the Noranda fluids. Data represents "Type" compositions for the McD I, II, Corbet Deposit and C-Shaft Fault. The data highlighted in black represents microthermometric measurements that were not included in the FIAs.

"Hot-Cathode" Cathodoluminescence (CL)

Analytical Procedure

"Hot-cathode" CL was combined with transmitted light microscopy to establish

the nature of various textures within quartz in the McD and C faults and to evaluate these

textures with respect to associated sulfide minerals, to test for the presence of primary

growth textures, and to evaluate the extent of post-entrapment modification of

hydrothermal quartz. This approach follows Ioannou et al. (2004). A total of 8

representative, carbon-coated thin sections were studied, with 3 samples each from the

McD I and II faults and 2 samples from the C fault.

The analysis was carried out by Dr. Götze at the Institute of Mineralogy, Frieberg

University of Mining and Technology, Germany on a "hot-cathode" CL microscope

HC1-LM (Neuser et al., 1995; Götze and Kempe, 2008) at 14 kV and a current density of

$\sim$10 μA/mm^2. Luminescence images were captured "on-line" during CL operation using

a peltier cooled digital camera (KAPPA 961-1138 CF 20 DXC). Thin section scans

previously used for fluid inclusion mapping were highlighted, specifying areas where

microthermometry measurements were taken and where quartz-sulfide textures appeared

favorable to evaluate quartz characteristics. To record time-dependent changes of CL

properties, images were taken initially and then after 40s with relatively long exposure

times due to the low intensity of the CL response and using additional electronic

amplification. Electron bombardment of specific areas could only be done once, to avoid

falsification of primary CL colours at non-irradiated sampling locations. Due to

electronic amplification above normal CL procedures, some micrographs show slight

"striations" and the quality of polishing sometimes produced an imperfect

photomicrograph. All Hot-CL photomicrographs (marked KL) are provided in Appendix 2, accompanied by photomicrographs taken using transmitted (TL) and polarized light (PL) for comparison of sample characteristics.

The CL spectrum wavelengths in the 380 to 1000 nm range were recorded using an Acton Research SP-2356 digital triple-grating spectrograph with a Princeton Spec-10 CCD detector that was attached to the CL microscope by a silica-glass fibre guide. CL spectra were measured under standardized conditions (wavelength calibration by a Hg-halogen lamp, spot width 30μm, measuring time 5 s). Measuring time-resolved spectra analysis occurred initially, and after 1 and 2 minutes (Götze, pers. Comm.) and spectra are provided in Appendix 2.

Results

Quartz veins within all of the faults had a similar initial CL response showing blue turning to a brownish violet colour in less than 120s (Appendix 2 – spectra graphs) during electron bombardment, which is interpreted to be a characteristic feature of hydrothermal quartz (Marshall, 1988; Ramseyer et al., 1988; Ramseyer and Mullis, 1990; Perny et al., 1992; Götze et al., 2001, Götze, 2009), a characteristic in both natural and synthetic hydrothermal quartz specimens (Götze, 2009). This indicates that the hydrothermal signature of Archean-age quartz is preserved (e.g. Ioannou et al., 2004). The CL response of hydrothermal quartz, from a transient blue CL to brownish violet is attributed to the alkali (or hydrogen) compensated center [AlO_4/M^+] of a deep blue emission band emitting a ~390 nm max emission band (blue), and emitting an orange-red (brownish-violet) band at about 620-650 nm (Götze, 2001) during electron bombardment over 40s (with the Noranda samples), caused by recombining electrons in the non-

bridging oxygen band-gap state with holes in the valence-band edge (Siegel and Marrone, 1981; Götze, 2001). Therefore, the structure of minerals affects their luminescence characteristics, which is important in quartz, where activator elements are limited due to its structure. Lattice defects are affected by thermodynamic conditions during mineral growth, temperature, metamorphism, deformation and post mineralization effects can change the structural properties, thus affecting their luminescence (Götze, 2001).

A feature that is common to quartz in all 3 faults is the presence of fine carbonate grains (calcite – spectrum sample SZMDI-03-23 in Appendix 2), which are visible as a bright orange CL colour. Also, the greenish-grey CL response in cavities and fractures is due to the luminescence of resin that caused a strong background and small peaks in the CL spectra.

McDougall I

Sample SZMDI-03-06-2 (Fig 3.12 A & B) shows a clear hydrothermal signature with zonation of interlocking comb textured quartz, thus showing preserved growth textures and indicating that the Type 1-p inclusions are in quartz of hydrothermal origin. Within a second location of the same quartz sample, photo Fig 3.12 D shows a clear hydrothermal signature but with marginal fracturing and secondary healing (2nd fluid generation) or crystallization from a non-crystalline silica precursor (due to the irregular internal structure).

In sample SZMDI-03-23 (Fig 3.12 E and F) the zonation within large comb textured quartz crystals is faint, and is cross-cut by quartz in fractures. The margin of a quartz crystal in Fig 3.12 F shows minor carbonate and sulfides. Sample SZMDI-03-09 (Fig 3.12 H) shows microcrystalline, mosaic and comb textured quartz in cross-polars

(Fig 3.12 G), all with a similar hydrothermal signature but with slight varying colour intensities of similar luminescence, but no evidence of growth zoning. Small spots of sulfides occur within microcrystalline quartz along grain boundaries. In Fig 3.12 H minor zones of secondary penetrative fluid trails marginally and along primary growth zones (faint pink-white luminescence) are visible.

McDougall II Fault

All quartz within the McD II fault shows hydrothermal signatures with local "spots" of calcite (orange spots) within quartz, and along the margins of quartz grains. The quartz also shows some characteristics of recrystallization and sulfide corrosion. Fig 3.12 I (sample SZMDII-03-19a2) shows marginal comb textured quartz mantling brecciated wall rock fragments suggesting there has been no movement on the fault post quartz deposition. In addition, Fig 3.12 J also exhibits a second generation of quartz deposition within the center of the vein and triple-junction intersections of quartz with growth zoning. Fig 3.12 L shows the corrosive effect associated with sulfide mineralization, which appears to replace or corrode primary growth textures of comb textured quartz as indicated by the truncation of quartz zoning. Brecciation of zoned quartz and subsequent rehealing may also produce this texture, but sulfide-quartz margins should appear irregular. The effect of sulfide corrosion is also evident along mosaic textured quartz margins in Figs 3.12 M and N. White areas indicate holes within the thin section.

Microcrystalline quartz within the center of quartz veins and along the margins and between comb textured quartz grains, is interpreted to be a product of rapid quartz precipitation, perhaps during boiling that accompanied chalcopyrite mineralization. In

Fig 3.12 P, no internal structure in the hydrothermal quartz is visible (similar to photo

SZMDI 03 09; Fig 3.12 A & B) and this is the same for mosaic textured quartz described

throughout most of the samples. A minor "reaction rim" is displayed in Fig 3.12 Q by an

unstable transient blue CL response where quartz is in contact with sulfides. The reaction

rim CL response possibly indicates partial corrosion and overprinting by quartz locally

along quartz grain margins. Recrystallization of mosaic textured quartz only occurred

within one sample (SZMDII-03-19b3 – Fig 3.12 R) and is indicated by grain coarsening

(in plain polarized light) scattered throughout the quartz grain and an overall

heterogeneous CL response, with recrystallized zones appearing purple-white in colour.

C-shaft Fault

The only appreciably visible difference in quartz veins from the C fault appears

to be a slightly higher abundance of calcite disseminated throughout the quartz. As well,

the texture of the quartz within all of the C fault samples was fractured during the

preparation of the sections resulting in a blocky appearance in PPL and making the

recognition of textures difficult. In addition, the CL intensity was also weak within

sample SZCO3-06-2 (Appendix 2), requiring doubling of the exposure time.

Sample SZC03-27 only exhibits visible relicts of growth zones in comb-textured

quartz (Fig 3.12 T). In addition, secondary fluid trails (pink CL response) appear

marginal to the comb and mosaic textured quartz.
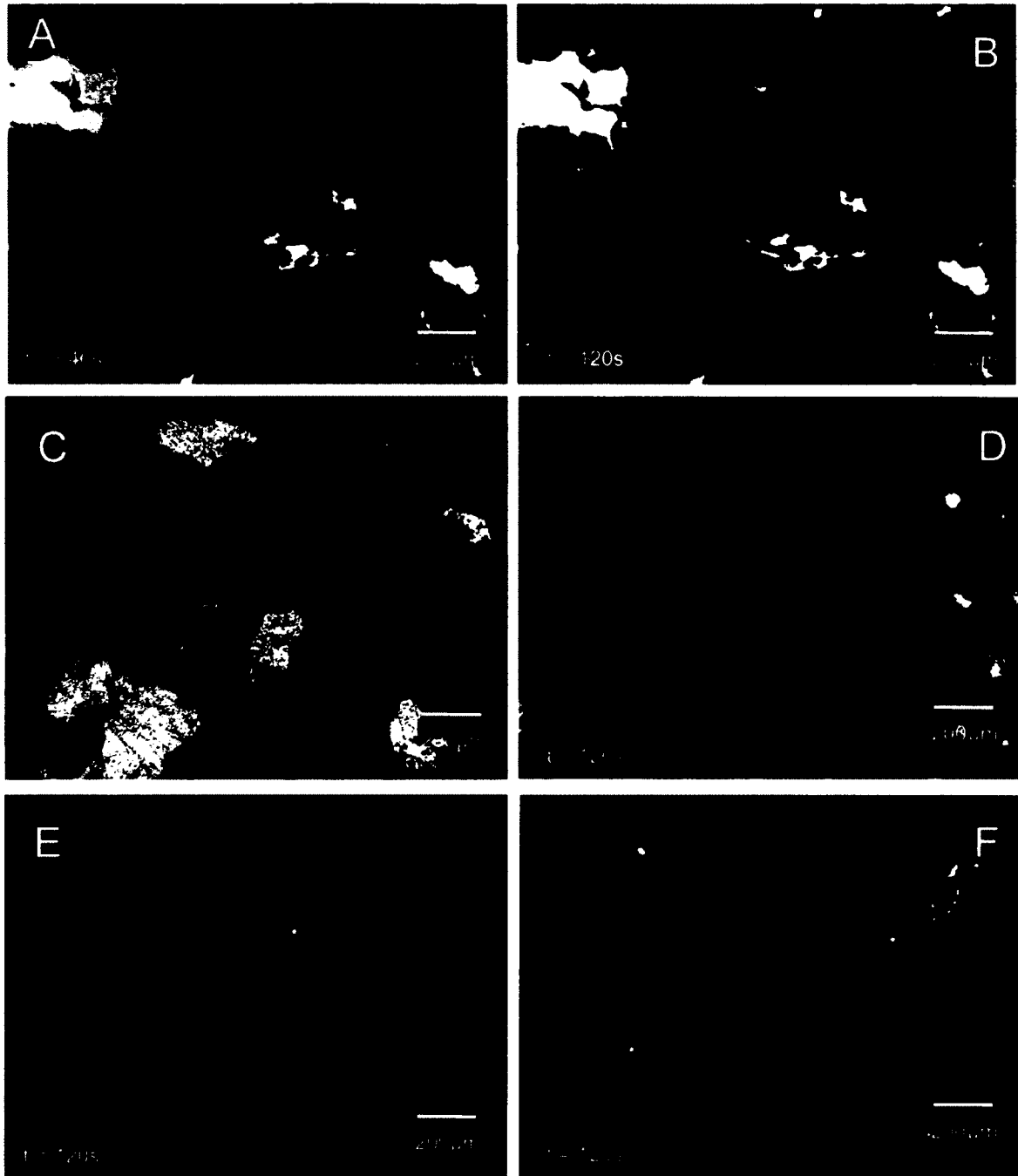
Fig 3.12 A) Sample SZMDI-03-06-2 [image 1a] of an initial intrinsic blue luminescence, (B) Same as above sample, [image 1a] after 40s exposure revealing growth zoned hydrothermal quartz, C) Sample SZMDI-03-06-2 [image 2a] in PPL, D) and showing a brownish-violet luminescence of mosaic and secondary fluid trails with partial corrosion of quartz by chalcopyrite, E) Sample SZMDI-03-23 [Image 1a] of faint internal zoning of large comb-textured quartz with disseminated carbonate (bright orange), F) Sample SZMDI-03-23 [image 2a] of internal growth zones and significantly more carbonate associated with a marginal chalcopyrite vein.
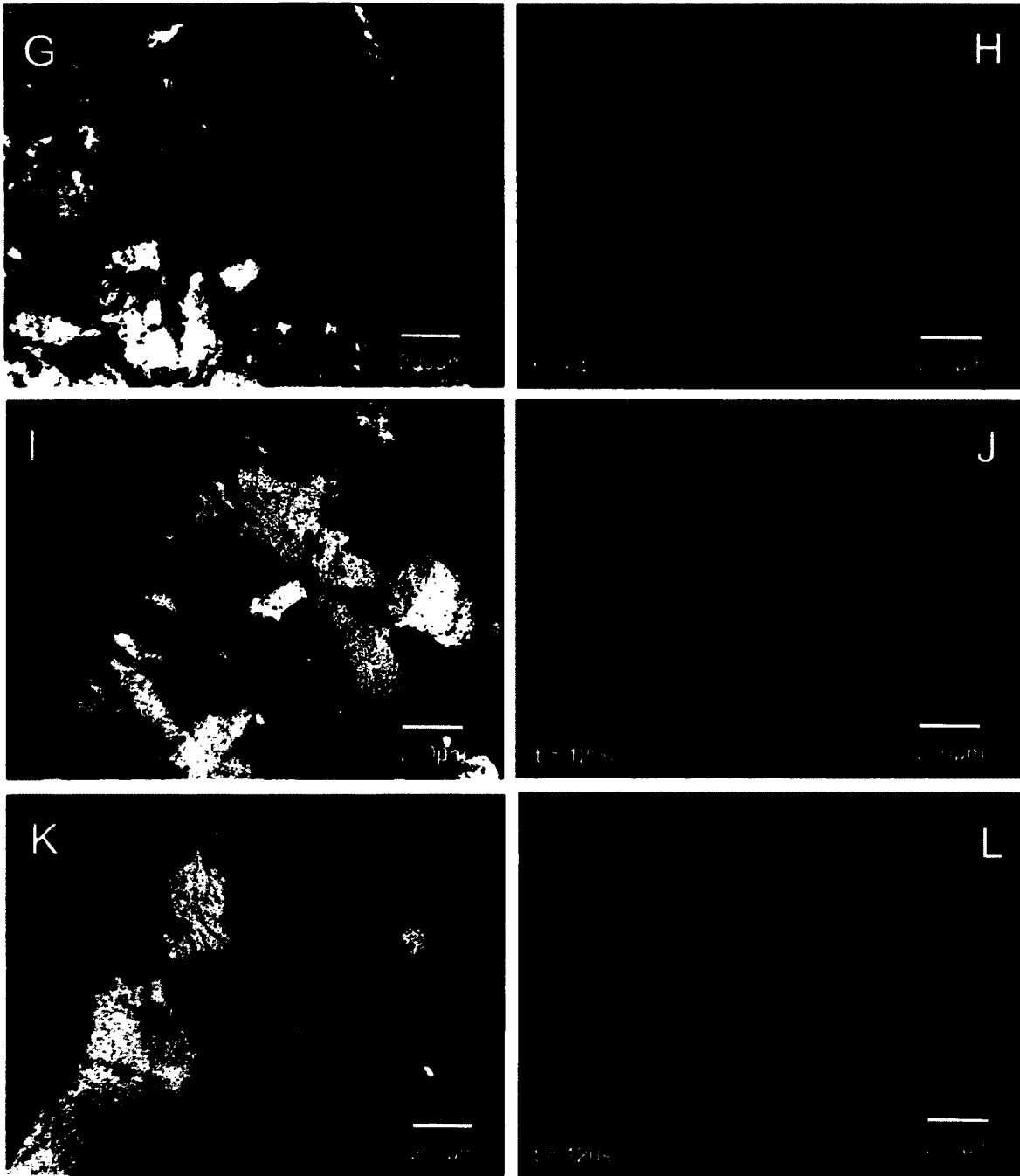
Fig 3.12 con't: Photo G, XPL; photo H, CL) Sample SZMDI-03-09 [image 1a] in XPL of mosaic and microcrystalline quartz (H) exhibiting similar luminescence of hydrothermal signatures but no internal textures, I in XPL; J in CL) Sample SZMDII-03-19a2; Comb textured quartz forms on brecciated fragments with a second fracture infilling quartz vein with triple joints, no deformation or recrystallization is visible. K in XPL; L in CL) Intergrowth of comb-textured quartz with corrosive sulfide truncating growth zones (Sample SZMDII-03-19a2).
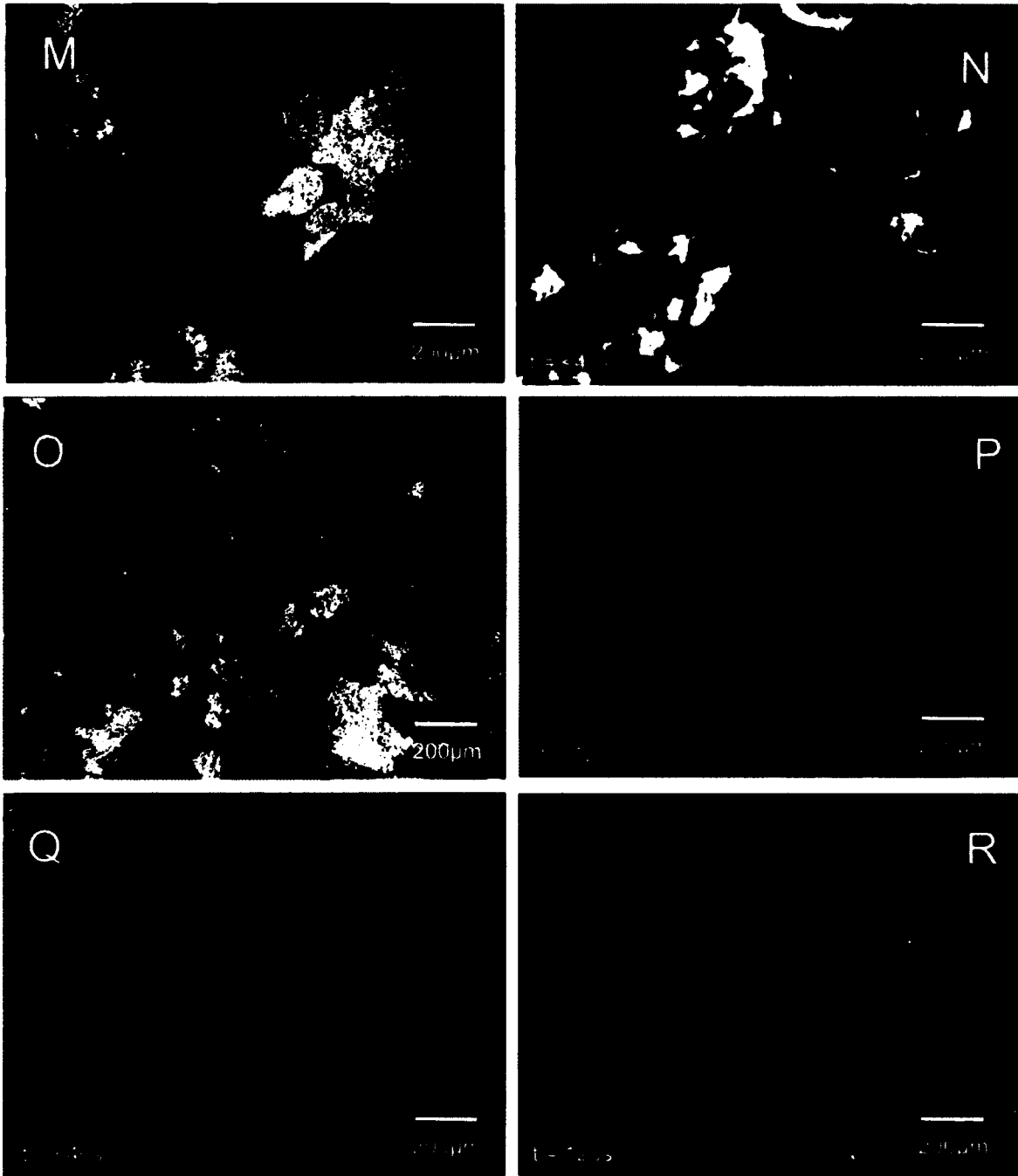
Fig 3.12 con't: Photo M in XPL; N in CL) of sample SZMDII-03-16-4, mosaic textured quartz with corrosive marginal chalcopyrite, O in XPL; P in CL) of sample SZMDII-03-19b3 of microcrystalline quartz with hydrothermal signatures, interpreted to be precipitated during boiling conditions and associated with chalcopyrite mineralization. Q) of the same sample of homogenous hydrothermal signature in mosaic textured quartz with a minor "reaction rim" in contact with chalcopyrite with a unstable blue CL response, R) of the same sample indicating only locally recrystallization of mosaic textured quartz with unstable "spots" of white-violet luminescence within quartz crystals.
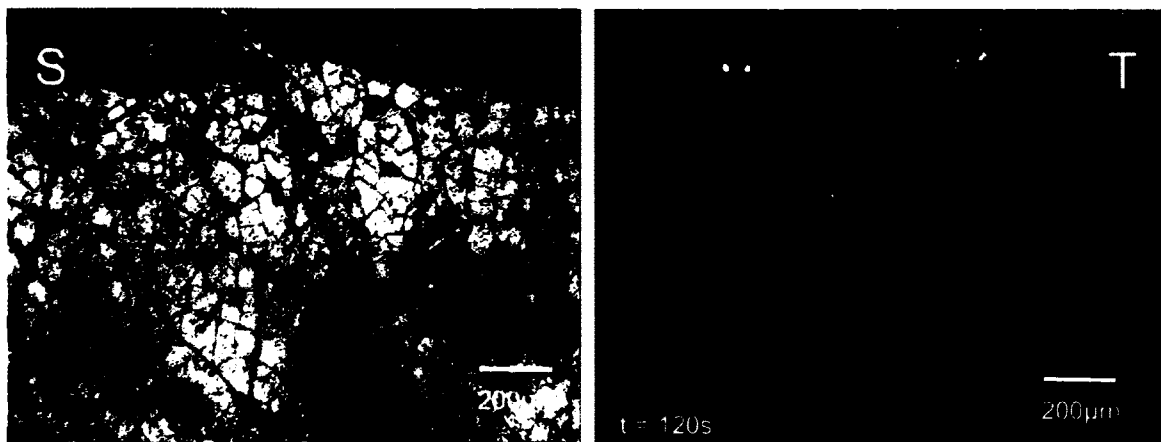
Fig 3.12 con't: Photo S in PPL; T in CL) of sample SZC03-27 [image 1a] showing extensive mechanical fracturing of quartz and in the CL of remnant preserved growth zoning of quartz and marginal infilling by secondary fluids (pink CL).

Interpretation

Comb textured quartz is clearly preserved and primary concentric growth zoning that is not visible in transmitted light has been identified and is of hydrothermal origin. This texture shows that quartz deposition occurred within an open-space environment under slightly varying fluid composition due to the variability in CL response along growth zones. No evidence of recrystallization has been recognized within comb textured quartz, but quartz termination and marginal contacts show partial dissolution and corrosion by chalcopyrite accompanied or followed by the deposition of microcrystalline quartz. Partial dissolution indicates fluid temperatures $>300°C$ (Fourier, 1985), thus consistent with chalcopyrite mineralization. The comb textured hydrothermal quartz has the potential for preserving primary fluid inclusions of hydrothermal origin, and preserving secondary fluids located marginal to corrosive mineralization.

Mosaic textured hydrothermal quartz typically occurs within the center of quartz-sulfide veins and is intergrown with chalcopyrite mineralization. The homogeneous

94

hydrothermal signatures that lack internal structures such as zoning suggest a nonfluctuating hydrothermal fluid composition during quartz crystallization and rapid crystallization (Ioannou et al. 2004). The thin CL rim on mosaic textured quartz in contact with chalcopyrite mineralization is likely due to thermal erosion in contact with a sulfide-rich solution (Ioannou et al. 2004).

Microcrystalline textured quartz veins and fractures are interpreted to represent secondary fluid trails that formed during chalcopyrite deposition as shown by chalcopyrite within the secondary fractures. Microcrystalline quartz is interpreted to have formed during rapid crystal growth from a silica supersaturated solution due to its irregular internal structure. It should be noted that pressure or temperature during quartz crystal growth does not influence the cathodoluminescence of the quartz (Ramseyer and Mullis, 1990).

The Corbet deposit CL response for overprinting of quartz from secondary fluids shows a characteristic unstable bright yellow CL emission shifting at 30s to a reddish-violet CL (Ioannou et al., 2004). The final reddish-violet CL emission occurs throughout the McD and C fault samples but, due to the relatively long exposure times, the initial yellow CL emission was not observed. The reddish-violet luminescence of quartz derived from secondary hydrothermal fluids is distinguishable from the brownish-violet emission of "primary" hydrothermal quartz, in which a very high content of lattice defects is thought to be responsible for this shift to reddish-violet luminescence related to the process of fast crystallization (Götze, 2009). Rapid quartz precipitation may have been triggered by boiling. Secondary fluid inclusion trails within mosaic and comb-textured quartz in contact with microcrystalline quartz and sulfides is interpreted to be a

potential indication of VMS ore PVTX conditions.

Calcite occurs within all of the samples although it was not apparent in transmitted light. The calcite is either disseminated in zoned quartz or occurs as disseminated or anhedral masses with chalcopyrite. Disseminated calcite throughout comb and mosaic textured quartz, suggests "pulses " of a significant CO_3^{2-} component. It should be noted that the major volatile species (higher hydrocarbons, CH_4 or CO_2) and the amount of volatiles does not affect the cathodoluminescence of quartz (Ramseyer and Mullis, 1990). The higher abundance of carbonate (calcite) along quartz margins and in association with chalcopyrite mineralization, suggests carbonate is associated with the ore-bearing fluids. In regards to the effect on isotopic compositions, calcite with ore-mineral association have $\delta^{13}C_{CO2}$ values in the range of 0 to -18‰ (Deer, Howie and Zussman, 1998), and are consistent with McD I and II $\delta^{13}C_{CO2}$ values.

Recrystallized quartz was detected within one sample of the McD II fault and it likely formed during partial compaction due to localized strain. Recrystallization is limited to amorphous mosaic textured quartz, and only forms minor Si-O lattice defects (Sprunt et al. 1978; Ioannou et al. 2004).

The lack of recrystallization within the McD and C faults is significant in that hydrothermal quartz is preserved, compaction and deformation is not widespread and the fault preserves VMS-related fluid inclusions.

Breached Inclusions and Evaporate Mounds

Introduction

Fluid inclusion eutectic temperatures from microthermometric analysis suggest a multi-component system dominated by Na-K-Ca-Mg hydrothermal fluids within Type 1

inclusions. Scanning electron microscopy energy dispersion spectroscopy (SEM-EDS) was used to identify the bulk composition of salts from decrepitated inclusion evaporates on inclusion walls as well as their trapped crystals. Both techniques were carried out on approximately 0.5 x 0.5cm "chips", from the unused portion of the 100μm double polished thin sections prepared for microthermometry. These techniques provide a cost-effective method of determining the semi-quantitative bulk composition of fluid inclusions, significantly lacking from fluid inclusion studies where microthermometry is the only technique used to quantify salinity compositions.

Breached Inclusion Procedure

The inclusions were analyzed using a JSM-6400 scanning microscope with a working distance of 39mm at an accelerated voltage of 20kV, equipped with an EDS spectrometer at Vale-Inco Exploration technical services. The samples were mounted vertically on aluminium stubs with double sided carbon tape and epoxy. The samples were then submerged in liquid nitrogen, removed and then severed at relatively the same height and carbon coated. Although 12 samples were prepared for analysis, only four were analyzed and only one sample (sample SZMDII-03-16-2) provided visible trapped crystals.

Breached Inclusion Results

Some of the trapped inclusions identified in sample SZMDII-02-16-2 are shown in Figure 3.13. Precipitated salts within opened inclusions were not identified, likely due to the relatively low salinities of the fluids and overpressuring, which would have expelled the contents of the inclusions when breached. Similarly, trapped solids may have also been expelled when breached and, in addition, the infrequency of trapped

accidental solids within Type 1 inclusions, that may account for the lack of data. The most common solid inclusions within the cavities are chlorite that is Fe rich (chamosite) (Fig 3.13 D) and Al rich (donbassite), followed by minor carbonates which include malachite and calcium carbonate and less common muscovite, which transects the length of the inclusions. A trapped sulfide in the form of covellite occurs as an irregular mass as well as a Sn - Cu-rich accidental contaminant (likely a bronze-like alloy?) that has tin peaks distinct from the larger Si peak of the host quartz was also observed (Fig 3.13 H).

Breached Inclusions Interpretation

Fluid inclusion microthermometry and evaporate mound analysis confirm that fluids within the MDI/II and C faults are Na^+/K^+ and Ca^{2+}-bearing brines, but condensates of halite or sylvite (chlorides) on individual fluid inclusion cavities were not detectable. Only trapped (accidental) solid inclusions of predominantly mica and chlorite were observed. The significant lack of precipitated salts within inclusions is interpreted to be due to the dominantly low salinity of the inclusions. For example, breached inclusions from the Cobalt Hill Prospect, Mackelcan Township, Ontario, having salinities of 24-46 wt% NaCl and from the Fraser Copper zone, Strathcona embayment with fluids containing 50 wt% NaCl were successfully analyzed for condensed salts by Schandl (2004) and Hanley et al. (2004), respectively. In contrast, fluid inclusions from the McD faults and Corbet deposit typically contain 6-16 wt% equiv. NaCl fluids, well below the high saline brines described above, suggesting that salt condensate formation is impeded by the low salinity of the trapped fluids.

Fluid inclusion petrography identified various trapped minerals with habits suggestive of halite, sylvite, and micas crosscutting the inclusion or embedded on

inclusion walls. A trapped spherical sulfide with halite in Type 2-s-L-V and H_2O-CO_2 ±

complex hydrocarbons (CH) ± multisolid (M) fluid inclusion in Table 3.1 located along a

secondary fracture, in close proximity to sulfide mineralization, suggests that

chalcopyrite mineralization was contemporaneous with quartz precipitation and the

presence of the CuS in image I and spectrum J suggests this sulfide may actually be

covellite. The only other sulfide detected was an elongated tin/copper (bronze alloy?)

sulfide mineral, likely occurring as a contaminant. Trace amounts of Sn were detected in

the geochemical data (Appendix 9) which is suggestive of stannite within both faults, but

were not detectable as trapped solids within inclusions. The most abundant trapped

solids are Fe-rich chlorite and micas, which also occurred with sulfides in the veins and

scattered throughout the quartz matrix to the veins. The sericite and chlorite in inclusions

are consistent with proximal chlorite and sericite alteration that envelopes the veins. The

precipitation of Fe-rich chlorite appears to be contemporaneous with quartz and sulfide

precipitation. Although the breached inclusion technique was unsuccessful in obtaining

chloride condensates to confirm microthermometry observations, the presence of trapped

micas and chlorite confirm fluids were contemporaneous with proximal chlorite and

sericite alteration.

Evaporate Mound Procedure

The technique applied to evaporate mound analysis using an EDS system has

been described in detail by Eadington (1974), with the technique being applied by Walsh

et al. (1988) on Archean Lode gold deposits at Porcupine, and by Khin Zaw et al. (1996)

on the Hellyer VHMS deposit in Tasmania, Australia. More recently, Heinrich and

Cousens (1989), Halter et al. (1996) and Kontak (2004) have applied a microprobe

technique, which may be more sensitive than an EDS. Within this study, fluid inclusions

that represent multiple FIAs were thermally decrepitated within the Linkam THMSG600

heating-freezing stage at Laurentian University within a temperature range of 500-600°C
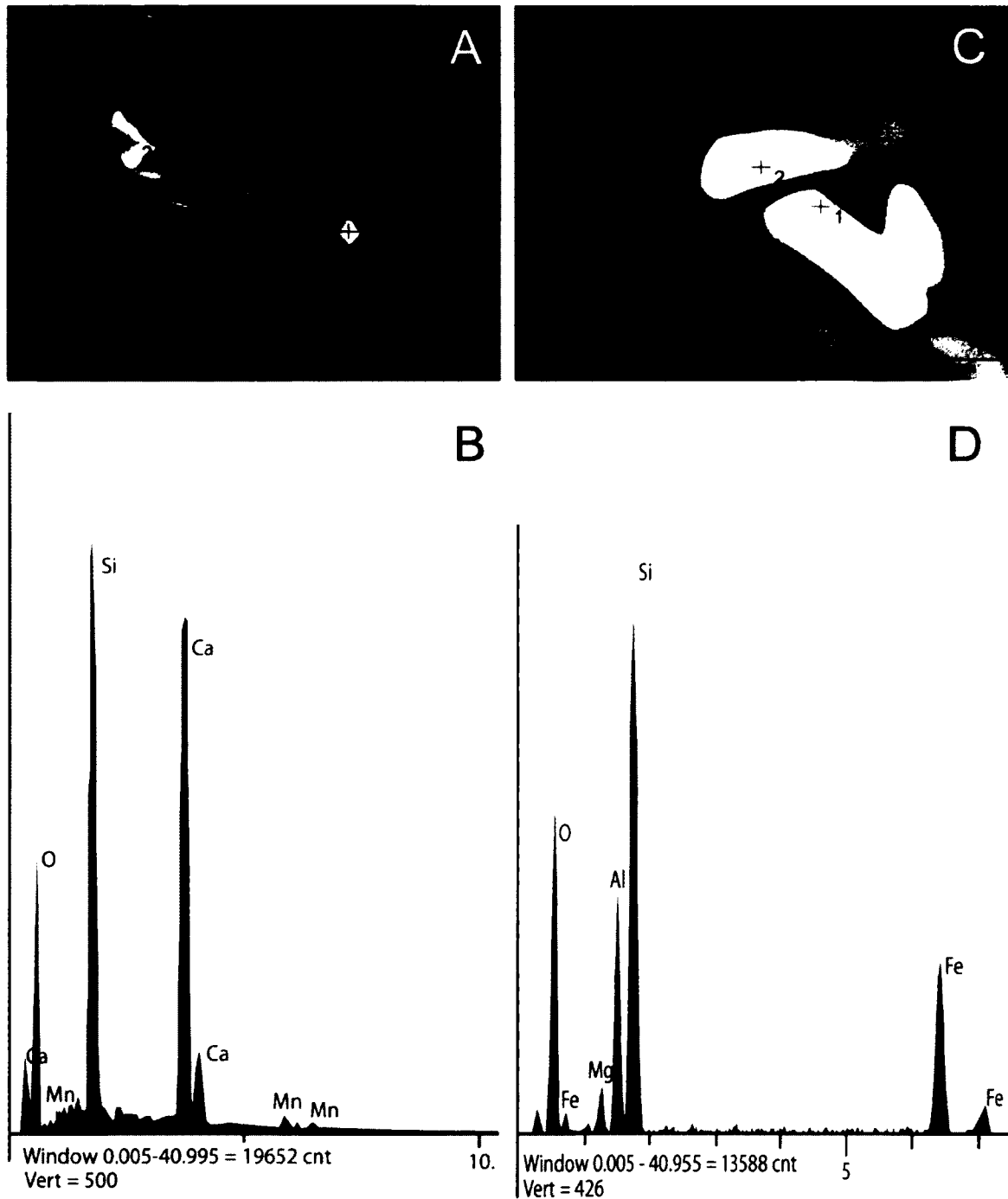
Fig 3.13 A) SEM photograph of precipitated or trapped salt on the edge of breached
inclusions B) SEM spectrum of spot #2 from image (A) of Ca bearing precipitate C) SEM
photograph trapped mineral and an accidental inclusion in the open fluid inclusion cavity.
D) SEM spectrum of spot #2 on image (C) of Fe-chlorite.
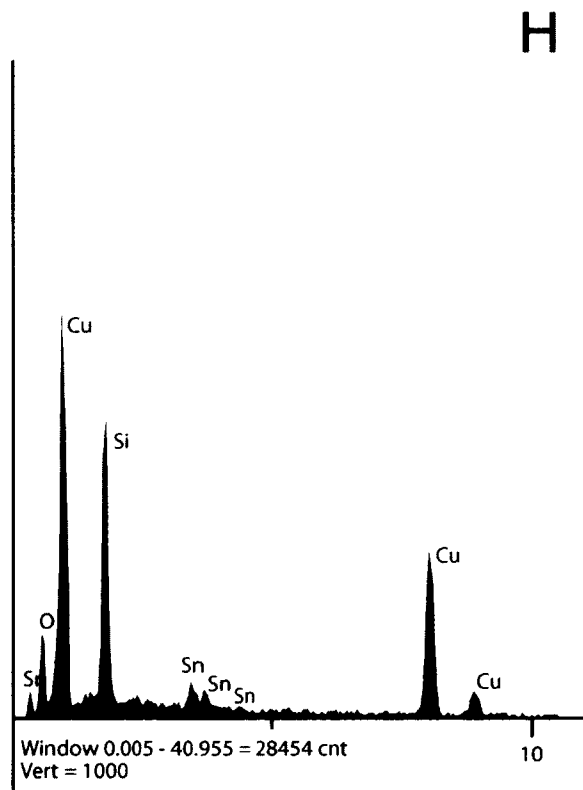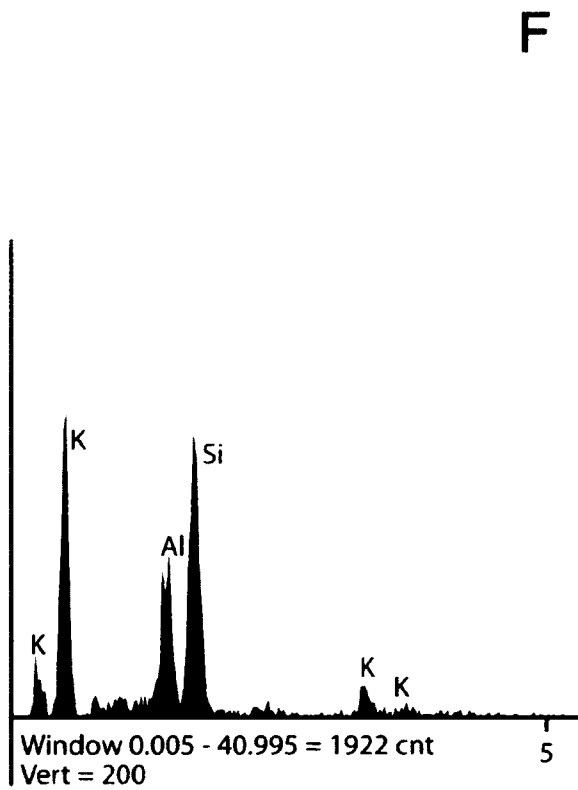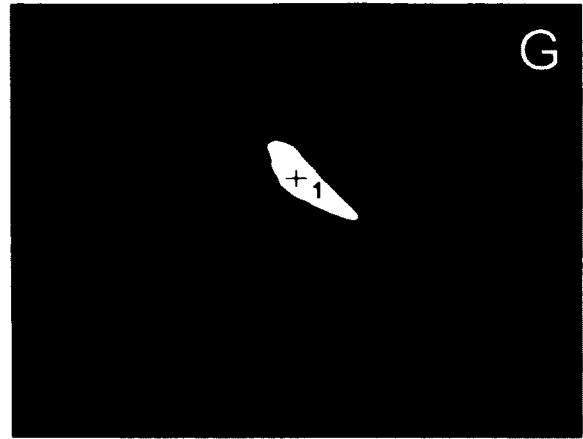
Fig 3.13 con't E) Sheet of muscovite transecting the inclusion F) SEM spectrum of trapped muscovite G) Anhedral mass of an accidental inclusion in an inclusion cavity H) SEM spectrum of accidental inclusion (bronze?) in image (G) with trace amounts of tin.
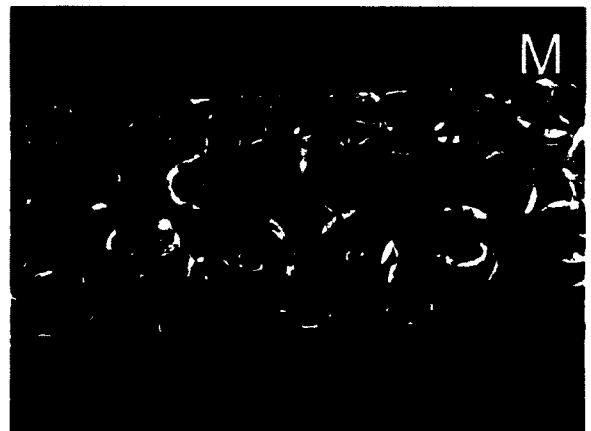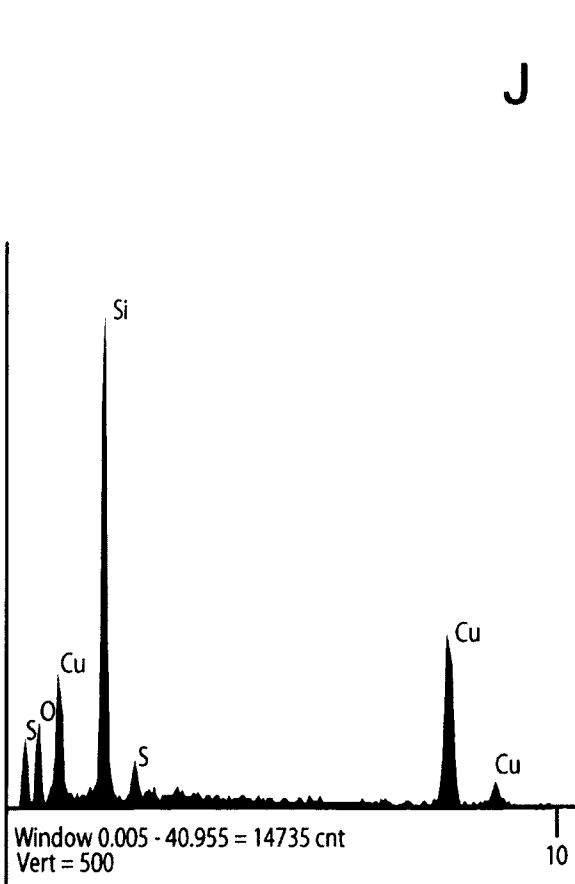
Fig 3.13 con't. I) Cu rich sulfide trapped on the edge of an inclusion cavity. J) SEM spectrum analysis of trapped sulfide. K) Breached open cavity inclusion with what appears to be a book of muscovite and trapped cubic inclusion. Due to the depth of the trapped inclusions in the inclusion cavity, no spectrums could be adequately identified. L) SEM photo of a double polished 100μm thin section mounted vertically revealing the texture of the fractured surface exposing breaching inclusion. M) 12 mounted chip

and quickly cooled by turning off the heating stage. Chips were then transferred to double-sided carbon tape, attached to a glass slide and visually scanned for the presence of evaporates mounds (Fig 3.14 A & B). The samples were then carbon coated and analysed utilizing a JSM-6400 scanning microscope with a working distance of 15mm and an accelerating voltage of 20kV, calibrated against table salt. The analysis of the evaporate mounds was either produced by rastering to cover a significant section of the mound to average out chemical homogeneity or typically by multiple point counts on the mounds to identify the potential for various mixtures. The evaporate mound analysis results in a mixture (bulk analysis) of the chloride salts from various types of fluid inclusions producing an average chemical composition and semi-quantitative data.

Composition of Evaporate Mounds

Multiple chips were prepared from type (I), (II) and type (V) veins of the McD I and II faults. The analyses indicates that the evaporate mounds are mixtures dominated by Na^+ and K^+ cations, with minor Ca^{2+} and Mg^{2+} cations. The dominant anion is Cl^-, with only minor S detected in the type (V) vein of the McD I fault. Results are subdivided, based on their occurrence within variable vein types, and plotted in Na-K-Ca space of Fig 3.15. Most evident from Fig 3.15 is the dominance of Na^+ within all vein types forming one trend, and the disproportional amount of data acquired from the vein type (V), likely due to higher-salinity inclusions.

Compositional data was obtained from evaporate mounds forming on top of quartz, as mounds occurring on sulphide minerals typically produced Cu, S, Zn, Fe mounds lacking salts (Fig 3.14 M to P). The results for evaporate mounds from type (I) and (II) veins of the McD I and II faults are similar. The mounds consist predominantly

of Na^+ and K^+ with minor Ca^{2+} and Mg^{2+}, equally proportioned Na^+, K^+ and Ca^{2+} at low concentrations, or rare K^+-rich mounds with minor Na^+, Ca^{2+} and Mg^{2+} (Fig 3.14 C to L). The type (V) vein in the McDougall I fault yielded mounds composed of Na^+ and lesser amounts of K^+ with minor Ca^{2+}. Mg^{2+} within the type (V) vein was not prevalent, only occurring above detection limits in one mound. The data are summarized on the Na-K-Ca ternary plot of Fig 3.15. The mounds within type (I) and (II) veins occurred as either irregular masses, shallow forming subrounded patches appearing as a dendritic interconnected mat or as isolated mounds. The mounds within type (V) veins are millipede shaped with or without the cubic habit of salts as described by Kontak (2004) for Ca^{2+} chloride dominated inclusions and dendritic patches. The dendritic patches of decrepitation mounds within Type (V) veins are well defined and form higher than the substrate compared to Type (I) and (II) vein mounds. The textures of the mounds do not appear to be diagnostic of the composition given that dendritic mounds and irregular masses appear to have similar compositions. As mentioned, decrepitation mounds are rare within type (I) and (II) veins, but their absence is consistent with the low-salinity inclusions determined from microthermometry (~6-16 wt% NaCl equiv.). Microthermometry obtained from the type (V) vein generally consists of higher salinity inclusions (20-25 wt% NaCl equiv.), correlating well with the higher abundance of evaporate decrepitation mounds.

Evaporate Mound Interpretation

The depression of the ice-melting temperatures indicates that fluid inclusions within of the McD and C faults and Corbet deposit are more complex then a simple H_2O-NaCl system, and must contain cations of K^+ and Ca^{2+} (minor Mg^{2+}, S) (Fig. 3.6) and for

this reason, salinities are reported in wt% NaCl equivalent (equiv). Microthermometry results from the McD faults indicate that the rare high salinity and low temperature fluids plot in the same cluster as the pyrite bearing sample, thus all McD fault samples had the potential to precipitate salt mounds despite their overall low salinity. The analysis of the mounds indicates 3 populations within the data. There are 2 distinct populations that are dominantly Na-K rich and to a lesser extent Na-Ca rich, and a third population that is a Na-K-Ca mixture (Fig 3.15).

The various compositions of evaporate mounds indicate the following: 1) In the Na-K-Ca ternary plot, the data is concentrated along the Na-K side with proportionally higher concentrations of Na^+ indicating that the fluids are best represented by the NaCl-H_2O system, 2) fluids from the McD I/ II faults and the Corbet deposit type I and II veins have proportionally higher Ca^{2+} values then the type V pyrite bearing vein, representative of sample MDI-03-15 which plots along the Na-Ca trend. These results suggest a distinctly Ca^{2+} bearing fluid is part of the hydrothermal discharge system, and 3) McD I sample SZ-MDI-03-15 represents dominantly Na-K fluids mixing with Ca^{2+}, but the proportion of Ca^{2+} to Na-K is unexpected considering eutectic temperatures suggest FIAs with a Ca^{2+} cation. The cluster of Ca^{2+}-bearing analyses away from the Na-K ternary suggests these cation mixtures (fluid mixtures) can occur elsewhere in the hydrothermal system.
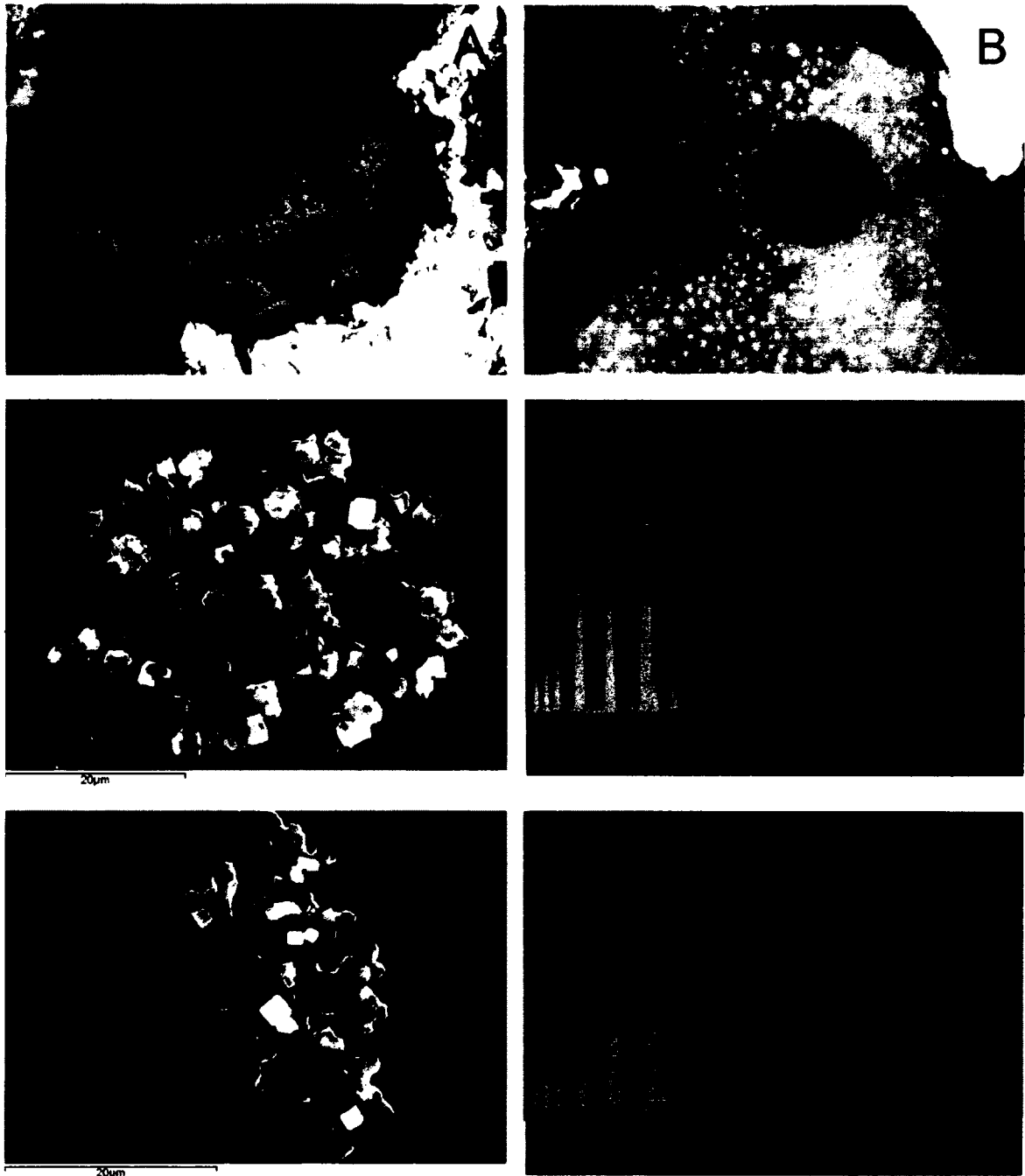
Figure 3.14 A) Dendritic masses of decrepitation salt mounds forming on mosaic textured quartz and surrounded by chalcopyrite, sample SZ-MDI-03-15. B) Anhedral masses of salt mounds forming on quartz and surrounded by fine trails of salt from decrepitated inclusions, sample SZ-MDI-03-15. c) SEM-EDS image of salt mound in photo (b). D) SEM spectrum #1 from SEM image (c) of NaCl with trace K. E) Dendritic salt mound with cubic salt crystals in sample SZ-MDI-02-15. F) SEM-EDS spectrum of cubic salt "Spectrum 2" of image (e) similar in composition to the irregular mound in images & spectrum of C & D of NaCl with trace amounts of K^+.

106
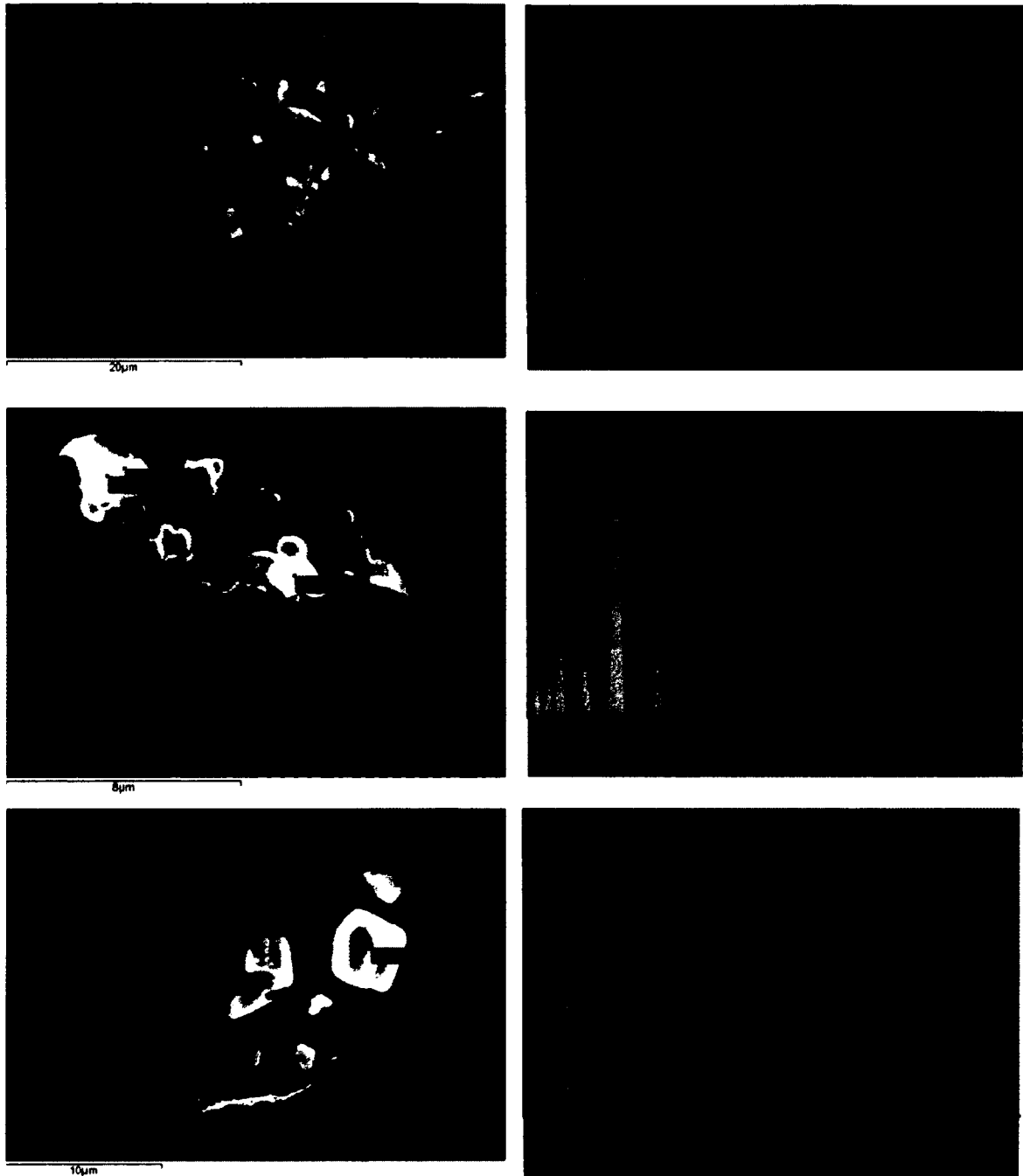
Figure 3.14 con't G) Dendritic patches to individual salt crystals on quartz in sample SZ-MDI-03-15. H) SEM-EDS spectrum is similar to photo C & E despite forming varying textures. I) Amorphous crystals of salt decrepitation mounds in sample SZ-MDI-03-15. J) SEM-EDS spectrum indicating the presence of Ca^+ in addition to NaCl. K) Breached inclusion of sample SZMDI-03-09. L) SEM-EDS spectrum of breached inclusion of image K with possible trace Ag.
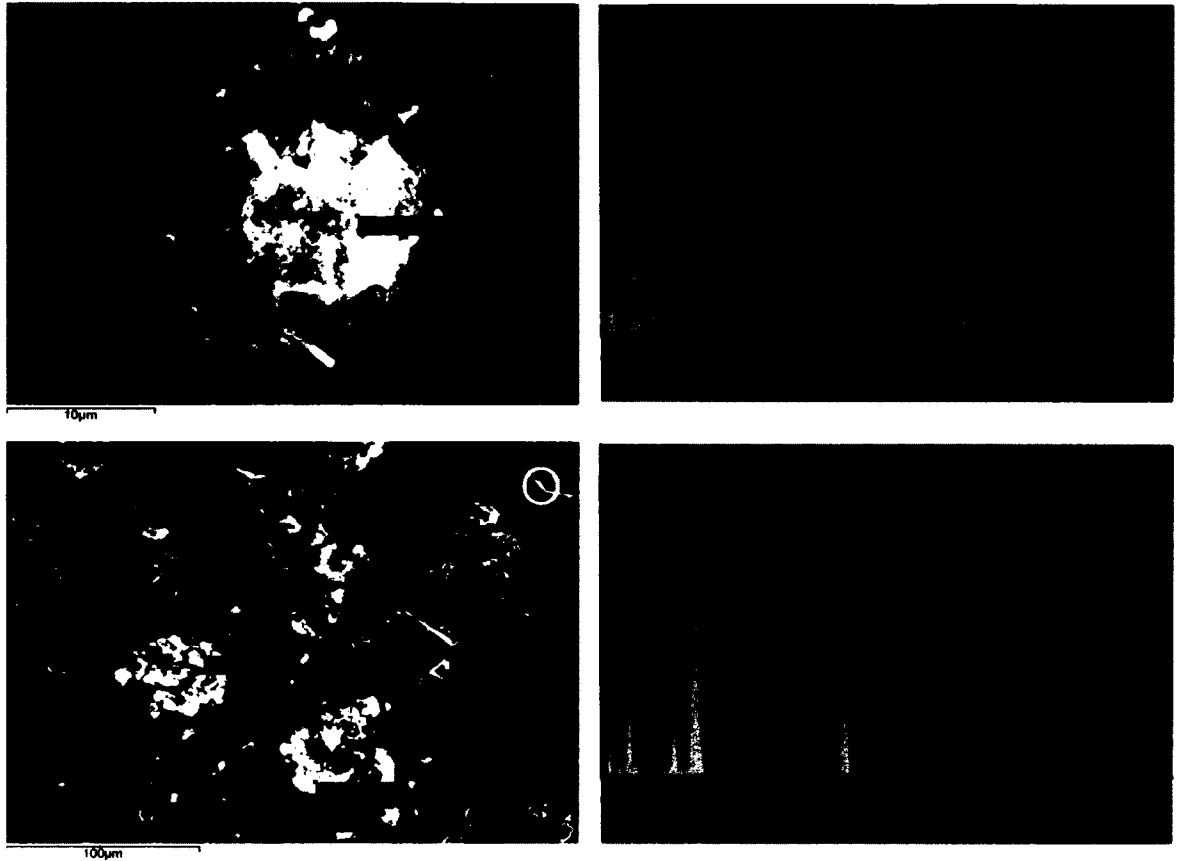
Fig 3.14 con't M) Anhedral irregular mound on quartz of SZ-MDI-03-13 sample N) SEM_EDS spectrum of irregular mound in image (m) of CuS_2 with trace amount of Zn. O) Image of quartz/sulfide contact with irregular salt mounds forming on both minerals in a Corbet Deposit sample (CS-1). P) FeS_2 with salt mounds bearing significant Ca^+ cation.
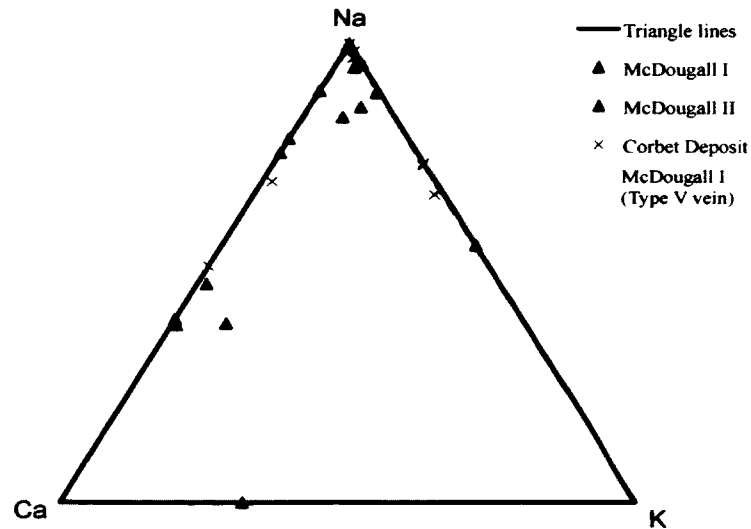
Fig 3.15: Na-Ca-K Ternary plot of SEM decrepitation mound analysis. Cation concentrations are normalized to 100%. The stippled section represents 48 data points analyzed from the McDougall I (Type V vein) pyrite bearing vein.

Gas Chromatography

GC Procedure

Gas chromatography (GC) was performed on selected samples of quartz and

chalcopyrite to determine the bulk chemistry of the volatile phases visible in Type 2

inclusions. The eutectic temperatures measured from Type 2-s-H_2O-CO_2-CH ± M

inclusions suggest the presence of CH_4 and N_2 in CO_2 dominated inclusions and the GC

technique was used to test for their presence. It should be noted that GC provides a bulk

analysis derived from the two major inclusion assemblages, resulting in a mixed signal

from aqueous Type 1 and volatile-bearing Type 2 inclusion which is unavoidable.

Although the results do not represent a single concentration of Type 2-s-H_2O-CO_2-CH ±

M inclusions, they can be used to confirm the presence of simple hydrocarbons and can

be compared to bulk analysis obtained from modern, active seafloor hydrothermal vents.

Hydrocarbons species analysis was performed on 5 samples (1 duplicate) of

quartz from the McD I fault and 7 samples (4 duplicates) from the McD II fault.

Hydrocarbons species analysis of chalcopyrite was also attempted with a total of 4

samples (1 duplicate) from the McD I fault and 5 samples (1 duplicate) from the McD II

fault using the GC at the University of Toronto. Samples were selected based on

microthermometric data and the size of the hand sample available for multiple GC runs

and duplicates. Sample were crushed and sieved to multiple fragment sizes ranging from

~1mm to ~3mm, allowing for sufficient separation and liberation of chalcopyrite and

quartz. Due to the penetrative nature of the chalcopyrite between comb and mosaic

textured quartz, the quartz samples may contain minor amounts of chalcopyrite

contaminants. The samples then undergo 2 runs of multiple deoxygenated water (DIW)

cleaning and drying at 40°C on a hot plate for up to 4 hours, and then they are cleaned

and left overnight to dry. Mineral volumes for quartz samples were generally ~1.3g, and

~2.6g for chalcopyrite samples. The instrumental and sample preparation procedure

follows those outlined by Bray and Spooner (1992). Samples were loaded into 4 stainless

steel crushing columns and heated overnight at 110°C in a steady stream of He gas. The

columns are followed by an on-line HP 5890 gas chromatograph equipped with both a

Photoionization Detection (PID) and a 1,2,3-trichloropropane (TCP) detector enabling

bulk analysis of volatile compounds of N_2, H_2O, CO_2, C1-C5 hydrocarbons, COS and

SO_2 (Bray and Spooner, 1992). Samples are calibrated against a Scott Standard Gas

Mixture 216 and Supelco Cat. No. 501697 Mixture 234 prior to each run and the results

are presented in table form in Appendix 6.

GC Results

Quartz samples from the McD I fault yielded the following analyses in mole % :

99.06-99.77% H_2O, 0.10-0.32% CO_2, 0.08-0.21% CH_4, 0.01-0.04% N_2, 0.01-0.03%

COS, 0.004-0.288% C_2H_4-C_2H_6, 0.001-0.004% C_3H_4-C_3H_6. The range of volatile

concentrations within the quartz of the McD II fault are higher than in quartz from the

McD I fault with respect to all volatiles and yielded the following results (in mole %):

97.68-98.88% H_2O, 0.30-1.23% CO_2, 0.35-1.16% CH_4, 0.02-0.06% N_2, 0.01-0.05%

COS, 0.004-0.258% C_2H_4-C_2H_6, 0.001-0.014% C_3H_4-C_3H_6. CO_2 is the dominant volatile

within the McD faults, which is supported by the GC analysis, but the high concentration

of CH_4 at almost similar concentrations to the CO_2 was unexpected, despite

microthermometry indications of a large population of almost pure CO_2 inclusions. The

proportion of hydrocarbons between species are also consistent, with only two

discrepancies from samples SZMDII03-16-2 and SZMDII03-16-4, where CH_4 is the dominant volatile over CO_2.

The analyses of the quartz obtained from the GC study are consistent with the microthermometry of Type II inclusions, as Type 2-s-L(CO_2)-V inclusions with eutectic temperatures occurring between -56.0 and -56.3°C are consistent with a higher percentage of CO_2. Similarly, Type 2-s-L(CO_2)-V inclusions and Type 2-s-H_2O-CO_2-CH±M inclusions with a $T_m(CO_2)$ range between -58.2 to -60.9°C are suggestive of more complex hydrocarbons in addition to CO_2, which is confirmed from the GC analysis since the T_{triple} of CH_4 is -182.5°C, thus lowering the total $T_m(CO_2)$. Based on microthermometric data and using figure 6.19b of Shepherd et al. (1985), 16-25 mole% CH_4 in the eutectic temperature limits mentioned above could be responsible for the CO_2 melting point depression. It should be noted that the GC analyses may also include brine inclusions (Type 1) that may contain some degree of diluted hydrocarbons and CO_2. Although this cannot be confirmed through GC analysis, it may account for the discrepancy in the T_m values of Type 1 inclusions within FIAs and a higher percentage of CH_4 volatiles although not visibly identifiable. Additionally, the higher volatile concentration in the McD II fault may be accounted for by comparatively more visible Type II inclusion as compared to the McD I fault. The GC study of the quartz also identified additional complex hydrocarbons to those already noted, unfortunately they occurred at lower concentrations or were undetected and were not considered in the analysis.

To better characterize the fluids and volatiles within the McD faults, sulfide separates from the two faults were analyzed to identify their potential volatile

contribution to the overall system, with a further aim of comparing quartz and chalcopyrite volatiles chemistries to modern sea floor hydrothermal vent systems. The chalcopyrite from the McD I fault yielded the following analysis (in mole%): 99.85-99.98% H_2O, 0.01-0.07% CO_2, 0.01-0.07% CH_4, 0.01-0.03% N_2, 0.01-0.02% COS, 0.001-0.003% C_2H_4-C_2H_6, 0.001-0.002% C_3H_4-C_3H_6. The gas concentrations for the McD II fault chalcopyrite are higher than similar chalcopyrite samples from the McD I fault and generally occur in the same volatile proportions as the equivalent quartz volatile results. The chalcopyrite from the McD II fault yielded the following concentrations: 99.18-99.96% H_2O, 0.01-0.39% CO_2, 0.03-0.25% CH_4, 0.01-0.03% N_2, 0.02-0.09% COS, 0.002-0.179% C_2H_4-C_2H_6, 0.001-0.006% C_3H_4-C_3H_6. Although the values from the gas concentrations in chalcopyrite are lower than the equivalent quartz samples, positive trends of volatiles ratios/gas plots which include N_2, CO_2, CH_4 suggest similar source(s) (Fig 3.16 A to E).

GC Interpretation

In summary, the GC analysis indicates the presence of volatile components in the following order of abundance, $H_2O \gg CO_2 \geq CH_4 > N_2 \geq COS > C2- > C3-$ for quartz and chalcopyrite. Variable volumetric ratios within CO_2-rich inclusions of the McD II fault and eutectic temperatures below -56.6°C (range from -58.2 to -63.5 C) indicate heterogeneous trapping of more than one phase in the same inclusion and, as a result, the mixtures of CO_2 with nitrogen and simple hydrocarbons were expected for this VMS system. Ratios of a combination of the various volatile components show positive correlations that are suggestive of phase separation and fluid mixing when the combined gases are plotted in Fig 3.16 D.
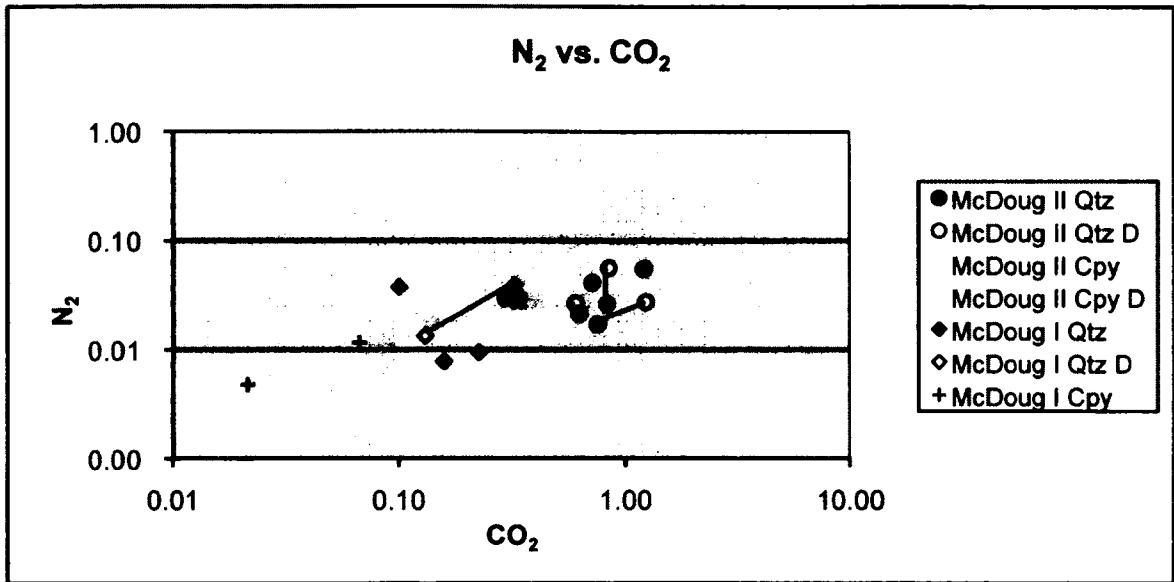
Figure 3.16 A: N_2 versus CO_2 plot of McDougall I & II quartz and chalcopyrite gas volatiles (mole %). Duplicates are marked by open-spaced symbols and tie-lines indicate sample pairs. McDougall II samples produced higher volatile yields.
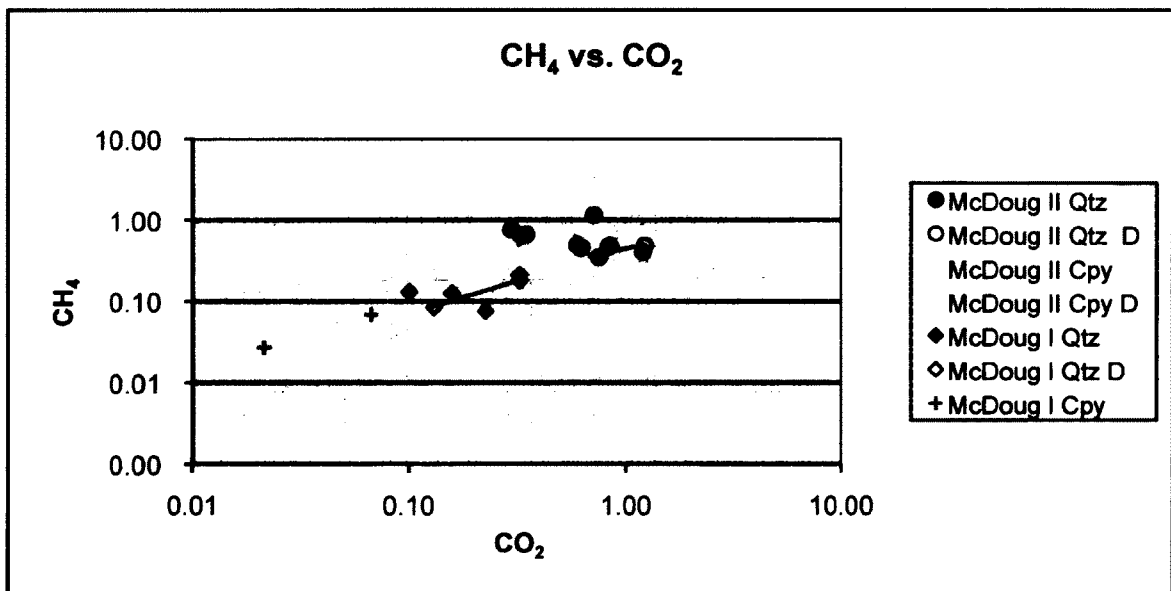
Figure 3.16 B: CH_4 versus CO_2 plot of McDougall I & II quartz and chalcopyrite gas volatiles (mole %). Duplicates marked by open-spaced symbols and tie-lines indicate sample pairs. McDougall II samples have higher volatile content but fall within the same trend as the McDougall I quartz and chalcopyrite samples.

113
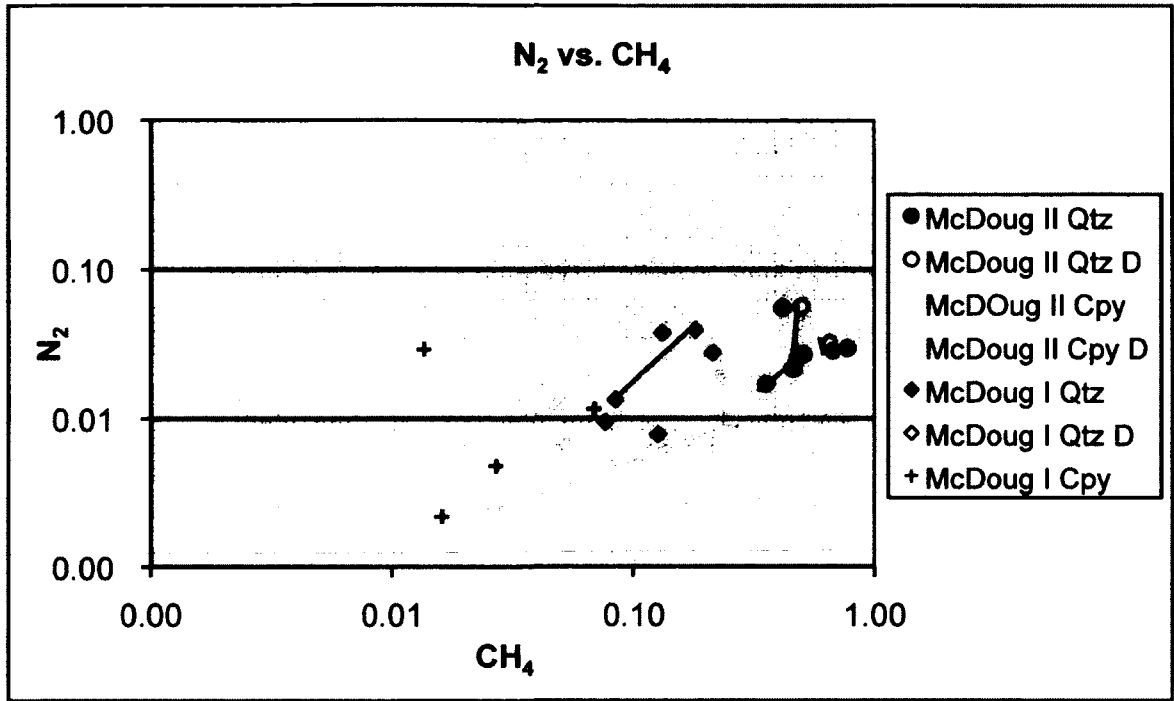
Figure 3.16 C: N_2 versus CH_4 plot of McDougall I & II gas volatile analysis (mole %) from quartz and chalcopyrite. Duplicates are marked by open-spaced symbols and tie-lines indicate sample pairs.
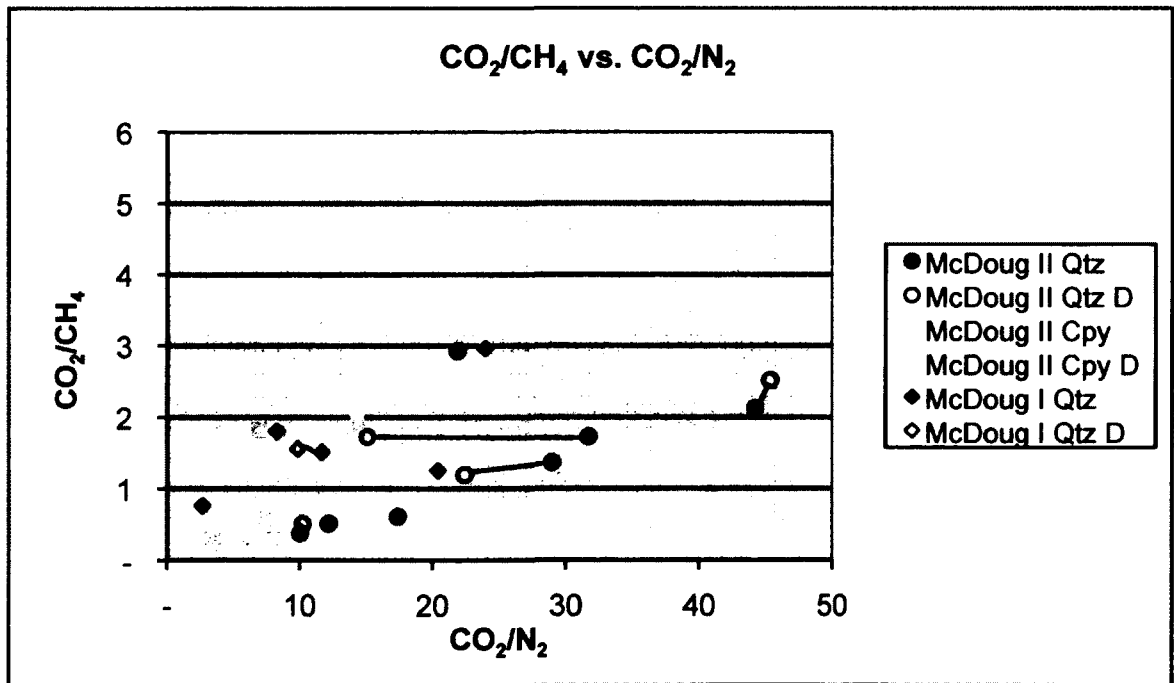
Figure 3.16 D: CO_2/CH_4 versus CO_2/N_2 plot of McDougall I & II gas volatiles (mole %). Duplicates are marked by open-spaced symbols and tie-lines indicate sample pairs.

114
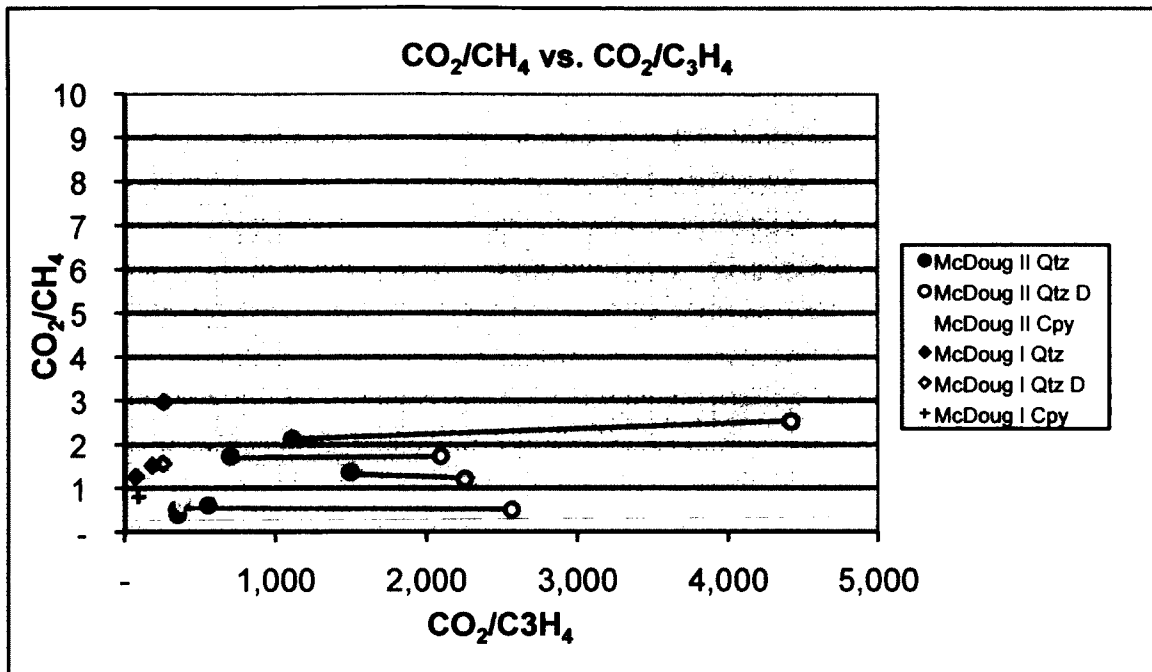
Figure 3.16 E: CO_2/CH_4 versus CO_2/C_3H_4 plot of McDougall I & II volatile analysis (ratio of mole %) of complex hydrocarbons. Duplicates are marked by open-spaced symbols and tie-lines indicate sample pairs.

In Figs 3.16 A to C, all data shows volatile concentrations in quartz and chalcopyrite within the McD II fault to be almost an order of magnitude greater than in quartz and chalcopyrite in the McD I fault, but both show positive correlations between volatiles, which suggests subsea-floor phase separation (de Ronde et al., 1997). Within all volatile plots, concentrations for the McD I fault quartz samples overlap with chalcopyrite displaying positive correlations. de Ronde (pers. comm.) described some of the highest CH_4 concentrations relative to CO_2 from a plume water sample at the Monowai volcano, Kermadec Arc in 2004, 2-3 weeks after its eruption. Enrichment of CH_4 has also been attributed to organic matter in high-temperature fluids (Lilley et al., 1993) where CO_2 and CH_4 occurred in approximately equal amounts as in the TAG

hydrothermal fluids. The high CH_4 concentrations in the McD faults may be a product of a similar volcanic event, saturating the fault with hydrocarbons over a brief time interval.

During phase separation, less soluble gases preferentially partition into the vapour phase in the order of C2- and C3- hydrocarbons, N_2, CH_4 and CO_2 (Giggenbach, 1980; Graupner, 2000). Thus, the residual liquid will increase in lighter hydrocarbons and this may account for the significantly lower N_2 values in the McD faults, lower than concentrations observed in modern black smoker environments. Plots of N_2 vs. CO_2 (Fig 3.16 A) and N_2 vs. CH_4 (Fig 3.16 C), demonstrate N_2 concentrations an order of magnitude lower than CO_2 and CH_4 concentrations. The low N_2 concentrations may indicate early intense fluid fluxes or pulsed CH_4 discharge, but an explanation for this variability is not presently known. The N_2 concentration in Fig. 3.16 D show positive correlation, and are consistent with phase separation (Thomas and Spooner, 1992). These volatile plots clearly demonstrate that data from an Archean VMS system at Noranda are comparable to data from modern seafloor VMS hydrothermal systems, and this will be addressed in the discussion section.

Gas Chromatography – Isotope Ratio Mass-Spectrometry

GC-irMS Procedure

The on-line gas chromatography continuous flow-isotope ratio mass-spectrometry (GC/C-irMS) method is a newly developed extraction method for carbon and hydrogen isotope determination in complex mixtures of fluid inclusion volatiles (Potter and Longstaffe, 2007). Four samples from the McD I fault and six samples from the McD II fault were analyzed using this technique (including duplicate samples) to determine $\delta^{13}C_{CH4}$ and $\delta^{13}C_{CO2}$ values that would potentially provide fluid/gas source data. The

procedure for sample preparation is similar to that of the GC technique with samples for

GC-irMS picked from the finer crushed material previously not used for GC analysis.

Crushed quartz in the range of 1-3mm in size was prepared in 1-1.3g sample sizes and

cleaned according to procedures outlined for GC. The GC-irMS method was developed

and is described in detail in Potter and Longstaffe (2007), with the analyses carried out by

Dr. Potter at the Department of Earth Sciences, University of Western Ontario. In

summary, the samples are loaded into 3 crushers slightly modified from the design of

Bray et al. (1992) and flushed overnight with He while heated to ~120°C. The lines

leaving the sample chamber are equipped with multiple mesh filters for trapping particles,

a cryogenic trap for H_2O, a molecular sieve trap to capture gases and a high flow - low

flow valve to maximize gas analysis through the mass spectrometer. Captured gases are

sent through a HP 6890 GC with a Poraplot Q column and then sent through a

$CuO/NiO/Pt$ reactor for combustion of hydrocarbons to CO_2 for δC^{13} analysis. The

samples are then passed through a ThermoFinnigan GC/C III interface and eventually

analysed using a ThermoFinningan Delta^{PLUS} XL continuous flow-isotope ratio mass

spectrometer (Potter and Longstaffe, 2007). A total of 3 aliquots were analysed per

sample, with each sample containing of a duplicate for comparison of accuracy.

GG-irMS Results

The $\delta^{13}C_{CH4}$, $\delta^{13}C_{CO2}$ analytical results are summarized in Appendix 8 and by

Potter et al. (2007). The analytical results represent a bulk analysis of Type 1 and Type 2

inclusions as previously mentioned for the GC method. The three aliquots analyzed from

the same sample, including the duplicates, produced a range in error between ±0.1 to

±2.3‰, with the difference between the sample and the duplicate falling within this

117

range. The only exception is from one sample (MDI-03-06-2) where the difference

between the duplicate and the original sample is as high as 5.8‰. The variation between

multiple crushes and between duplicate samples may be accounted for by heterogeneity

within the samples.

The results for the McD I and II faults are generally consistent within the

individual faults but there are potentially different sources of $\delta^{13}C_{CO2}$ and $\delta^{13}C_{CH4}$ for the

two faults. The $\delta^{13}C_{CO2}$ results for the McD I fault range from -22 to -13 ‰, and $\delta^{13}C_{CH4}$

values are in the range of -44 to -35‰. The McD II fault results range from -5.0 to

+4.7‰ for $\delta^{13}C_{CO2}$ and -18.9 to -26.8‰ for $\delta^{13}C_{CH4}$. Samples used for GC-irMS from the

McD II fault, correspond to locations selected for microthermometry, further showing the

relatively consistent microthermometric results across the fault also are reflected in

similar consistent GC and GC-irMS analysis that are fault specific. The range in results

for the McD II-19 samples is between -5 to 0 ‰ for $\delta^{13}C_{CO2}$ and from -20 to -19 ‰ for

the $\delta^{13}C_{CH4}$ values. Alternatively, the McD II-16 samples range from 0 to +5 ‰ for

$\delta^{13}C_{CO2}$ and from -18.9 to -20.1 ‰ for $\delta^{13}C_{CH4}$.

GC-irMS Interpretation

Potter et al. (2007) suggested that based on $\delta^{13}C_{CO2}$ results, the McD II fault

contains fluids derived from a magmatic (~ -5‰) and a seawater-derived source (~ 0‰).

The McD I fault is more difficult to interpret as $\delta^{13}C_{CO2}$ data from Potter et al., (2007)

suggest a more ^{13}C-depleted source of (~ -20‰), indicative of fluids derived from a

sedimentary source. Finally, equilibration temperatures of 300-400°C were calculated

from the ΔCH_4-CO_2 data of Potter et al., 2007, and they are similar to the

homogenization temperature determined through microthermometry, and suggested by the decrepitation temperatures.

Fluid Inclusion Data

Fluid Inclusion Data Interpretation

Fluids trapped within FI in quartz and sphalerite from VMS deposits and in quartz from quartz-sulfide veins in discordant alteration pipes at Noranda both have PTX characteristics within the range of similar Archean VMS environments (de Vries and Touret, 2006; Ioannou, 2004; Weiershäuser, 2004; Drieberg, 2003; de Ronde et al., 1994; Farr, 1984). Salinity and minimum trapping temperature variations (T_h) of Type 1 FIAs within the McD I, II, C faults, and the Corbet deposit range from ~6-16 wt% NaCl equiv., and ~140-230°C, with minor FIAs extending beyond this range to 1-28wt% NaCl equiv. and T_h from 75-300°C. Type 2 aqueous-carbonic inclusions comprise <~5% of the total microthermometry data set with decrepitation temperature between 294-477°C and occur in close proximity to mineralization within the McD II fault. Visible CO_2 bearing inclusions are noticeably lacking in the McD I fault and appear to be a dissolved gas phase in saline brines (Type 1 <3wt% NaCl equiv. inclusions) with salinities below the lower limit of probable Archean seawater values (~3.1 wt% NaCl equiv.; de Ronde et al., 1997). The variations in the salinity and minimum trapping temperature of FIAs are expected, as they represent the range in composition and temperature of fluids that moved into and upward through the faults contemporaneously over time resulting in a complex range of T_h and T_m of the FIAs. In addition, trends defined by the variability in salinity and temperature of the FI and the presence of CO_2 bearing inclusion may help in the interpretation of subseafloor modification mechanisms such as:

1. Post-entrapment modification.

2. Salinity shifts resulting from fluid dehydration modified via fluid-rock interaction and mixing within the discharge conduit.

3. An overall decrease in T_h with an increase in salinity caused by boiling and phase separation of fluids with brine generation and segregation of a vapour (supported by CO_2 inclusions).

4. Mixing of magmatic fluids of variable salinity with seawater or variably evolved seawater.

The fluids are interpreted to be evolved, seawater-dominated hydrothermal fluids (Franklin et al., 1981; Lydon, 1984; Seyfried et al., 1988; Franklin et al., 2005; Gibson and Galley, 2007) produced by water-rock interactions during seawater incursion into and convection within the volcanic rocks beneath the sea floor, with or without a magmatic contribution (Galley, 1993; Franklin et al., 2005). The range in fluid compositions and minimum trapping temperatures is consistent with a long-lived fault and hydrothermal conduit that provided a pathway for fluids ranging from seawater, to variably evolved sea water modified via fluid-rock interaction. Evolved seawater fluids were derived from different levels of the semiconformable alteration zones where the temperature ranged from <100°C during zeolite facies metasomatism to >300°C during epidote-quartz alteration (Galley, 1993a) and where water-rock ratios ranged from >10 to <1 (Gibson and Galley, 2007; Fig. 3.17). Evolved seawater fluids entered the fault from various levels within the semiconformable alteration zones and mix with fluids from deeper within the hydrothermal system upon accent, resulting in an extremely dynamic and

compositionally heterogeneous fluid environment (Fig 3.17) with turbulent fluid mixing

between brecciated wallrock fragments.
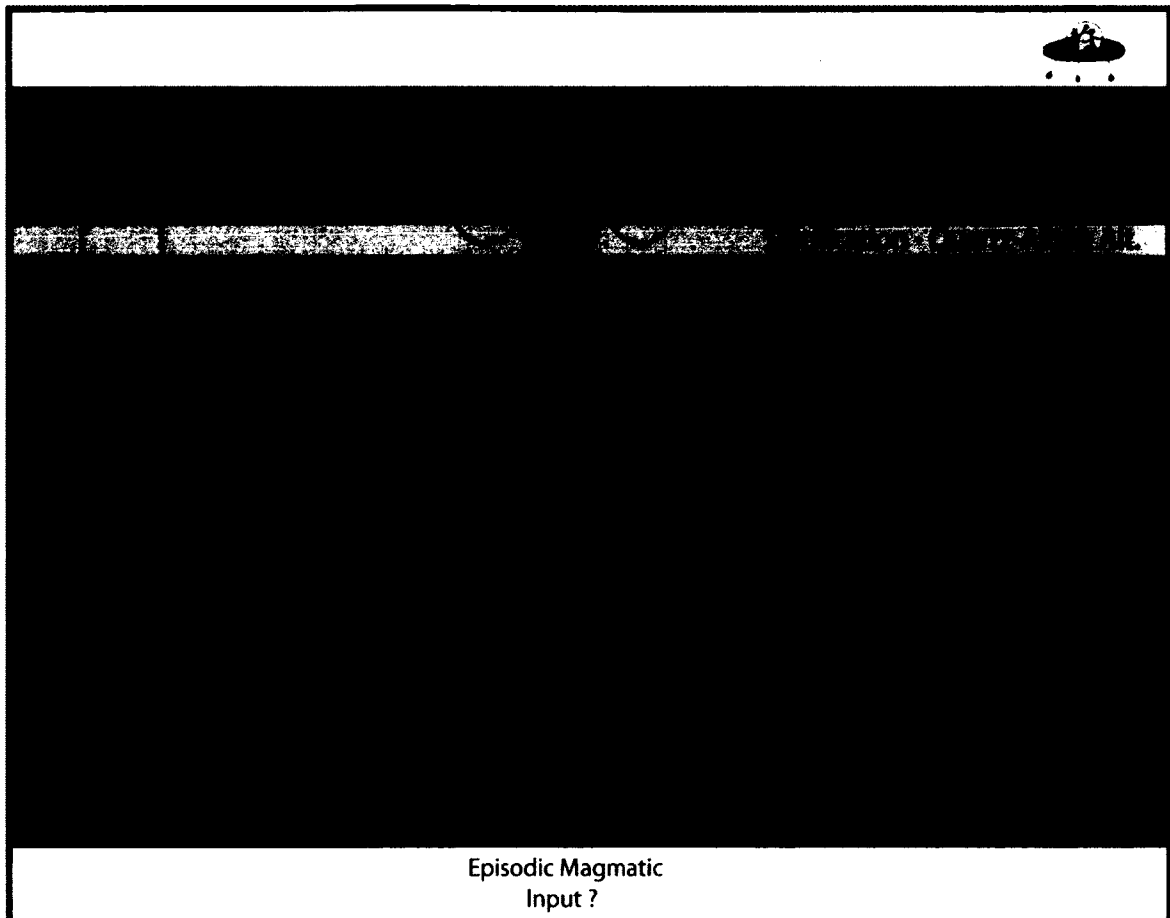
Figure 3.17: Evolved seawater modified through interaction with wall rocks in semiconformable alteration zones continuously enters the synvolcanic fault from different levels within the alteration zone that define Archean geothermal system. Thus evolved seawater fluids entering the fault have different compositions (salinities) and different temperatures, but all are variably acidic and contain dissolved silica. Upon entering the fault the fluids interact and mix with fluids ascending within the fault resulting in an extremely dynamic environment where the composition and temperature of the ascending fluids are continuously changing.

Post-entrapment modification

Fluid inclusions that form homogenous fluids trapped under conditions following

"Roedder's Rules" where inclusions remain at a constant volume after trapping and

nothing is added, or removed from the inclusion post-trapping (Roedder, 1984; Bodnar,

2003), can be used with certainty to reconstruct the thermobaric history of the system (Bodnar, 2003). Often though natural processes may change the location, shape, volume and composition after initial entrapment and during uplift and burial (e.g. Goldstein and Reynolds, 1994). One must assess the degree to which these changes have altered the fluid inclusions from their original entrapment fluid. Fluid inclusions experiencing re-equilibration typically show recognizable textures (Goldstein and Reynold, 1994) such as necking (Roedder, 1984) or secondary haloes around parent inclusions (Sterner and Bodnar, 1989). Where textural evidence is not available, fluid inclusions may have re-equilibrated from stretching due to overheating, leakage, diffusion, or partial decrepitation and refilling (Roedder, 1984; Shepherd et al., 1985; Wilkinson, 2001), and are only evident during microthermometric analysis.

According to Bodnar (1993), the P-T path should first be assessed before discussing textural features. Hannington et al. (2003) have shown that the Mine Sequence volcanic rocks are at greenschist metamorphic grade and that this metamorphism and resulting mineral assemblages are a product of a primary hydrothermal metamorphism that remained stable during later greenschist facies regional metamorphism. Re-equilibration during regional metamorphism may have occurred, but any re-equilibration due to burial is interpreted to be minimal since the greenschist facies regional metamorphism and greenschist facies alteration likely do not have significantly varying P-T paths. In thin section, macroscopic features interpreted during "hot-cathode" CL analysis show minimal re-equillibration textures in the quartz which were typically associated with recrystallization along quartz-cpy margins. Where textural features diagnostic of re-equillibration were suspected of fluid inclusions, these FIs were avoided

(Sterner and Bodnar, 1989; Vityk and Bodnar, 1995). Overheating of fluid inclusions in the laboratory leading to stretching and ultimately varying homogenization temperatures was avoided during fluid inclusion analysis by limiting measurements on individual thin section "chips". Evidence from T_m-T_h plots for FIAs show narrow subsets of measurements distinct from the larger cluster of data in the 6-16wt% NaCl equiv. mode suggests microthermometric measurements were carefully acquired and re-equilibration was likely minimal since all the data are not skewed together or considerably varied. Since stretching or necking can't produce the narrow range of salinities measured (Shepherd et al., 1985), phase separation, fluid mixing with seawater and for the most part, the intrinsic variability in the temperature and salinity of evolved seawater fluids are likely responsible for the overall variability in the data.

Salinity and temperature variations between fluid inclusions are expected in this hydrothermal system since inclusions are not expected to precisely seal synchronously and, therefore may not trap fluids with identical P and T. Teinturier and Pironon (2003) experimentally recorded variances within individual FIAs along microfractures due to changes in TX conditions, a similar situation expected within the McD and C faults. Goldstein (2003) also recognized time delays in sealing of individual FIAs, and thus defined FIA assemblages as each FIA representing the finest temporal resolution possible as to timing of initial closure of the inclusion vacuoles. Loucks (2000) suggested that hydrothermal breccias in epizonal hydrothermal systems, similar to that proposed for the McD and C faults where breccias likely occurred formed by overpressuring and fluid trottling. These fault systems are very dynamic and over the duration of crystal growth within them the P, salinity and T variations of fluids are large and occur relatively rapid.

Therefore, the range in fluid salinity, pressures and homogenization temperatures

displayed by primary, pseudosecondary and secondary FIAs should be expected in this

dynamic hydrothermal up-flow environment.

Salinity variations resulting from sea water-dominated hydrothermal fluids via fluid-rock interaction

At Noranda, semi-conformable, syn-volcanic alteration is manifest in the

development of four alteration types, superficially resembling regional metamorphic

facies (previous alteration discussion: Gibson, 1990; Gibson et al., 1993, Galley, 1993;

Powell, 1994; Santaguida, 1999; Hannington et al., 2003). Semi-conformable alteration

with increasing depth and temperature and on approaching upflow zones includes

regional K-Mg metasomatism (50-140°C); a transitional zone of Na-Mg assemblages

resulting from spilitization (140-300°C); silicification producing quartz-albite

assemblages (300-400°C) and epidote-quartz alteration (Ca-Fe metasomatism) defining

temperatures at the greenschist-amphibolite facies boundary (Galley, 1993; Gibson and

Galley, 2007). Minimum trapping temperatures of fluid inclusions ranging from 140-

230°C are consistent with the discordant chlorite and sericite alteration zones surrounding

the McD I, II and C-shaft faults, which are superimposed on the regional

semiconformable alteration assemblages. Higher temperature fluids (i.e, in upwards of

400°C for individual inclusions) that could not be grouped into FIAs are rare. They are

typically associated with the Corbet ore deposit and not the fault structures, although

calculated temperatures based on bulk CO_2/CH_4 isotope from the McD I/II faults suggest

temperatures in the 300-400°C range. A minimum trapping temperature range of 140°C -

230°C between the various faults and the Corbet orebody (Fig 3.7) may reflect similar

fluids, suggesting that the hydrothermal system comprises a complex combination of evolved sea water compositions that have undergone similar mixing and cooling histories prior to entering the faults.

The overall decrease in fluid temperatures and corresponding increase in salinity (isothermal) via fluid-rock interaction or mixing within the fault, are evident by the near horizontal trend from the earliest McD I/II primary fluid inclusions (lowest salinity) to later assemblages (higher salinity pseudosecondary and secondary FIs) (Fig 3.18) associated with mineralization. Primary FIAs are most prominent near 6 wt% NaCl on T_h vs. wt% NaCl equiv. plots, and may represent fluid salinities that were typically present during the onset of comb-textured quartz growth. Primary FIA salinities >6 wt% NaCl but <13 wt% NaCl equiv. may represent silica saturated fluids that were metal poor, texturally appearing as primary FIAs but may have been trapped during "breaks" in mineralization. The McD I & II faults also show an overlap of secondary FIA clusters in the 8-14 wt% NaCl equiv. interval, a similar interval (8-11 wt% NaCl equiv.) could to be associated with chalcopyrite-bearing primary inclusions at the Hellyer VHMS deposit (Zaw et al., 1996). Overlapping of secondary and pseudosecondary inclusions within this interval suggests assemblages were possibly misinterpreted or more likely that TX varied continuously, as fluids of different composition and temperature from various semiconformable horizons entered and traversed these long lived faults.

Fluid "dehydration" caused by the growth of large amounts of hydrous silicate minerals that did not incorporate Cl (eg. chlorite) throughout the semiconformable alteration zones likely caused an increase in the salinity of these reacted fluids. For example, a significant increase in fluid salinity has been obtained in experiments run at

Ranges of FIAs of the McDougall I/II, C-shaft faults and the Corbet Deposit
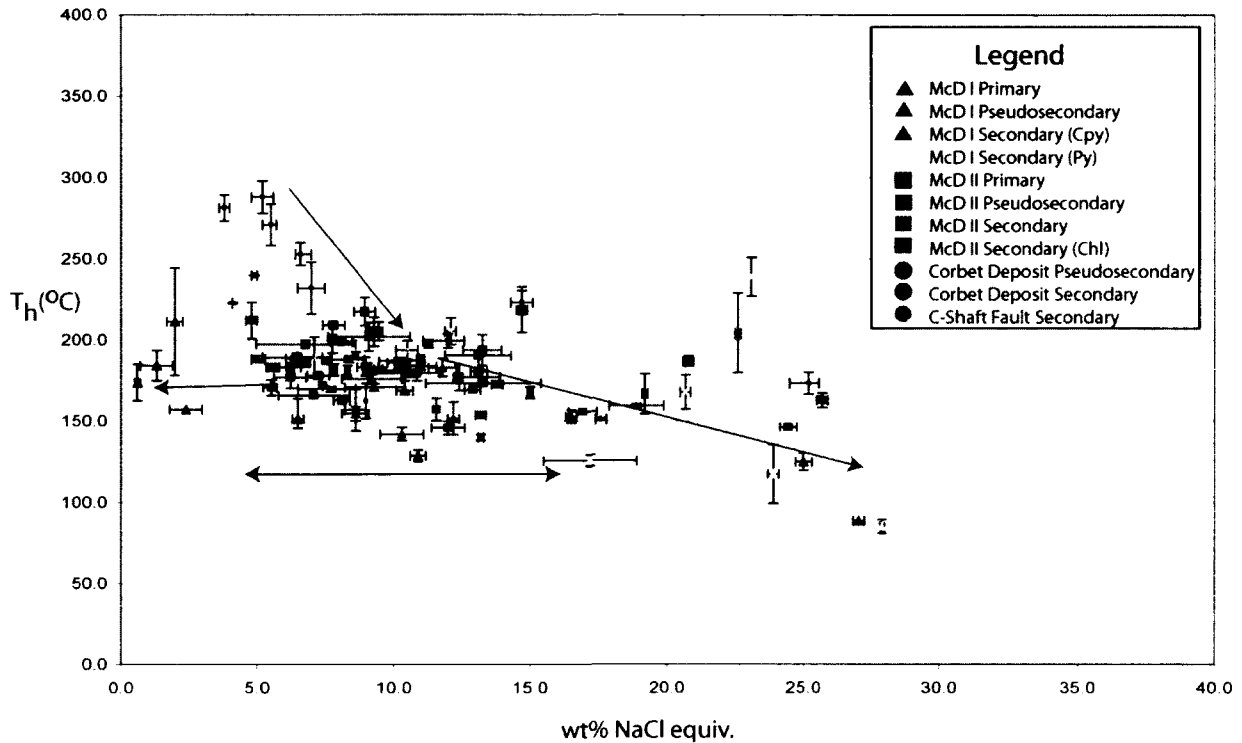
Fig 3.18: Possible mixing or fluid "dehydration" trend indicated by the blue arrow in the 6-16wt% NaCl salinity range. Red arrows indicate a possible boiling trends with the presence of CO_2 inclusions as the possible coexisting vapour phase.

low water-rock ratios and proper P-T conditions (Cathles, 1983). Furthermore, Kelley et al., (1992) has shown that dehydration reactions under greenschist facies conditions with limited brine-rich fluid mixing can result in salinity variations from 70% below to 200% above normal seawater concentrations for FIs from the Troodos Ophiolite, Cyprus. This salinity range is well within the range of Noranda fault fluid inclusion salinities. In addition, Hanley, et al., (2004) has shown a water soluble Cl⁻ enrichment and increased concentrations of bulk-rock Cl⁻ for distances of at least 150m from footwall sulfide mineralization at the Strathcona mine in Sudbury, Ontario, Canada. At Strathcona, the elevated Cl⁻ concentrations were attributed to elevated modal abundances of Cl-bearing

hydrosilicates minerals (biotite, actinolite, chlorite) within alteration haloes associated with the mineralization. Low salinity fluids percolating upwards through anhydrous minerals such as pyroxene and apatite has been shown to rapidly increase Cl^- concentrations in layered intrusions of the Bushveld and Stillwater complexes (Mathez and Webster, 2004) where the Cl^- concentration is highly dependent on the melt composition. These examples suggest that fluid dehydration processes likely increased fluid salinities in the McD faults, but where fluid salinities are < 6 wt% NaCl and > 16wt% NaCl equiv., phase separation may also have been a contributing factor to salinity variations.

The Corbet deposit has FIAs in the 6-16wt% NaCl equiv. range, overlapping with the fluid temperatures and salinities recorded in the McD faults. Similar T_h/T_m ranges suggest a similar semiconformable association, but extending up to ~260°C within the 8-16wt% NaCl equiv. range and upwards of 300°C in the 5-8 wt% NaCl equiv. fluid salinity interval. A total of 22 FIAs in the Corbet deposit show a continuous dilution trend (Hedenquist and Henley, 1985) from high temperature and low salinity fluids to moderate salinities (~9wt% NaCl equiv.) and low temperatures ~150°C. Salinity variations in this range may reflect mixing of the relative proportions of two end-member fluids, a low salinity/high temperature fluid in the range of 5-8 wt% NaCl equiv. (240-300°C) and evolved seawater fluids with salinities of ~16-35wt % NaCl equiv. and generally lower in temperature. More likely, this trend suggests boiling (Fig 3.18) near the seafloor and mixing with ambient seawater in the sulphide mound as high temperature and low salinity fluids trend towards decreased temperatures over a relatively small salinity range.

It must be emphasized that none of the fluid inclusion compositions (and temperatures) from this study can be directly compared to evolved sea water fluids that have been modified by a specific semiconformable alteration type, not until targeted fluid inclusions studies specific to alteration assemblages within the Noranda cauldron are completed. However, the predominant temperature and salinity range from inclusions of the McD, C-faults and Corbet deposit are also prevalent within other Archean VMS systems. Dreiberg (2003) has shown secondary fluids in the Strelley Granite associated with epidote to have temperatures of 114-222°C, and salinities of 0.8-15.6 wt% NaCl, but no source was suggested.

Phase Separation and CO_2 bearing inclusions

The CO_2 vapor dominated inclusions are interpreted to be the product of deep brine segregated vapors derived from a breached hydrothermal cracking zone (high temperature reaction zone) and exsolved from a homogenous fluid phase (Bischoff and Rosenbauer, 1988, Roedder, 1992) around a high level intrusion or from crystallizing basaltic magmas (Javoy & Pineau, 1991, de Ronde et al., 2005) similar to those that produced basaltic dikes that comprise the Old Waite Paleofissure. This interpretation is not based exclusively on microthermometry, but incorporates isotopic GC-irMS analysis on CO_2 and CH_4, C^{13}, C^{14} isotopes (Potter et al., 2007) suggestive of a magmatic input to the Noranda hydrothermal system. The contrasting phases within the McD II fault may be represented by CO_2 (± simple and complex hydrocarbons) volatile bearing Type 2 (both 3 phase and trapped sulfide/salt) inclusions proximal to Type 1 brine inclusions in the Noranda VMS system. Within the McD I fault, the association of low molar volume CO_2-bearing FIAs with salinities of 1-4wt% NaCl equiv. (150-245°C) with higher salinity

FIAs (16-27wt% NaCl equiv.) also suggests that phase separation may have occurred at some depth in the faults below the sampling location. In addition, the overall trend of decreasing temperature with increasing salinity is an indication of boiling (Figure 3.19) in epithermal systems (Hedenquist and Henley, 1985; Hedenquist et al., 1992), and may be responsible for the association of low salinity inclusions (<sea water) and higher salinity fluids (>16 wt% NaCl equiv.) in the McD I and II faults along the two-phase boundary.

a. · Data point for single fluid inclusion
b. High gas system
Dilution
Boiling and gas loss
-Tm°C
Th°C ➤
Th°C ➤

c. Low gas system
d.
Boiling
Concentration of salinity due to steam loss
Tm due to gas
Tm due to salinity
Dilution of unbolled fluid
Boiling and gas loss
Dilution
-Tm°C
Th°C ➤
Th°C ➤
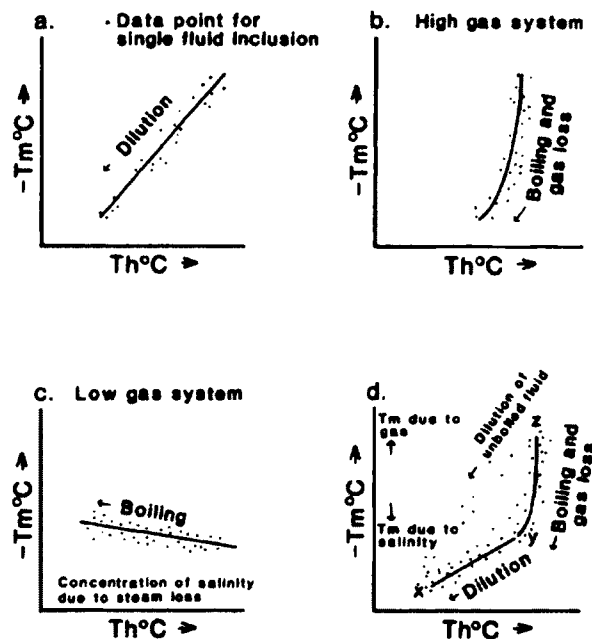
Figure 3.19: Trends of fluid inclusion data from Broadland epithermal Geothermal Field, New Zealand. From Hendenquist and Henley, 1985.

Visible Type 2 CO_2-H_2O (+complex hydrocarbons) and Type 2 fluid inclusions containing multisolids (i.e., chalcopyrite/halite) with H_2O-NaCl brine FIs, in close proximity to sulphide mineralization within the McD II fault, is the best evidence of phase separation deep within the Noranda VMS hydrothermal system associated with the mineralization. Textural evidence of cogenetic CO_2 bearing Type 2 inclusions with Type 1 brine inclusions in the McD II fault would suggest phase separated fluids occurred at

this height within the fault. Unfortunately, microthermometric analysis resulted in varied T_h values within trails that failed to meet the boiling criteria of Ramboz et al., (1982), and this suggests that phase separation likely occurred deeper in the discharge conduit, which resulted in the trapping of two heterogeneous fluids. Only two CO_2 bearing fluid inclusions contained trapped solids with disproportionate phases of halite and sulfides that almost completely infilled the inclusions. Their occurrence suggests derivation of a heterogeneous brine from a cracking horizon (Ioannou, 2004) that was trapped during the mineralization event. Therefore, visible CO_2 bearing inclusions in the McD II fault may be derived from various sources including degassing of a shallow magma reservoir (Cheminee et al., 1991; Yang and Scott, 1996; de Ronde et al., 2005), phase separation of sea water-derived fluids, or potentially but less likely, CH_4 produced abiogenically from serpentinite (Sherwood Lollar et al., 1993).

It is interpreted that fluid boiling deep within the faults may have been caused by rapid depressurization of an overpressured fluid where overpressuring may have resulted from self-sealing due to quartz precipitation and rapid depressurization may have resulted from fluid overpressure and or fault movement (seismic activity). Evidence for overpressured fluids are the extensive angular wallrock breccia fragments within the faults and the temperature and salinity variability in FIAs representing Type 2 H_2O-NaCl-CO_2 inclusions indicating that the fluids were trapped under various temperature and pressure conditions representing slightly different times of entrapment (Loucks, 2000). The data shows measured salinities of Type 2, H_2O-NaCl-CO_2 bearing inclusions from 0.8-21.3 wt% NaCl equiv. with three modes of decrepitation temperatures within narrow ranges of 294.3-372.4°C, 431.2-477.4°C and T_d>600°C. If Type 2-s-$L_{(CO2)}$-V inclusions

are assumed to represent end-member compositions, estimates of trapping conditions (pressures) may be determined. Isochores calculated using microthermometric measurements modeled in the H_2O-NaCl-CO_2 and H_2O-CO_2 systems using MacFlinCor (Brown and Hagemann, 1994 and Brown and Lamb, 1989 respectively) when intersected with the average H_2O-NaCl isochors of the 6-16wt% NaCl equiv. range, resulted in P values in the 400-1200 bar range (Fig 3.20). Error in these modeled systems may be due to the complex nature of the fluids-volatiles (C2- and C3- hydrocarbons), based on GC data (see Appendix 6). The intersecting isochors results (400-1200 bars) imply a water depth of 4000 to 12000 metres for this open to seafloor fault system; a water depth that is unrealistic based on water depths of the modern seafloor arcs (Humphris and Tivey, 2000; de Ronde et al., 2003). Pressures were then calculated using the equations provided by Bakker (BULK-program) for lower pressure systems, with the equations of state for a liquid-like gas mixture & homogenization conditions of non-aqueous phases of Bakker (1999), Bowers & Helgeson (1983). The equation of state for volumetric properties was calculated using a combination of Duan et al. (1992) and Krumgalz et al. (1996). Microthermometric measurements on low X_{CO2}, presumably end-member inclusions have estimated hydrostatic trapping pressures represented by 3 modes; 9.14-9.65 MPa, 10.21-10.73 MPa and 12.26-13.87 MPa. Therefore, pressure corrections are negligible to the overall system since the pressures are minimal, and trapping temperatures will not be significantly greater than homogenization temperatures. These pressures suggest that the water depth of water within the open to seafloor McD fault system was in the range of 900 to almost 1400m, this water depth is consistent both the

modern seafloor arcs and the range of water depths assumed during eruption and

emplacement of the Mine Sequence (Gibson, 1990).
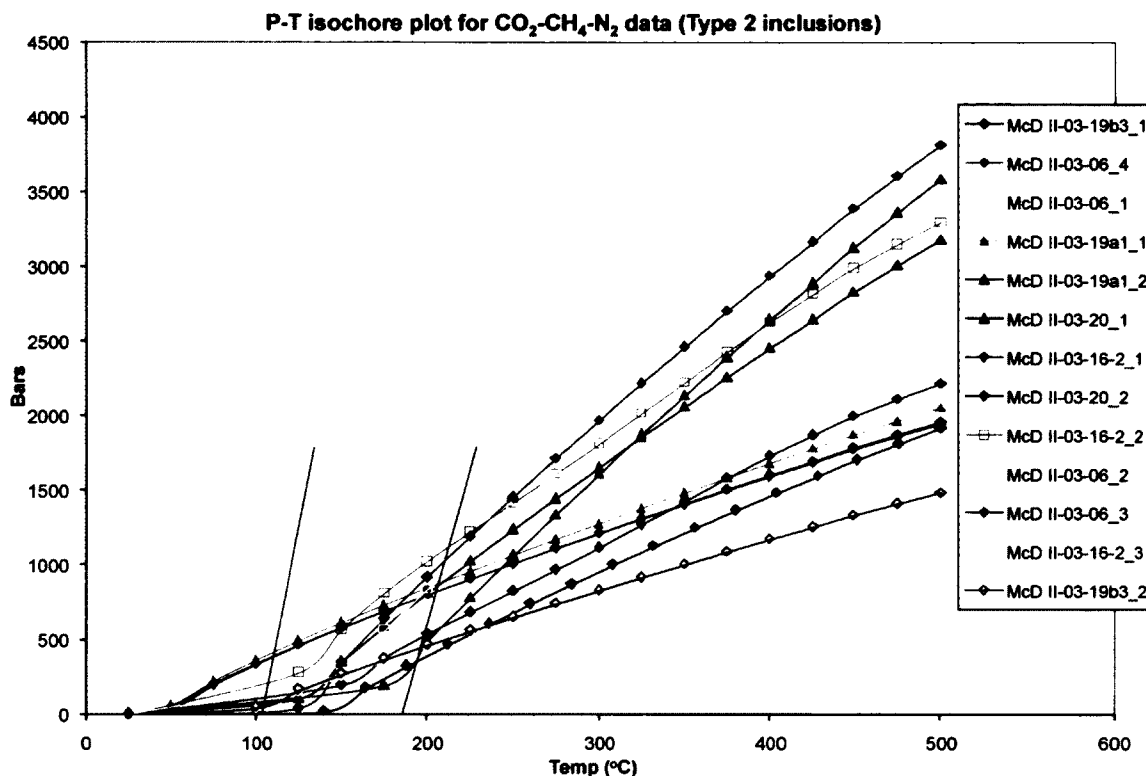
Figure 3.20: P-T plot of CO_2-CH_4-N_2 isochores with estimated minimum and maximum average isochors for Type I inclusions (line in red).

A cluster of four Type 1-p FIAs from the McD I fault have salinities that are

below those expected for seawater and are plotted on the bivariante plot of Fig 3.18 with

three Type 1-p high salinity (16-27wt% equiv.) FIAs. These two groups of FIAs are

interpreted to be a product of phase separation with an evolved seawater or magmatic

origin, with an overall low abundance as compared to the more common 6-16 wt% NaCl

equiv. FIAs. Hedenquist and Henley (1985) have shown that gases and salts dissolved in

solution contribute to the depression of the melting point of ice relative to pure water

within modern epithermal systems of the New Zealand geothermal fields. It is

interpreted that these low salinity Type 1-p FIAs within the McD I fault were likely

produced through phase separation followed by extensive fluid/volatile mixing within the fault, with volatile concentrations below ~0.85 molal as a dissolved species, since higher concentration should produce a visible CO_2 clathrate in the H_2O-CO_2 system (Barton and Chou, 1993). High salinity FIAs with coexisting <3.2wt% NaCl FIAs would require phase separation to occur at ~450°C and at 40MPa (Sourirajan and Kennedy, 1962; Bischoff, 1991), a temperature range consistent with GC-irMS equilibration temperatures of 300-400°C (Potter et al., 2007) of CO_2 and CH_4 magmatic isotopic signatures and 294-477°C decrepitation temperatures of Type 2 inclusions. In addition, self-sealing of the faults by quartz precipitation and depressurization by fault movement likely caused pore fluid pressure gradients and phase separation of already metasomatized (6-16 wt% NaCl equiv.) fluid within the faults, ultimately cooling and mixing with modified seawater fluids. It should be noted that these primary inclusions also plot with high salinity low temperature Type 1-s-py fluid inclusions that are exclusively associated with pre or post chalcopyrite, pyrite mineralization (Type V "vein") in the McD I fault. Type 1-s-py inclusions are likely not a product of phase separation and are interpreted to be highly evolved seawater fluids within the Ca-system, typically >20wt% $CaCl_2$ (Gutzmer et al., 2003) or with various other cations-chloride complexes (Na-K bearing inclusions determined from decrepitation mound analysis – Appendix 5). Type 1-s-py FIs possibly represent a separate, high salinity pre-chalcopyrite fluid, suggestive that high salinity Type 1 inclusions may have various cation-chloride complexes other than Na^+.

Decreasing temperatures with increasing salinities of T_h-T_m plotted Type 1 inclusions (Fig 3.18) is a trend suggestive of a progressive unmixing of a gas rich phase as a result of phase separation within the McD I/II and C faults. Hedenquist and Henley,

1985, plotted fluid inclusion data from high and low gas epithermal systems and showed

boiled fluids to have only a maximum of about 30% enrichments of dissolved salts with

cooling from adiabatic boiling of a 300° fluid to 200°C and well over half the dissolved

CO_2 with a small (10°C) temperature decrease. Therefore, phase separation within the

faults likely did not produce the enrichment of seawater, but of seawater modified fluids

from the various levels of the semiconformable alteration zone or of magmatically

derived fluids.

Magmatic fluids

Hypersaline fluids (>30wt% NaCl equiv.) with trapping temperatures of ~400°C

have been suggested as evidence for a magmatic contribution to the VMS system, where

the magmatic fluids are derived from breaching of a two-cell convective system (e.g. $T_t =$

373+/- 44°C and 38.2+/-19wt% NaCl equiv.; Archean Matagami Bell River complex

cracking zone - Ioannou and Spooner, 2007), and/or exsolved from a crystallizing magma

(Ioannou and Spooner, 2007; Weiershäuser and Spooner, 2005; Drieberg, 2003; Yang and

Scott, 1996). Visually discerning and microthermometrically measuring magmatically

derived fluid inclusions within any hydrothermal systems is challenging and may never

be possible in natural systems without the aid of isotopic analysis (Roedder, 1992;

Shepherd, et al. 1985). As evidenced by isotopic analysis of the McD II fault, a

magmatic isotopic signature was measured, despite none of the FIAs in the McD I/II, C

faults or Corbet deposit having salinities that are representative of hypersaline fluids.

Hypersaline fluids associated with some VMS deposits, like those mentioned above, are

likely brines that were generated during boiling, or by post-entrapment water loss by H_2

diffusion out of the inclusion. Masking of possible hypersaline fluids within the McD

I,II, C-fault and Corbet deposit may have occurred through fluid mixing in the faults, or low salinity derived fluids from the magma.

Webster, J.D., Kinzler, R.J. and Mathez, E.A. (1998) have experimentally determined that regardless of the parental melt composition a typical magma cannot exsolve hypersaline fluids because this would require an unusually high Cl^-/H_2O ratio in the melt and the exsolution of a vapor phase dominated by H_2O and/or CO_2 is much more likely. At 2000 bars and temperatures near 1100°C, silicate melt inclusions for most basalts and andesites contain <1 wt.% Cl^- implying that only Cl-bearing vapor (not vapor and hydrosaline liquid) will exsolve from the magmas and the Cl^- contents of the aqueous vapors will be <4wt.% at pressures ≥ 2000 bars (Webster, J.D., Kinzler, R.J. and Mathez, E.A., 1998). Therefore, any of the FIAs within the McD and C faults or Corbet deposit may possibly represent magmatic fluids and microthermometry is inconclusive.

The presence of Type 2 - CO_2 bearing inclusions within the McD I/II faults had a significant effect on the outcome of the microthermometry interpretation and the course of FI analysis (SEM, GC, GC-irMS). Although Type 2 inclusions were only minor (<5% visible inclusions), and <1 mole % combined of $CO_2+CH_4+C_2H_4$ for McD I and <2 mole% combined for the McD II fault (Appendix 6 – GC analysis) with a magmatic isotopic signature (Appendix 7 – GC-irMS analysis), their low abundance and source may significantly contribute to the metal budget of the hydrothermal system, over systems with similar fluid circulation and alteration (Gibson, pers. comm.).

135

CHAPTER 4
DISCUSSION AND CONCLUSIONS

Introduction

The fluid and volatile characteristics of modern black smokers as well as the conduit structure and mineral precipitation models can provide an analogue to comparable features associated with the Archean McDougall I/II and C-shaft (McD & C) faults. Fluid inclusion data and interpretation of vein textures from dredged samples of VMS mounds and from epithermal deposits can provide models for vein development and the PVTX-fluid characteristics that are applicable to ancient VMS systems. Fluid inclusions from the McD and C faults provide a unique opportunity to collect data from a dynamic upflow system where the characteristics for fluids of different temperatures, salinities and origins can be measured, avoiding direct sea water input as is typically encountered in studies of fluids trapped in near-seafloor environments such as the stringer zones to Archean VMS deposits (ie: Corbet deposit). Processes in the early oceans have been interpreted to be fundamentally the same at modern mid-ocean ridges and arcs, allowing for direct comparisons between black smokers and Archean VMS systems (Hannington et al., 1995). Processes controlling sulfide deposition (mixing, cooling and pH) are similar at seafloor hydrothermal vents everywhere (Von Damm, 1990; Hannington, 1995), where major differences in the chemistry of hydrothermal fluids are typically associated with phase separation and a breached high temperature reaction zone (HTRZ), leading to the influx of extensively modified and/or magmatic fluids. A secondary aim of this chapter is to compare the fluid/volatile characteristics of FIAs trapped within these faults to other Archean VMS systems.

Factors influencing the formation of quartz veins

Dredge sampling of modern ocean floor VMS hydrothermal vent areas has
returned samples that contain veins with euhedral quartz-breccia textures that are similar
to those described in quartz-sulfide veins of the McD and C faults. For example, Delaney
et al. (1987) described quartz-cemented breccias, dredged from the east facing wall of the
TAG central graben, with one sample consisting of hexagonal outlines of a euhedral
interlocking matrix quartz that was interpreted to have been derived from a fault and/or
stringer zone that is remarkably similar to the interlocking quartz textures observed in the
McD and C faults and the Corbet deposit in "hot-cathode" CL images (Chapter 3).
Modern shallow seafloor quartz-pyrite breccia veins have been described by Humphris
and Tivey (2000) at the TAG-1 site from 110 metres below the sea floor, and Embley et
al. (1988) and Alt (1995) described an exposed stringer zone at the Galapagos Spreading
Center where highly altered volcanic rock surrounded anastomosing veinlets of silica, Fe-
chlorite, pyrite, chalcopyrite and cristobalite; thus quartz is contemporaneous with active
faulting, hydrothermal venting and sulfide mound formation at relatively shallow depths
below the seafloor. In addition, the quartz-breccia texture of the McD and C faults is also
not unique when compared to VMS stringer-zone breccia veins such as those of the
Cambrian Hellyer deposit, Australia (Khin Zaw et al., 1995) and Archean Ansil deposit,
at Noranda, Quebec (Weiershäuser, 2005). Detailed descriptions of the quartz veins are
lacking in most of these studies, and no reference is made to interstitial mosaic or
microcrystalline quartz to comb-textured quartz, a significant textural variation of quartz
associated with chalcopyrite mineralization and changing PVTX conditions (Fournier,
1985) that may be unique to the paleo-depth of samples collected from the quartz sulfide

veins of the McD and C faults (~1000 - 500 metres below the paleo sea floor). An important result of the "hot-cathode" CL study (Chapter 3) is that quartz within the synvolcanic McD and C faults is dominantly hydrothermal, preserving primary textures in both comb and microcrystalline quartz (Chapter 2), consistent with the findings of Ioannou et al. (2004). Thus, the textural variations of hydrothermal quartz within the McD and C faults suggest varying PVTX conditions and that inclusions of primary origin may be preserved.

The McD and C faults are breccia vein structures (Chapter 2) that consist of comb textured quartz that rims the fault margins and wallrock breccia fragments, which are later infilled by microcrystalline and mosaic textured (locally amorphous) quartz of hydrothermal origin that is associated with chalcopyrite mineralization (Chapter 3- "hot-cathode" CL images) that is locally fragmented in the McD I fault. The textural variation suggests that the faceted comb textured quartz precipitated from silica oversaturated fluids with relatively stable PVTX conditions over a longer period of time as described in epithermal (Dong et al, 1995) and gold deposits (Dowling et al., 1989) due to open space during crystal growth, high permeability (experimentally determined by Takeno et al., 2000) and relatively slow changing conditions. During comb textured quartz growth, the surrounding wall rocks were likely approaching a steady state with the open conduit. Fluids precipitating comb textured quartz were likely derived from acidic (pH <3) hydrothermal solutions in the $200°$ to $340°C$ range (Fournier, 1985), which are consistent with the extensive chlorite alteration halo surrounding the faults (Chapter 2). The fluids are interpreted to be derived from semiconformable alteration zones (Chapter 3) and intermittent HTRZ fluids. In the McD and C faults a steady-state system likely persisted

138

that was characterized by ascending fluids of moderate temperature (130-170°C) and salinity (6-16wt% NaCl), until permeability was decreased by the precipitation of comb-textured quartz within the main upflow zones in the faults (Chapter 2 - o/c photos & mapping).

Prior to sealing, fluids likely continued to precipitate quartz under stable hydrostatic conditions, and are now represented by the bulk of microthermometric measurements that range in minimum temperatures from 130-170°C and with salinities of 6-16 wt% NaCl equiv, since at temperatures below about 300°C, pressure and salinity have very little effect on the solubility of quartz (Fournier, 1985). The decrease in permeability as a result of self-sealing would have resulted in decreased flow rates and decreased mixing between deeper derived higher temperature fluids in the 300°C range and more shallowly derived lower temperature fluids, allowing the deeper derived fluids to rise to higher levels within the faults and maintain their temperature. At temperatures above 300°C metals, in particular Cu can be solubilized as a chloride complex, and at this temperature the effect of both pressure and salinity changes can significantly affect the solubility of quartz (Fig 3.2 in Fournier, 1985 - shaded area of retrograde solubility). Microthermometic measurements and GC-irMS analyses suggest that fluid temperatures were >300°C, as Type 2 -CO_2 bearing inclusions have decrepitation temperatures >300°C (one inclusion w/ a T_h of ~331°C) and the $\Delta_{CH4-CO2}$ values suggest equilibration temperatures of 300-400°C for the MDII and 250-350°C for the MDI, thus moving the fluids into the "quartz retrograde solubility" field, where silica undersaturated fluids are capable of dissolving quartz (silica) until the solution either boils or the solubility maximum is reached (Fournier, 1985). Corrosion on the margins and interstitially

139

between comb textured quartz, as evident in "hot-cathode" CL images, is interpreted to be a result of fluids undersaturated with respect to silica due to increasingly higher temperatures ($>300°C$). As fluids become saturated in silica significant changes in temperature or composition may result in rapid precipitation of mosaic and microcrystalline quartz, which along with chalcopyrite infill voids within breccia veins.

The co-precipitation of microcrystalline (chalcedony) and amorphous mosaic-textured quartz with chalcopyrite within the center of Type 1 and 2 qtz-breccia veins suggests a high degree of silica supersaturation, with respect to quartz, and rapid changes in the chemical and physical conditions of the fluid to lower temperatures and likely neutral to alkaline conditions (Fournier, 1985). These conditions and the resulting quartz textures can be accounted for by silica supersaturation resulting from decompressional boiling over a short column height (Cline et al, 1992), a process supported by the occurrence of Type 1-s-cpy and possibly co-genetic Type 2 - CO_2-complex hydrocarbon inclusions. In addition, trace amounts of CO_2 within low salinity (ie: salinity $<3.2wt\%$ NaCl) Type 1 inclusions likely represents phase separated vapour from a deeper boiling fluid (Chapter 3). The extent of silica supersaturation during boiling may precipitate a variety of silica polymorphs, but deposition of amorphous silica requires a high degree of silica saturation (Cline et al., 1992). Boiling becomes less effective in precipitating quartz below $340°C$ (Fig 5 – Cline et al., 1992) (diff of ~700ppm vs. ~470 ppm below $340°C$), due to the difference in quartz solubility between the liquid and vapour phase as temperatures decrease, shifting conditions to where growth-zoned quartz precipitates at slower rates (ie: Fournier 1985 - Fig 3.2). Precipitation of amorphous quartz from acidic fluids also results in a shift to near neutral to alkaline conditions as CO_2 is separated from

solution and the salinity is increased (Weres et al., 1982, Fournier, 1985). Thus, boiling

is an effective depositional mechanism for amorphous and microcrystalline quartz, but

also for metals, particularly for chalcopyrite whose solubility is very temperature

dependant (Crerar and Barnes, 1976; Seyfried et al., 1999).

Metal Solubility

The McD and C faults noticeably lack a significant variety of sulfide

mineralization. The dominant sulfide is chalcopyrite within all of the faults (chapter 2 -

petrography), with only minor pyrite, sphalerite with trace electrum within a Type V vein

within the McDougall I fault and minor sphalerite with chalcopyrite disease within the C-

shaft fault. Temperature is the key variable controlling Cu solubility as a chloride

complex in hydrothermal fluids (>300°C) and the precipitation of chalcopyrite is a

function of decreasing temperature and, to a lesser extent an increase in pH (Lydon,

1988). Although single (non-FIA, Fig 3.11) inclusions record temperatures up to 375°C,

and CO_2 decrepitation temperatures range from 294-477°C, the bulk of T_h measurements

for Type 1-s-cpy inclusions lie outside of the range of significant Cu solubility

temperatures (T_h <250°C), which questions the ability of Type 1-s-cpy fluids to transport

Cu below 250°C, despite having high salinities in the 6-16wt% NaCl equiv range, which

could efficiently transported Cl⁻ complexed elements (Crerar and Barnes, 1976).

Indications that this fluid was saturated in Cu (or some Cu-sulfide) at high temperatures

(>300°C) is evident by Type 2 – multisolid inclusions in which an accidentally trapped

chalcopyrite solid phase and CO_2 indicate that the fluid precipitated its Cu by the time of

fluid entrapment. However, as Type 1-s-cpy inclusions are associated with copper

mineralization, the minimum trapping temperatures and salinities recorded more likely

represent temperatures and salinities of a fluid that has been modified (cooled) through boiling or mixing such that chalcopyrite was no longer soluble and was precipitated.

Zn is soluble as a chloride complex at temperatures >170°C and the solubility of Zn is more sensitive to pH changes than to temperature changes (Xiao et al., 1998). Despite mean FIA minimum trapping temperatures (T_h) of 166°C, 182°C and 199°C for the McDougall I, McDougall II, and C-shaft faults respectively, the faults contain only minor sphalerite, which suggests that the pH and/or temperature changes brought about through mixing, cooling or boiling were not sufficient to precipitate Zn at the paleo-level within the faults represented by the present day surface exposures.

Phase separation

The large variation in salinity of modern VMS seafloor vents is thought to reflect phase separation in hydrothermal systems (e.g., Galapagos Spreading Center, the East Pacific Rise and the Southern Juan de Fuca Ridge; Edmond et al., 1979; Von Damm, 1987). Boiling of fluids controls partitioning of dissolved gases into the vapour phase affecting pH and redox conditions. The immediate impact is to oxidize fluids and raise pH by the removal of CO_2, H_2S and H_2. This will induce sulfide precipitation and could lead to abundant sub-seafloor stockwork mineralization over a large vertical depth range coincident with the boiling zone.

Hydrothermal fluids collected from the ASHES vent field in 1986, 1987 and 1988 consist of 300°C gas enriched/low-chlorinity fluids (33% of seawater chlorinity) which transitioned to a 328°C high-chlorinity/gas depleted fluid explained as a single hydrothermal fluid undergoing phase separation (Butterfield et al., 1990), where low-chlorinity fluids (below seawater) are likely not modified on ascent to the seafloor. Low

salinity fluids that are below Archean seawater salinities within FIAs of the McD I fault

(Chapter 3) may reflect phase separation from fluid dehydration reactions resulting in

predominantly 6-16 wt% NaCl equiv. residual fluids. Once ascending fluids intersect the

boiling curve, boiling and phase separation will continue during ascent unless the

confining pressure is increased through self-sealing processes (quartz precipitation) and

subsequent crack-seal processes may result in fluctuations between boiling and non-

boiling conditions (Delaney et al., 1987). CO_2 bearing inclusions from the McD II fault

also suggest phase separation. The relatively close homogenization to decrepitation

temperature measured from Type 2 CO_2 bearing inclusions, are consistent with other

decrepitation temperatures in this system and are interpreted to reflect phase separation

along a boiling curve closest modelled by the H_2O-0.5m NaCl -0.5m CO_2 critical curve

(Wilkinson, 2001). The initial fluid or fluids may have had elevated temperatures of

>300°C and likely intersected the boiling curve during two separate events from ~324-

331°C and again at 334-372°C corresponding to calculated depth constraints of ~110 and

~134 bars. Minor scattered inclusions with salinities above 16wt% NaCl equiv. on the

wt% NaCl equiv./T_h plots and higher temperature fluids (200-250°C) in the McD and C

faults likely represent the remnants of phase separation prior to re-homogenization (6-

16wt% NaCl equiv. fluids) or higher salinity inclusions derived from deeper in the

hydrothermal system. Phase separation from the subcritical portion of the H_2O-NaCl

system is unlikely to shift a seawater derived fluid to salinities of >2-4 times since

temperatures in the sub-critical field, under optimal adiabatic conditions, are insufficient

to separate more than 30-40% vapour and can only result in a residual liquid salinity of

approximately 2 times that of seawater (Delaney et al., 1987). Therefore, minor salinity

variations resulting from boiling of 6-16wt% NaCl equiv. fluids are likely masked during chalcopyrite precipitation and dehydration reactions, as phase separation only becomes noticeable beyond the 6-16wt% NaCl equiv. salinity range and where vapors are trapped. Any low density, CO_2 bearing and low salinity phase separated fluids likely re-homogenized in the turbulent upflow zone of the breccia filled conduit. Unless the two phases are physically removed and isolated, the effects of phase separation in moving hydrothermal fluids may not be detectable (Delaney et al., 1987).

Magmatic Fluids/Volatiles

High salinity fluids (>20 wt% NaCl) and high temperature fluids (>350°C) relative to modern seawater have typically been associated with a direct input of magmatic fluids that exsolved from a magma chamber in ancient VMS-related systems (Delaney et al., 1982). For example, on the northern Cleft segment of the Juan de Fuca Ridge, vents were discharging mainly low salinity phase separated fluids in 1988, but in 1990 and 1991 the same vents were discharging high temperature chloride- and metal-rich fluids (Butterfield and Massoth, 1994). It was suggested that a megaplume event in 1986 caused the venting of a vapour-rich, metal depleted phase, followed by a later, metal rich brine. Magmatic volatiles have been the source of elevated N_2 and CO_2 in ancient and modern epithermal systems, but within ancient VMS systems, vapour rich inclusions typically are not identified (Ioannou, 2004). Type 2-CO_2+/- complex bearing hydrocarbons inclusions from the McD faults suggest a magmatic input, and GC-irMS analysis isotopically confirms a magmatic contribution, previously not quantified in other ancient VMS systems.

Many authors have suggested a magmatic contribution to account for the high salinities of inclusions encountered within ancient VMS systems. At the Matagami and Kidd Creek deposits a ~15-20% magmatic fluid input was estimated (Costa et al., 1983; Huston and Taylor, 1999; Schandl and Bleeker, 1999), and at the Millenbach deposit, Noranda (Kheang, 1982) FI containing ~40 wt% NaCl equiv. fluids were suggested to be magmatic in origin. Ioannou (2004) suggested that Archean seawater-derived hydrothermal fluids obscure magmatic signatures but suggested that phase separated brines from high salinity fluid inclusions in the Bell River Complex hydrothermal cracking horizon at Matagami are both the product of seawater and magmatic fluids. In the Panorama VMS district of Western Australia, Drieberg (2003), suggested that high salinity fluids and CO_2 bearing inclusions represented a magmatic contribution.

Phase separation of volatiles fractionates N_2 followed by CH_4 and CO_2 (Giggenbach, 1980; Butterfield et al., 1994) such that gas fractionation will favour higher volatile concentrations that are least soluble in the fluid (Hedenquist et al., 1992). Gas chromatography (Chapter 3) not only confirmed the presence of volatiles in quartz and sulfides in the McD faults, but also confirmed the presence of more complex hydrocarbons derived likely through Fischer-Tropsch synthesis (e.g., Hedenquist et al., 1992). If these inclusions represent phase separation, the gas ratio should show a linear correlation (Henley et al., 1985) similar to volatiles in inclusions from Eskay Creek (Sherlock et al., 1999). Although near-linear trends are recognized in Figure 3.18 – Chapter 3, the system likely partially re-homogenized with trapped fluids shortly after the system re-opened following boiling. It is interesting to note that in back-arc settings (Scott, 1997), addition of magmatic contributions to the arc-back-arc VMS deposits are

more obvious than at mid-ocean ridges (Kelley and Delaney, 1987; Scott, 1997). The gas

chromatography data from the McD and C faults, when plotted with data from Brothers,

Rumble II, Minami Ensai sulfides, Nurukawa quartz (de Ronde et al., 2005), TAG

samples, and the Vai Lilli and Axial Sea Mount smoker samples (Graupner et al., 2001)

show similar trends with respect to CO_2, CH_4 and N_2 (Fig 4.1 to 4.4). This is consistent

with a magmatic contribution and an arc- back-arc setting that has been inferred for the

Noranda District. In addition, the CH_4 values are an order of magnitude higher than

modern discharging fluids used in the above comparison, and may suggest an initial

rising buoyant plume from a breached cracking front. CO_2 and the highest recorded CH_4

plume samples were collected from the Monowai volcano along the Kermadec Arc in

2004 (de Ronde, pers. comm.) 2-3 weeks after eruption, and the high CH_4 samples from

the Noranda McD fault samples may record a similar "megaplume" event that expelled

magmatically derived fluids. Although the data are compatible with data drawn from arc

environments which have a high magmatic component (de Ronde et al., 2005), a

magmatic contribution can only be proven by isotopic signatures.

Magma types associated with hydrothermal systems can be distinguished using

various gas signatures and within modern systems, systematic analysis of N_2, Ar, He, and

CO_2 make the source of gases more apparent (de Ronde, 1995). As described above, the

CO_2 and N_2 ratios from the McD and C shaft faults compare favourably to modern arc

vent systems. Methane encountered at 21°N along the mid-ocean ridge system is

interpreted to have been derived through inorganic reactions (Welhan, 1988; de Ronde,

1995) and the $\delta 13C_{CH4}$ and $\delta 13C_{CO2}$ isotopic signatures were used to identify fluid

sources. The average McD II fault isotopic signatures range from -18.9 to -26.8‰ for
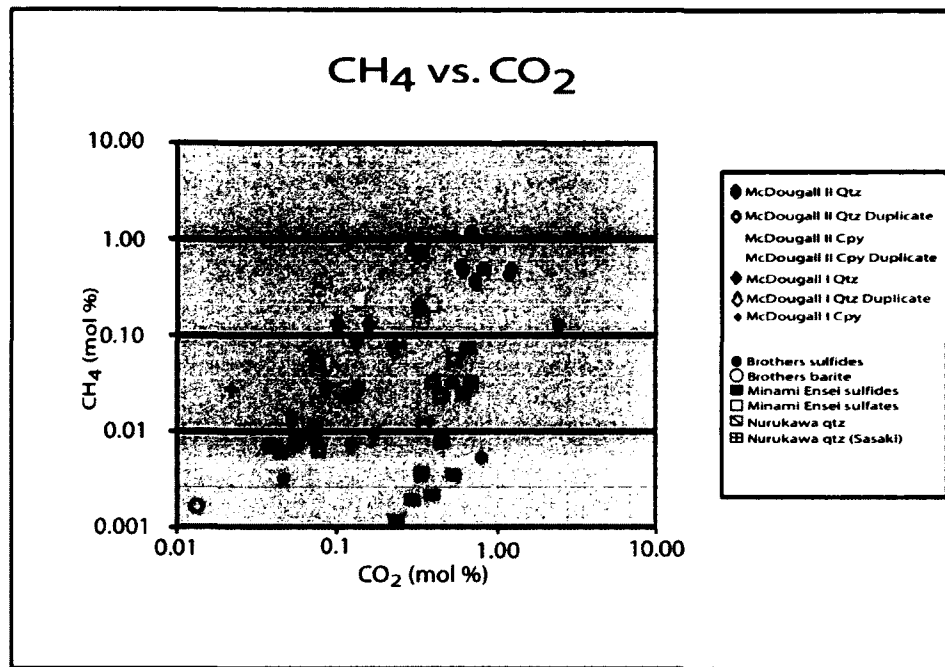
Figure 4.1: CH₄ vs. CO₂, GC data (Chapter 3) plotted with data of de Ronde, et al., 2005, Fig 14 – gas contents from fluid inclusions in sulfide and sulfate minerals from Brothers northwest and southwest caldera sites, Kermadec Arc, the Minami Ensei vent site, Okinawa back arc, and the Nurukawa Kuroko deposit, northern Nonshu, Japan.
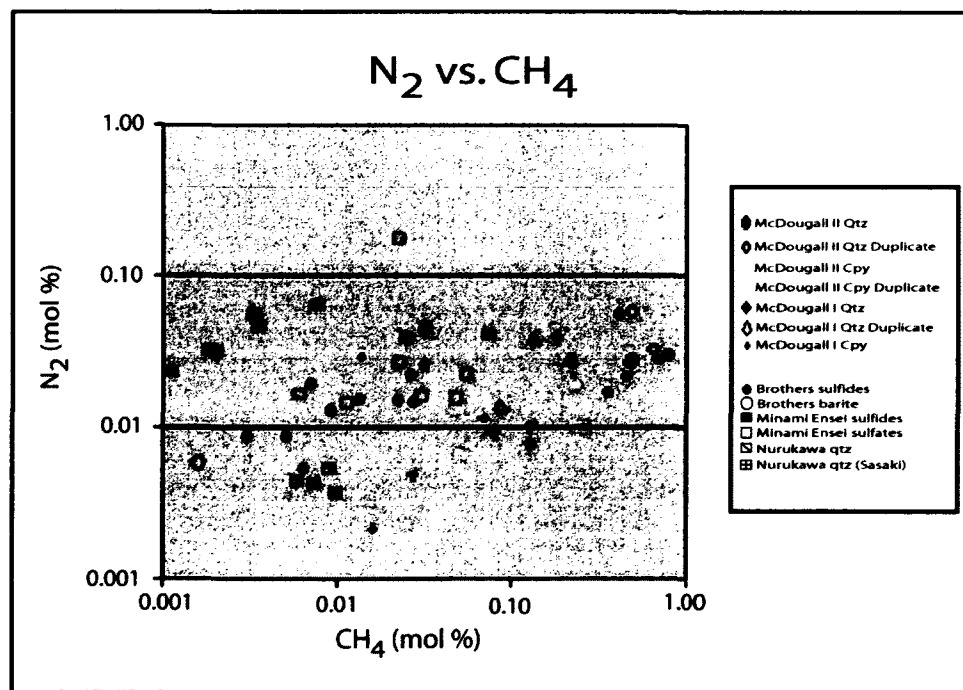
Figure 4.2: N₂ vs. CH₄, GC data (Chapter 3) plotted with data of de Ronde, et al., 2005, Fig 14 – gas contents from fluid inclusions in sulfide and sulfate minerals from Brothers northwest and southwest caldera sites, Kermadec Arc, the Minami Ensei vent site, Okinawa back arc, and the Nurukawa Kuroko deposit, northern Nonshu, Japan.

147
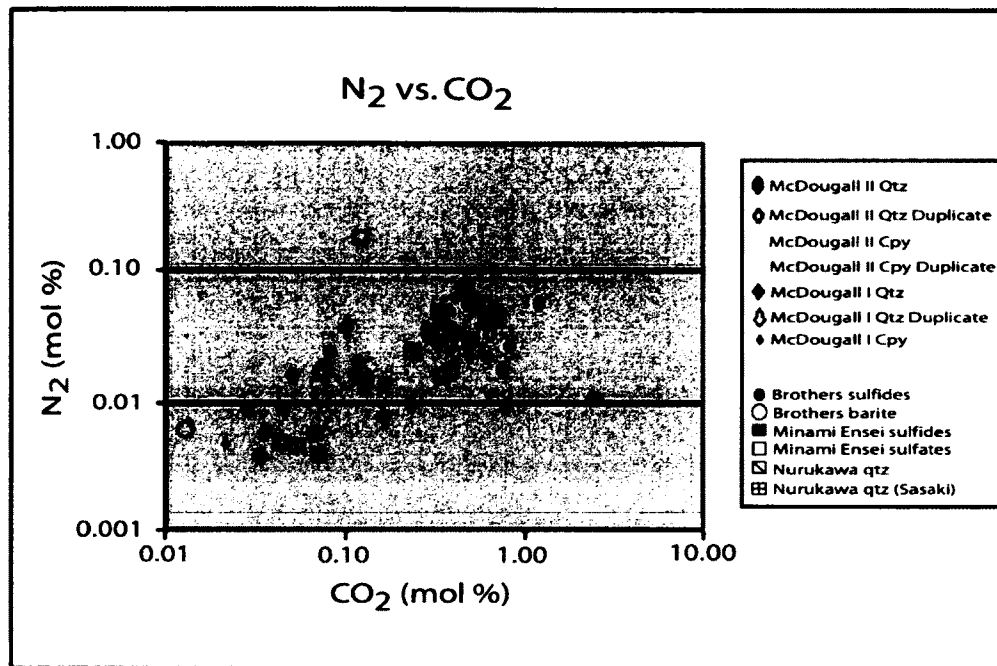
Figure 4.3: N₂ vs. CO₂, GC data (Chapter 3) plotted with data of de Ronde, et al., 2005, Fig 14 – gas contents from fluid inclusions in sulfide and sulfate minerals from Brothers northwest and southwest caldera sites, Kermadec Arc, the Minami Ensei vent site, Okinawa back arc, and the Nurukawa Kuroko deposit, northern Nonshu, Japan.
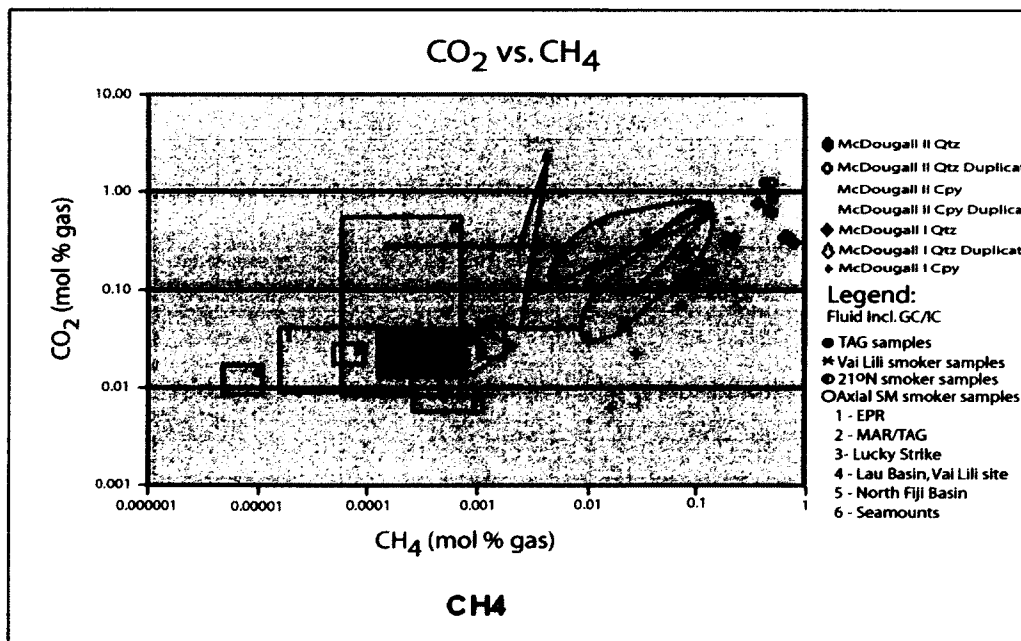
Figure 4.4: CO₂ vs. CH₄ data (Chapter 3) plotted with data compiled by Graupner et al. (2001) of calculated end-member data for discharging vent fluids.

148

$\delta13C_{CH4}$ and -5.3 to +1.3 for $\delta13C_{CO2}$, and are comparable to modern hydrothermal vent systems such as those of South Cleft, Juan de Fuca Ridge, Okinawa Trough (Minami-Ensei) 13°N EPR, North Fiji Basin (White Lady & Kaiyo) and Broadlands. The isotopic signatures within the McD II fault are similar to modern vent fluids within back-arc basins and back-arc spreading centers that are indicative of a magmatic source (de Ronde, 1995) but 0‰ signatures suggest also a seawater derived component (Potter et al., 2007). The $\delta13C_{CH4}$ and $\delta13C_{CO2}$ isotopic signatures from the McD I fault suggest a depleted source (Potter et. al. 2007) and the combined $\delta13C_{CH4}$ and $\delta13C_{CO2}$ signatures don't compare to any modern seafloor hydrothermal fluids. The Noranda District does not contain graphitic sediments within its strata (Gibson, pers. comm.) and thus the source of fluids derived from a depleted source are at present unresolved. In summary, modern vent fluids and the McD II fault data are consistent with a magmatic contribution and overprinting seawater has not completely masked this signature. The magmatic volatile contribution is thought to be important for ore formation because of the high metal contents of magmatic fluids (e.g. Sawkins and Kowalik, 1981; Yang and Scott, 1996).

Conclusions

The main conclusions of this research are:

1. The McDougall I, II and C-shaft faults are mineralized, VMS hydrothermal upflow zones that were localized along synvolcanic faults within the Archean, Noranda Volcanic Complex.

2. Within the McD I, II and C-Shaft faults the anastomosing quartz-sulfide veins have similar textures within all the faults. The veins contain 20-70% angular, wall rock fragments (variably altered andesite) that are cemented by comb-

textured quartz that has a central zone or interior of mosaic-textured to microcrystalline quartz and chalcopyrite mineralization. Locally, the comb-textured quartz is fragmented and re-cemented by mosaic-textured to microcrystalline quartz and chalcopyrite, and this brecciation in interpreted to be a product of hydrostatic fracturing, and /or movement along the fault. The microcrystalline quartz texturally appears contemporaneous with chalcopyrite precipitation and chlorite alteration within the veins, suggestive of silica saturation resulting from decompressional boiling. The lack of sphalerite within the faults suggests that pH and/or temperature changes resulting from mixing, boiling or cooling were insufficient to precipitate Zn at this level (depth) within the hydrothermal conduits.

3. "Hot-cathode" CL observations suggest that the McD I, II and C-shaft faults have preserved Archean hydrothermal quartz that has retained original depositional textures (comb-textured quartz with concentric growth zoning) and shows an almost complete lack of recrystallization or strain. This indicates that the quartz has a high potential for preserving primary FI. Carbonates are abundant along quartz margins where they are associated with the chalcopyrite mineralization.

4. Microthermometric and salt decrepitation mound analysis indicate that the fluids are representative of a H_2O-NaCl system with lesser K^+ and divalent cations such as Ca^{2+} and Mg^{2+}.

5. Primary FIAs trapped during comb-textured quartz growth or in mosaic textured quartz overlap secondary inclusions, indicating that similar evolved seawater

fluids were present prior and during mineralization as mosaic textured quartz likely formed from silica supersaturated fluids.

6. Visible CO_2 inclusions suggest phase separation at depth during late stage chalcopyrite mineralization, and trapped solids (sulfide/halite) suggest heterogeneous entrapment of fluids supersaturated in Cu with high salinities. The calculated pressure of CO_2 bearing inclusions suggests hydrostatic trapping at 9.2-9.7MPa, 10.2-10.7MPa and 12.3-13.9MPa, which is consistent with a 900 to 1400m water depth including the depth of water within the open to seafloor fault system. Trends of FI data derived from epithermal systems suggest that fluids within the McD I, II and C-shaft faults are similar, and may be products of fluid dehydration reactions in the semi-conformable or discordant alterations zones and later mixing within the discharge conduit, and/or phase separation during ascent. The similarity between FIA trends in the McD I, II and C faults and the Corbet deposit suggest similar fluids whose range in composition (salinity) and temperature are consistent with seawater to evolved seawater that has been modified via fluid-rock interaction within semiconformable alteration zones.

7. Trace amounts of Sn from geochemical analysis of fault samples suggests a possible magmatic contribution.

8. Gas chromatography confirmed that hydrocarbons are present in quartz and chalcopyrite from the McDougall faults; their order of abundance is $H_2O \gg CO_2 \geq CH_4 > N_2 \geq COS > C2's- > C3's$. The presence of hydrocarbons supports measured CO_2 melting temperatures as low as -60.9°C. Volatile concentrations were also an order of magnitude greater in FI within quartz compared to those in

chalcopyrite. Hydrocarbon trends are consistent with those documented from discharging hydrothermal fluids in modern arc and back-arc environments.

9. Isotopic analysis of FI in the McDougall faults are consistent with magmatic and seawater-derived sources for the CO_2-bearing fluids trapped in quartz within the McDougall II fault and a depleted source for CO_2-bearing fluids trapped within quartz in the McDougall I fault. Calculated equilibration temperatures are consistent with CO_2 microthermometry and are in the 300-400°C range. The isotopic results suggest that magmatic fluids were, at least episodically, incorporated into a dominantly evolved seawater, Archean, hydrothermal system at Noranda.

REFERENCES

Alt, J.C., 1995, Sub-seafloor processes in mid-ocean ridge hydrothermal systems, in Humphris, S.E., Zierenberg, R.A., Mullineaux, L.S., and Thomson, R.E., eds., Seafloor hydrothermal systems: physical, chemical, biological, and geological interactions. American Geophysical Union Monograph 91, p. 222-272.

Ayer, J., Amelin, Y., Corfu, F., Kamo, S., Ketchum, J., Kwok, H., and Trowell, N., 2002, Evolution of the southern Abitibi greenstone belt based on U-Pb geochronology: autochthonous volcanic construction followed by plutonism, regional deformation and sedimentation: Precambrian Research, v. 115, p. 63–95.

Bakker, R.J., Brown, P.E., and Hagemann, S.G., 1999, Adaptation of the Bowers and Helgeson (1983) equation of state to the H_2O-CO_2-CH_4-N_2-NaCl system: Chemical Geology, v. 154, p. 225-236.

Barton, P.B., and Chou, I,M., 1993, Calculation of the vapor-saturated liquidus for the NaCl-CO_2-H_2O system: Geochimica et Cosmochimica Acta, v. 57, p. 2715-2723.

Baker, J.R., 2003. FLUIDS, package of computer programs for fluid inclusion studies Program 1: BULK, version 01/03.

Bischoff, J.L., 1991, Densities of liquids and vapors in boiling NaCl-H2O solutions: A PVTX summary from 300° to 500°C: American Journal of Science, v. 291, p. 309–338.

Bischoff, J.L., and Rosenbauer, R.J., 1988, Liquid-vapor relations in the critical region of the system NaCl-H_2O from 380 to 415°C: A refined determination of the critical point and two-phase boundary of seawater: Geochimica et Cosmochimica Acta, v. 52, p. 2121-2126.

Bodnar, R.J., 1994, Philosophy of fluid inclusion analysis. *In* Fluid Inclusions in Minerals, Methods and Applications (B. De Vivo & M. L. Fressotti, eds.) Virginia Tech, Blacksburg, VA, p. 1-6.

Bodnar, R.J., Reynolds, T.J., and Kuehn, C.A., 1985, Fluid-inclusion systematics in epithermal systems, in Berger, B.R., and Bethke, P.M., eds., Geology and Geochemistry of Epithermal Systems, Volume 2. Reviews in Economic Geology, Society of Economic Geologists, p. 73-97.

Bodnar, R.J., 1993, Revised equation and table for determining the freezing point depression of H_2O-NaCl solutions: Geochimica et Cosmochimica Acta, v. 57, p. 683-684.

Bodnar, R.J., and Vityk, M.O., 1994, Interpretation of microthermometric data for H_2O-NaCl fluid inclusions, *in* Vivo, B.D., and Frezzotti, M.L., eds., Fluid inclusions in minerals: Methods and applications: International Mineralogical Association Short

Course Manual, p. 117–130.

Bodnar, R.J., 2003, Introduction to fluid inclusions:, Fluid inclusions; analysis and interpretation, Short Course Series v. 32, p.1-8.

Bowers, T.S., and Helgeson, H.C., 1983, Calculation of the thermodynamic and geochemical consequences of nonideal mixing in the system H_2O-CO_2-NaCl on phase relations in geologic systems: Equation of state for H_2O-CO_2-NaCl fluids at high pressures and temperatures: Geochimica et Cosmochimica Acta, v. 47, p. 1247-1275.

Bray, C.J., Spooner, E.T.C., 1992, Fluid inclusion volatile analysis by gas chromatography with photoionization/micro-thermal conductivity detectors; applications to magmatic MoS_2 and other H_2O-CO_2 and H_2O-CH_4 fluids: Geochimica et Cosmochimica Acta, Current research on fluid inclusions; PACROFI III; papers presented at the Third biennial pan-American conference on Fluid inclusions, v. 56, p.261-272.

Brown, P.E., and Hagemann, S.G., 1994, MacFlinCor: A computer program for fluid inclusion data reduction and manipulation. In De Vivo and Frezzotti (eds) Fluid Inclusions in Minerals: Methods and Applications, VPI Press, p. 231-250.

Brown P.E., and Lamb, W.M., 1989, P-V-T properties of fluids in the system H_2O + or - CO_2 + or - NaCl; new graphical presentations and implications for fluid inclusion studies: *Geochimica et Cosmochimica Acta*, v. 53, p. 1209-1221.

Burruss, R.C., 1984, Analysis of phase equilibria in C-O-H-S fluid inclusions, in Hollister, L.S. and Crawford, M.L., eds., Fluid inclusions, applications to petrology; Geological Association of Canada Short Course Handbook, v. 6, p. 39-74.

Butterfield, D.A., Massoth, G.J., McDuff, R.E., Lupton, J.E., and Lilley, M.D., 1990, Geochemistry of hydrothermal fluids from Axial Seamount Hydrothermal Emissions Study vent field, Juan de Fuca Ridge: Subseafloor boiling and subsequent fluid-rock interaction: Journal of Geophysical Research, v. 95, p. 12895-12921.

Butterfield, D.A., and Massoth, G.J., 1994, Geochemistry of north Cleft segment vent fluids: Temporal changes in chlorinity and their possible relations to recent volcanism: Journal of Geophysical Research, v. 99, p. 4951–4968.

Candela, P. A., 1997, A review of shallow, ore-releateed granites: Textures, volatiles, and ore metals: Journal of Petrology, v. 38, p. 1619-1633.

Card, K.D., 1990, A review of the Superior Province of the Canadian Shield, a product of Archean accretion: Precambrian Research, v. 48, p. 99-156.

Cathles, L.M., 1993, Oxygen Isotope Alteration in the Noranda Mining District, Abitibi

Greenstone Belt, Quebec: Economic Geology, v. 88, p. 1483-1511.

Channer, D.M., and Spooner, E.T.C., 1994, Combined gas and ion chromatographic and analysis of fluid inclusions; applications to Archean granite pegmatite and pegmatite and gold-quartz vein fluids: Geochimica et Cosmochimica Acta, v. 58, p. 1101-1118.

Chen, C.H., 1970, Geology and geothermal power potential of the Tatun volcanic region: Geothermics, Special Issue 2, Proceedings of the United Nations symposium on The development and utilization of geothermal resources, v. 2, p.1134-1143.

Chen, C.H., 1975, A method of estimation of standard free energies of formation of silicate minerals at 298.15 degrees K: American Journal of Science, v. 275, p. 801-817.

Cheminee, J.L., Stoffers, P., McMurty, G., Richnow, H., Puteanus, D., and Sedwick, P., 1991, Gas-rich submarine exhalations during the 1989 eruption of Macdonald Seamount: Earth and Planetary Science Letters, v. 107, p. 318-327.

Cline, J.S., Bodnar, R.J., and Rimstidt, J.D., 1992, Numerical simulation of fluid flow and silica transport and deposition in boiling hydrothermal solutions; application to epithermal gold deposits: Journal of Geophysical Research, v. 97, p. 9085-9103.

Cline, J.S., and Bodnar, R.J., 1994, Direct evolution of brine from a crystallizing silicic melt at the Questa, New Mexico, molybdenum deposit: Economic Geology, v. 89, p. 1780-1802.

Collins, P.L.F., 1979, Gas hydrates in CO_2-bearing fluid inclusions and the use of freezing data for estimation of salinity: Economic Geology, v. 74, p. 1435-1444.

Costa, U.R., Barnett, R.L., and Kerrich, R., 1983, The Mattagami Lake mine Archean Zn-Cu sulfide deposit, Quebec: Hydrothermal coprecipitation of talc and sulfides in a sea-floor brine pool--Evidence from geochemistry, $^{18}O/^{16}O$, and mineral chemistry: Economic Geology, v. 78, p. 1144-1203.

Crerar, D.A., and Barnes, H.L., 1976, Ore solution chemistry V. Solubilities of chalcopyrite and chalcocite assemblages in hydrothermal solution at 200° to 350°C: Economic Geology, v. 71, p. 772-794.

de Ronde, C.E.J., 1995, Fluid chemistry and isotopic characteristics of seafloor hydrothermal systems and associated VMS deposits: Potential for magmatic contributions, in Thompson, J. F. H., ed., Magmas, Fluids, and Ore Deposits, Mineralogical Association of Canada, Short Course Volume 23, p. 479-509.

de Ronde, C.E.J., Channer, D.M., Faure, K., Bray, C.J., and Spooner, E.T.C., 1997, Fluid chemistry of Archean seafloor hydrothermal vents: Implications for the composition of circa 3.2Ga seawater: Geochimica et Cosmochimica Acta, v. 61, p. 4025-4042.

de Ronde, C.E.J, Hannington, M.D., Stoffers, P., Wright, I.C., Ditchburn, R.G., Reyes,

155

A.G., Baker, E.T., Massoth, G.J., Lupton, J.E., Walker, S.L., Greene, R.R., Soong, C.W.R., Ishibashi, J., Lebon, G.T., Bray, C.J., and Resing, J.A., 2005, Evolution of a submarine magmatic-hydrothermal system; Brothers Volcano, southern Kermadec Arc, New Zealand: Economic Geology and the Bulletin of the Society of Economic Geologists, v. 100, p. 1097-1133.

de Rosen-Spence, A.F., 1976, Stratigraphy, development and petrogenesis of the central Noranda volcanic pile, Noranda, Quebec: Ph.D. thesis, University of Toronto, Toronto, Ontario, 166 p.

de Vries, S.T., and Touret, J.L.R., 2007, Early Archaean hydrothermal fluids; a study of inclusions from the ~ 3.4 Ga Buck Ridge Chert, Barberton Greenstone Belt, South Africa: Chemical Geology, v 237, p 289-302.

Deer, W.A., Howie, R.A., and Zussman, J., 1998, An Introduction to rock-forming minerals: Longman Group Ltd., London, United Kingdom, 528p.

Delaney, J.R., 1982, Generation of high salinity fluids from seawater by two phase separation: EOS Transactions, Transactions of the American Geophysical Union, v. 63, p. 1135.

Delaney. J.R., Mogk, D.W., and Mottl, M.J., 1987, Quartz-cemented breccias from the Mid-Atlantic Ridge: Samples of a high-salinity hydrothermal upflow zone: Journal of Geophysical Research, v. 92, p. 9175–9192.

Diamond L.W., 2003, Systematics of H$_2$O inclusions: In Samson I., Anderson A. and Marshall D. (Eds.) Fluid Inclusions: Analysis and Interpretation., Mineralogical Association of Canada., v. 32 p. 55-79.

Dimroth, E., and Lichtblau, A.P., 1979, Metamorphic evolution of Archean hyaloclastites, Noranda area, Quebec, Canada; Part I, Comparison of Archean and Cenozoic sea-floor metamorphism: Canadian Journal of Earth Sciences, v.16, p. 1315-1340.

Dimroth, E., Imreh, L., Rocheleau, M., and Goulet, N., 1982, Evolution of the south-central part of the Archean Abitibi Belt, Quebec. Part I: Stratigraphy and paleogeographic model: Canadian Journal of Earth Sciences, v. 19, p. 1729–1758.

Dimroth, E., 1983, Evolution of the south-central segment of the Archean Abitibi belt, Quebec. Part III: Plutonic and metamorphic evolution and geotectonic model: *Canadian Journal of Earth Sciences*, v. 20, p. 1374-1388.

Dong, G., Morrison, G., Jaireth, S., Walshe, J.L., 1995, Quartz textures in epithermal veins, Queensland; classification, origin and implication, in McQueen, K.G., and Cox, S.F.,: Economic Geology and the Bulletin of the Society of Economic Geologists, v. 90, p. 1841-1856.

Dowling, K., Morrison, G., Keays, R.R., 1989, Application of quartz textures to the classification of gold deposits using North Queensland examples: Economic Geology Monographs, 6, p. 342-355.

Drieberg, S.L., 2003. The magmatic-hydrothermal architecture of the Archean volcanic massive sulfide (VMS) system at Panorama, Pilbara, Western Australia. Ph.D. thesis. University of Western Australia, 327 pp.

Duan, Z., Moller, N., and Weare, J.H., 1992, An equation of state for the CH_4-CO_2-H_2O system; I, Pure systems from 0 to 1000 degrees C and 0 and to 8000 bar: Geochimica et Cosmochimica Acta, v. 56, p. 2605-2617.

Dube, B., Mercier-Langevin, P., Hannington, M.D., Lafrance, B., Gosselin, G., Gosselin, P., 2007, The LaRonde Penna world-class Au-rich volcanogenic massive sulfide deposit, Abitibi, Quebec; mineralogy and geochemistry of alteration and implications for genesis and exploration: Economic Geology and the Bulletin of the Society of Economic Geologists, v. 102, p. 633-666.

Eadington, P.J., 1974, Microprobe analysis of the non-volatile constituents in fluid inclusions: Neues Jahrbuch fuer Mineralogie. Monatshefte, v. 11, p. 518-525.

Edmond, J.M., Craig, H., Gordon, L.I., and Holland, H.D., 1979, Chemistry of hydrothermal waters at 21 degrees N on the East Pacific Rise: Eos, Transactions, American Geophysical Union, v. 60, 864p.

Embley, R.W., 1988, Submersible investigation of an extinct hydrothermal system on the Galapagos Ridge; sulfide mounds, stockwork zone, and differentiated lavas in Jonasson, I.R., Perfit, M.R., Franklin, J.M., Tivey, M.A., Malahoff, A., Smith, M.F., Francis, T.J.G., and Barrett, T.J., eds.: The Canadian Mineralogist, v. 26, p. 517-539.

Farr, J.E., 1984, The geology, mineralogy, and geochemistry of the 070 faults of the Corbet mine, Noranda, Quebec: M.Sc. thesis, University of Toronto, 154p.

Fournier, R.O., 1985, The behaviour of silica in hydrothermal solutions, in Berger, B. R., and Bethke, P. M., eds., Geology and geochemistry of epithermal systems: Reviews in Economic Geology, v. 2, Society of Economic Geologists, p. 45-61.

Franklin, J.M., Sangster, D.F. and Lydon, J.W., 1981, Volcanogenic massive sulphide deposits: Economic Geology 75th Anniversary volume, p. 485-627.

Franklin, J.M., Eckstrand, O.R., Sinclair, W.D., Thorpe, R.I., Volcanic-associated massive sulphide base metals, 1995, Geology of Canadian mineral deposit types., eds. 8, p. 158-183

Franklin, J.M, Gibson, H.L., Jonasson, I.R. and Galley, A.G., 2005, Volcanogenic

Massive Sulphide Deposits, *in* Hedenquist, J.W., Thompson, J.F.H., Goldfarb, R.J., and Richards, J.P., eds., Economic Geology, 100th Anniversary Volume, The Economic Geology Publishing Company, p. 523-560.

Galley, A.G., 1993a, Characteristics of semi-conformable alteration zones associated with volcanogenic massive sulphide districts: Journal of Geochemical Exploration, v 48, p 175-200.

Galley, A.G., 1993b, Semi-conformable alteration zones in volcanogenic massive sulphide districts: Journal of Geochemical Exploration, v. 48, p. 175-200.

Galley, A.G., 2003, Composite synvolcanic intrusions associated with Precambrian VMS- related hydrothermal systems: Mineralium Deposita, v. 38, p. 443-473.

Gao, S., Liu, X., Yuan, H., Hattendorf, B., Guenther, D., Chen, L., and Hu, S., 2002, Determination of forty two major and trace elements in USGS and NIST SRM glasses by laser ablation-inductively coupled plasma-mass spectrometry: Geostandards Newsletter, v. 26, p.181-196.

Gibson, H.L., 1990, The Mine Sequence of the Central Noranda Volcanic Complex: Geology, alteration, massive sulphide deposits and volcanological reconstruction: Ph.D. thesis, Carleton University, Ottawa, Ontario, 715 p.

Gibson, H.L. and Watkinson, D.H., 1990, Volcanogenic massive sulphide deposits of the Noranda Cauldron and Shield Volcano, Quebec, *in* Rive, M., Verpaelst P., Gagnon, Y., Lulin, L.M., Riverin, G., and Simard, A., eds., The Northwestern Quebec Polymetallic Belt: A summary of 60 years of mining exploration, Canadian Institute of Mining and Metallurgy, Special Volume 43, p. 119-132.

Gibson, H.L., Watkinson, D.H., Watkins, J.J., Labrie, M., and Doiron, G., 1993, Volcanological reconstruction of the Corbet breccia pile, and Cu-Zn massive sulfide deposit, Noranda, Quebec: Exploration & Mining Geology, v. 2, p. 1-16.

Gibson, H., and Galley, A., 2007, Volcanogenic massive sulphide deposits of the Archean, Noranda District, Quebec, *in* Goodfellow, W. D., ed., Mineral Deposits of Canada: A Synthesis of Major Deposit-types, District Metallogeny, the Evolution of Geological Provinces, and Exploration Methods, Special Publication No. 5, Mineral Deposits Division, Geological Association of Canada, p. 533-552.

Gibson, H.L., Watkinson, D.H. and Comba, C.D.A., 1983, Silicification: Hydrothermal alteration in an Archean geothermal system within the Amulet Rhyolite formation, Noranda, Quebec: Economic Geology, v. 78: p. 954-971.

Giggenbach, W.F., 1980, Geothermal gas equilibria: Geochimica et Cosmochimica Acta, v. 44, p.2021-2032.

Goldie, R.J., 1976, The Flavrian and Powell plutons, Noranda area, Quebec; a geological investigation of the Flavrian and Powell plutons and their relationships to other rocks and structures of the Noranda area: Ph.D. thesis, Queen's University, Kingston, Ontario, 355p.

Goldie, R., 1979, Consanguineous Archean intrusive and extrusive rocks, Noranda, Quebec. Chemical similarities and differences: Precambrian Research, v. 9, p. 275-287.

Goldstein, R,H., 2003, Petrographic analysis of fluid inclusions: Fluid inclusions; analysis and interpretation; Short Course Series, v. 32, p. 9-53.

Goldstein, R.H. and Reynolds, T.J., 1994, Systematics of fluid inclusions in diagenetic minerals: SEPM Short Course, v. 31, 199p.

Götze, J., Plötze, M., and Habermann, D., 2001, Origin, spectral characteristics and practical applications of the cathodoluminescence (CL) of quartz – a review: Mineralogy and Petrology, v. 71, p. 225-250.

Götze, J., and Kempe., 2008, A comparison of optical microscope- and scanning electron microscope-based cathodoluminescence (CL) imaging and spectroscopy applied to geosciences: Mineralogical Magazine, v. 72, p. 909-924.

Götze, J., 2009, Chemistry, textures and physical properties of quartz – geological interpretation and technical application: Mineralogical Magazine, v. 73(4), p. 645-671.

Goutier, J., Ayer, J., and Thurston, P., 2006, Synthèse lithologique et stratigraphique de la Sous-province de l'Abitibi: Ministère des Ressources naturelles et de la Faune – Association de l'exploration minière du Québec, Québec, DV 2006-03, p. 24.

Graupner, T., Götze, J., Kempe, U., and Wolf, D., 2000, CL for characterizing quartz and trapped fluid inclusions in mesothermal quartz veins; Muruntau Au ore deposit, Uzbekistan: Mineralogical Magazine, v. 64, p.1007-1016.

Graupner, T., Bray, C.J., Spooner, E.T.C., and Herzig, P.M., 2001, Analysis of fluid inclusions in seafloor hydrothermal precipitates; testing and application of an integrated GC/IC technique: Chemical Geology, v. 177, p. 443-470.

Gutzmer, J., Banks, D. A., Lüders, V., Hoefs, J., Beukes, N. J., and von Bezing, K. L., 2003, Ancient sub-seafloor alteration of basaltic andesites of the Ongeluk Formation, South Africa: Implications for the chemistry of Paleoproterozoic seawater: Chemical Geology, v. 201, p. 37-53.

Halter, W.E., William-Jones, A.E., and Kontak, D.J., 1996, The role of greisenization in cassiterite precipitation at the East Kemptville tin deposit, Nova Scotia: Economic Geology and the Bulletin of the Society of Economic Geologists, v. 91, p. 368-385.

Halter, W.E., Webster, J.D., 2004, The magmatic to hydrothermal transition and its

bearing on ore-forming processes: Chemical Geology, v. 210, 1-4, 230p.

Hanley, J.J., Mungall, J.E., Bray, C.J., and Gorton, M.P., 2004, The origin of bulk and water-soluble Cl and Br enrichments in ore-hosting Sudbury breccia in the Fraser copper zone, Strathcona Embayment, Sudbury, Ontario, Canada: The Canadian Mineralogist, v. 42, p. 1777-1798.

Hannington, M.D., Jonasson, I.R., Herzig, P.M., Petersen, S., Humphris, S.E., Zierenberg, R.A., Mullineaux, L.S., and Thomson, R.E., 1995, Physical and chemical processes of seafloor mineralization at mid-ocean ridges: Seafloor hydrothermal systems; physical, chemical, biological, and geological interactions, Geophysical Monograph, v. 91, p. 115-157.

Hannington, M., Santaguida, F., Kjarsgaard, I.M., and Cathles, L.M., 2003, Regional-scale hydrothermal alteration in the central Blake River Group, western Abitibi Subprovince, Canada; implications for VMS prospectivity, Mineralium Deposita, v. 38, p. 393-422.

Haynes, F.M., Sterner, S.M., Bodnar, R.J., and Norman, D.I., 1988, Synthetic fluid inclusions in natural quartz; IV, Chemical analyses of fluid inclusions by SEM/EDA; evaluation of method: Geochimica et Cosmochimica Acta, Proceedings of the First annual meeting of the Pan-American current research on fluid inclusions group, v. 52, p. 969-977.

Heinrich, C.A., Cousens, D.R., 1989, Semi-quantitative electron microprobe analysis of fluid inclusion salts from the Mount Isa copper deposit (Queensland, Australia): Geochimica et Cosmochimica Acta, v. 53, p. 21-28.

Hedenquist, J.W., and Henley, R.W., 1985, The importance of CO_2 on freezing point measurements: Evidence from active geothermal systems and implications for epithermal ore deposition: Economic Geology, v. 80, p. 1379-1406.

Hedenquist, J.W., Reyes, A.G., Simmons, S.F., and Taguchi, S., 1992, The thermal framework and geochemical structure of geothermal and epithermal systems: A framework for interpreting fluid inclusion data.: European Journal of Mineralogy, v. 4, p. 989-1015.

Henley, R.W., 1985, The geothermal framework of epithermal systems, in Berger, B. R., and Bethke, P.M., eds., Geology and Geochemistry of Epithermal Systems, v. 2. Reviews in Economic Geology, Society of Economic Geologists, p. 1-24.

Hou, Z., Zaw, K., Qu, X., Ye, Q., Yu, J., Xu, M., Fu, D., and Yin, X., 2001, Origin of the Gacun volcanic-hosted massive sulfide deposit in Sichuan, China: Fluid inclusion and oxygen isotope evidence: Economic Geology, v. 96, p. 1491-1512.

Humphris, S.E., and Tivey, M.K., 2000, A synthesis of geological and geochemical investigations of the TAG hydrothermal field; insights into fluid-flow and mixing

processes in a hydrothermal system: Special Paper - Geological Society of America: Ophiolites and oceanic crust; new insights from field studies and the Ocean Drilling Program, v. 349, p. 213-235.

Huston, D.L., and Taylor, B.E., 1999, Genetic significance of oxygen and hydrogen isotope variations at the Kidd Creek volcanic-hosted massive sulfide deposit, Ontario, Canada: Economic Geology Monograph 10, p. 335-350.

Ikingura, J.R., Hydrothermal alteration and Cu-Zn sulfide mineralization in the D-68 Zone, Corbet Mine, Noranda District, Quebec, Canada: M.Sc. thesis. Carleton University, Ottawa, Ontario, 326p.

Ioannou, S.E., Götze, J., Weiershäuser, L., Zubowski, S.M., and Spooner, E.T.C., 2004, Cathodoluminescence characteristics of Archean VMS-related quartz: Noranda, Ben Nevis and Matagami districts, Abitibi subprovince, Canada: Geochemistry, Geophysics, Geosystems, v. 5, Q02007, doi:10.1029/2003GC000613.

Ioannou, S.E., 2004, Hydrothermal fluid chemistry and flow paths associated with the Archean Matagami VMS system, Abitibi Subprovince, Canada: Ph.D. thesis. University of Toronto, Ontario, 275p.

Ioannou, S.E., and Spooner, E.T.C., 2007, Fluid Temperature and Salinity Characteristics of the Matagami Volcanogenic Massive Sulfide District, Quebec: Economic Geology, v. 102, p.691-715.

Janecky, D.R. and Seyfried, W.E., Jr., 1982, The solubility of magnesium-hydroxide-sulfate-hydrate in seawater at elevated temperatures and pressures: American Journal of Earth Sciences, v. 283, 831-860.

Javoy, M., and Pineau, F., 1991, The volatiles record of a "popping" rock from the Mid-Atlantic Ridge at 14 degrees N: chemical and isotopic composition of gas trapped in vesicles: Earth and Planetary Science Letters, v. 107, p. 598-611.

Jolly, W.T., 1978, Metamorphic history of the Archean Abitibi belt. In: Metamorphism in the Canadian Shield: Geological Survey of Canada, Paper 78-10, p. 66–78.

Jolly, W.T., 1980, Development and degradation of Archean lavas, Abitibi area, Canada, in light of major element geochemistry: Journal of Petrology, v. 21, p. 323–363.

Kennedy, L.P., 1985, The geology and geochemistry of the Archean Flavrian Pluton, Noranda, Quebec: Ph.D. thesis. University of Western Ontario, Ontario, 469p.

Kerr, D.J. and Gibson, H.L., 1993, A comparison of the Horne volcanogenic massive sulphide deposit and intracauldron deposits of the Mine Sequence, Noranda, Quebec: Economic Geology, v. 88, p. 1419-1442.

Kheang, L., 1984, Magmatic water/sea water mixing in an Archean hydrothermal

system related to the formation of Millenbach Cu-Zn deposit, Rouyn-Noranda, Quebec, 1984.

Knuckey, M.J. and Watkins, J.J., 1982, The geology of the Corbet massive sulphide deposit, Noranda District, Quebec, Canada: Geological Association of Canada, Special Paper 25, p. 255-296.

Kontak, D.J., 2004: Analysis of decrepitate mounds as a complement to fluid inclusion thermometric data: Case studies from granitic environments in Nova Scotia and Peru. Canadian Mineralogist, vol. 42, p. 1315-1330.

Lilley, M.D., Butterfield, D.A., Olson, E.J., Lupton, J.E., Macko, S.A., and McDuff, R.E.,1993, Anomalous CH4 and NH4+ concentrations at an unsedimented mid-ocean-ridge hydrothermal system: Nature v. 364, p. 45–47.

Liu, W., McPhail, D.C., Brugger, J., 2001, An experimental study of copper(I)-chloride and copper(I)-acetate complexing in hydrothermal solutions between 50 degrees C and 250 degrees C and vapor-saturated pressure: Geochimica et Cosmochimica Acta, v. 65, p. 2937-2948.

Loucks, R.R., 2000, Precise geothermometry on fluid inclusion populations that trapped mixtures of immiscible fluids: American Journal of Science, v. 300, p. 23-59.

Lydon, J.W., 1988, Volcanogenic massive sulphide deposits. Part 2: genetic models: Geoscience Canada, v. 15, p. 43-65.

Marshall, D.J., 1988, Cathodoluminescence of geological materials. Unwin-Hyman, Boston, 146 p

Mathez, E.A., Webster, J.D., 2005, Partitioning behavior of chlorine and fluorine in the system apatitite-silicate melt-fluid: Geochimica et Cosmochimica Acta, v. 69, p. 1275-1286.

Mercier-Langevin, P; Goutier, J; Ross, P -S; McNicoll, V; Monecke, T; Dion, C; Dubé, B; Thurston, P; Bécu, V; Gibson, H; Hannington, M; Galley, A., 2011, The Blake River Group of the Abitibi Greenstone Belt and its unique VMS and gold-rich VMS endowment: Geological Association of Canada-Mineralogical Association of Canada, Field Trip Guidebook 2b, 61p.

Mortensen, J.K., 1993, U-Pb geochronology of the eastern Abitibi Subprovince; Part 2: Noranda- Kirkland Lake area: Canadian Journal of Earth Sciences, v. 30, p. 29-41.

Moura, A., 2005, Fluids from the Neves Corvo massive sulphide ores, Iberian pyrite belt, Portugal: Chemical Geology, v. 223, 1-3, p. 153-169

Neuser, R. D., F. Bruhn, J. Götze, D. Habermann, and D. K. Richter, 1995, Kathodolumineszenz: Methodik und Anwendung, Zentralblatt für Geol. und

Paläontologie Teil, p. 287-306.

Oakes, C.S., Bodnar, R.J., and Simonson, J.M., 1990, The system NaCl-CaCl$_2$–H$_2$O: I. the ice liquidus at 1 atm total pressure: Geochimica et Cosmochimica Acta, v. 54, p. 603-610.

Perny, B., Eberhardt, P., Ramseyer, K. and Mullis, J., 1992, Microdistribution of aluminium, lithium and sodium in quartz: possible causes and correlation with short-lived cathodoluminescence: American Mineralogist, v. 77, p. 534-544.

Powell, E.G., Carmichael, D.M., Hodgson, C.J., 1994, Conditions and timing of metamorphism in the southern Abitibi greenstone belt, Quebec: Canadien Journal of Earth Sciences, v. 32, p. 787-805.

Pearson, V., Daigneault, R., 2009, An Archean megacaldera complex: The Blake River Group, Abitibi greenstone belt: Precambrian Research, v. 168, p. 66-82.

Potter, J., and Longstaffe, F.J., 2007, A gas chromatograph, continuous flow-isotope ratio-mass spectrometry method for delta ^{13}C and delta D measurement of complex fluid inclusion volatiles; examples from the Khibina alkaline igneous complex, northwest Russia and the South Wales coal fields: Chemical Geology, v. 244, p.186-201.

Potter, J., Zubowski, S.M., Spooner, E.T.C., Bray, C.J., Longstaffe, F.J., and Gibson, H.L., 2007, An online GC-irMS crushing technique for stable isotope analysis of trace gases in aqueous-dominated fluid inclusions: An example from the Noranda VMS District, Quebec, Canada: European Current Research on Fluid Inclusions (ECROFI-XIX) University of Bern, Switzerland,. Abstract Volume, p. 276.

Ramboz, C., Pichavant, M., and Weisbrod, A., 1982, Fluid immisciblity in natural processes: Use and misuse of fluid inlcusion data. II. Interpretation of fluid inclusion data in terms of immiscibility: Chemical Geology, v. 37. P. 29-48.

Ramseyer, K., Baumann, J., Matter, A., and Mullis, J., 1988, Cathodoluminescence colours of a-quartz: Mineralogical Magazine, v. 52, p. 669-677.

Ramseyer, K., and Mullis, J., 1990, Factors influencing short-lived blue cathodoluminescence of a-quatrz: American Mineralogist, v. 75, p. 791-800.

Richard, M.G., 1999, Evolution of the Flavrian Pluton and its association with VHMS deposits and granitoid-hosted gold deposits of the Noranda Cauldron: Rouyn-Noranda, Quebec, Canada. Ph.D. thesis, Université de Montreal, Montreal, Québec, 318p.

Robert, F., Boullier, M., and Firdaous, K., 1995, Gold-quartz veins in metamorphic terranes and their bearing on the role of fluids in faulting: Journal of Geophysical Research, v. 100, p. 12,861-12,879.

Roedder, E., and Bogdanov, B., 1977, Changes in ore fluid with time, from fluid

inclusion studies at Creede, Colorado: Symposium of the International Association on the Genesis of Ore Deposits, [Proceedings], v. 2, p.179-185.

Roedder, E., 1979, Fluid inclusions as samples of ore fluids. In: Barnes, H.L. (Ed.), Geochemistry of Hydrothermal Ore Deposits. 2nd ed. Wiley, New York, 684-737.

Roedder, E., and Bodnar, R.J., 1980, Geologic pressure determinations from fluid inclusion studies: Annual Review of Earth and Planetary Sciences, v. 8, p. 263–301.

Roedder, E., 1984, Fluid inclusions: Reviews in Mineralogy, v. 12, 646 p.

Roedder, E., 1992, Fluid inclusion evidence for immiscibility in magmatic differentiation: Geochimica et Cosmochimica Acta, v. 56, p. 5-20.

Samson, I. M., Anderson, A. J., Marshall, D., eds., 2003, Fluid inclusions; analysis and interpretation: Short Course Series, v. 32, 374 p.

Sánchez-España, J., Velasco, F., Boyce, A. J., and Fallick, A. E., 2003, Source and evolution of ore-forming hydrothermal fluids in the northern Iberian Pyrite Belt massive sulphide deposits (SW Spain): evidence from fluid inclusions and stable isotopes: Mineralium Deposita, v. 38, p. 519-537.

Santaguida, F., Gibson, H.L., Watkinson, D.H., and Hannington, M.D., 1998, Semi-conformable epidote-quartz hydrothermal alteration in the Central Noranda Volcanic Complex: Relationship to volcanic activity and VMS mineralization: CAMIRO Project 94E07, The Use of Regional-Scale Alteration and Subvolcanic Intrusions in the Exploration for Volcanic-Associated Massive Sulphide Deposits, unpublished report, p. 139-180.

Santaguida, F., 1999, The paragenetic relationships of epidote-quartz hydrothermal alteration within the Noranda Volcanic Complex, Quebec: PhD thesis, Carleton University, Ontario, 302 p.

Sawkins, F.J. and Kowalik, J., 1981, The source of ore metals at Buchans; magmatic versus leaching models: The Buchans orebodies; fifty years of geology and mining: Geological Association of Canada – Special Paper 22, p. 255-267.

Schandl, E.S., 2004, The role of saline fluids base-metal and gold mineralization at the Cobalt Hill prospect northeast of the Sudbury igneous complex, Ontario; a fluid-inclusion and mineralogical study: The Canadian Mineralogist, v. 42, p. 1541-1562.

Schandl, E.S., and Bleeker, W., 1999, Hydrothermal and metamorphic fluids of the Kidd Creek volcanogenic massive sulfide deposit: Preliminary evidence from fluid inclusions: Economic Geology Monograph 10, p. 379–387.

Scott, S.D., 1997, Submarine hydrothermal systems and deposits, in Barnes, H.

L., ed., Geochemistry of Hydrothermal Ore Deposits: New York, John Wiley and Sons, p. 797-875.

Setterfield, T.N., 1984, Nature and significance of the McDougall-Despina fault set, Noranda, Quebec: M.Sc. thesis. University of Western Ontario, Ontario, 148p.

Setterfield, T., 1987, Massive and brecciated dikes in the McDougall and Despina faults, Noranda, Quebec, Canada: Journal of Volcanology & Geothermal Research, v. 31, p. 87-97.

Setterfield, T.N., Hodder, R.W., Gibson, H.L., and Watkins, J.J., 1995, The McDougall-Despina fault set, Noranda, Quebec; evidence for fault-controlled volcanism and hydrothermal fluid flow: Exploration and Mining Geology, v. 4, p. 381-393.

Seyfried, W.E., Jr., and Janecky, D.R., 1985, Heavy metal and sulfur transport during subcritical and supercritical hydrothermal alteration of basalt: Influence of fluid pressure and basalt composition and crystallinity: Geochimica et Cosmochimica Acta, v. 49, p. 2545-2560.

Seyfried, W.E., Jr., Berndt, M.E., and Seewald, J.S., 1988, Hydrothermal alteration processes at mid-ocean ridges: constraints from diabase alteration experiments, hot-spring fluids and composition of the ocean crust: Canadian Mineralogist, vol. 26, p.787-804

Seyfried, W.E., Jr., Ding, K., Berndt, M.E., and Chen, X., 1999, Experimental and theoretical controls on the composition of mid-ocean ridge hydrothermal fluids: Reviews in Economic Geology, v. 8, p. 181–200.

Sherlock, R.L., Roth, T., Spooner, E.T.C., and Bray, C.J., 1999, Origin of the Eskay Creek precious metal-rich volcanogenic massive sulfide deposit: Fluid inclusion and stable isotope evidence: Economic Geology, v. 94, p. 803-824.

Shepherd, T.J., Rankin, A.H., and Alderton, D.H.M., 1985, A practical guide to fluid inclusion studies: Glasgow, Blackie, 239 p.

Sherwood Lollar, B., Frape, S.K., Weise, S.M., Fritz, P., Macko, S.A., Welhan, J.A., 1993, Abiogenic methanogenesis in crystalline rocks: Geochimica et Cosmochimica Acta, v. 57, p. 5087-5097.

Siegel, G.H., and Marrone, M.J., 1981, Photoluminescence in as-drawn and irradiated silica optical fibers: an assessment of the role of nonbridging oxygen defect centres. Journal of Non-Crystalline Solids, v. 45, p. 235-247.

Sourirajan, S., and Kennedy, G.C., 1962, The system H2O-NaCl at elevated temperatures and pressures: American Journal of Science, v. 260, p.115–141.

Spence, C.D., and de Rosen-Spence, A.F., 1975, The place of sulphide mineralization in

the volcanic sequence at Noranda, Quebec: Economic Geology, v. 70, p. 90-101.

Spooner, E.T.C., Hollister, L.S., Crawford, M.L., 1981, Fluid inclusion studies of hydrothermal ore deposits: Short Course Handbook; Fluid inclusions, applications to petrology, v. 6, p. 209-240.

Sprunt, E.S., Dengler, L.A., and Sloan, D., 1978, Effects of metamorphism on quartz cathodoluminescence: Geology, v. 6, p. 305-308.

Sterner, S.M., and Bodnar, R.J., 1984, Synthetic fluid inclusions in natural quartz. I. Compositional types synthesized and applications to experimental geochemistry: Geochimica et Cosmochimica Acta, v. 48, p. 2659-2668.

Sterner, S.M., and Bodnar, R.J., 1989, Synthetic fluid inclusion; VII, Re-equilibration of fluid inclusions in quartz during laboratory simulated metamorphic burial and uplift: Journal of Metamorphic Geology, v. 7, p. 243-260.

Takeno, N., Ishido, T., Pritchett, J.W., Shigeno, H., 2000, Dissolution, transportation, and precipitation of silica in geothermal systems: Chishitsu Chosajo Hokoku = Report - Geological Survey of Japan, Studies on deep-seated geothermal resources; with special emphasis on analyses and evaluations of the deep geothermal system at the Kakkonda area, Japan, v. 284, p.235-248.

Takashima, I., Yamada, E., 1976, Rock alteration and hydrothermal systems in the Onikobe geothermal area, northeastern Japan: Chishitsu Chosajo Hokoku = Report - Geological Survey of Japan, v. 268, p. 229-244.

Teinturier, S., and Pironon, J., 2003, Synthetic fluid inclusions as a recorders of microfracture healing and overgrowth formation rates: American Mineralogist, v. 88, p.1204-1208.

Thomas, A.V., Spooner, E.T.C., Bodnar, R.J., 1992, The volatile geochemistry of magmatic H_2O-CO_2 fluid inclusions from the Tanco zoned granitic pegmatite, southeastern Manitoba, Canada: Geochimica et Cosmochimica Acta, v. 56, p. 49-65.

Ulrich, T., Golding, S.D., and Taube, A., 2000, Comparison between the Mount Morgan Au-Cu deposit and the adjacent stratabound Fe-(Cu-Zn) mineralization: Volcanic environments and massive sulfides, Tasmania, Australia, p. 217-218.

van den Kerkhof, A.M., Hein, U.F., Andersen, T., 2000, Fluid inclusion petrography: Lithos; Fluid inclusions; phase relationships-methods-applications; special volume in honour of Jacques Touret, v. 55, p. 27-47.

Vityk, M.O., and Bodnar, R.J., 1995, Textural evolution of synthetic fluid inclusions in quartz during reequilibration, with applications to tectonic reconstruction: Contributions to Mineralogy & Petrology, v. 121, p. 309-323.

Von Damm, K.L., and Bischoff, J.L., 1987, Chemistry of hydrothermal solutions from the southern Juan de Fuca Ridge: Journal of Geophysical Research, v. 92, p. 11334-11346.

Von Damm, K. L., 1990, Seafloor hydrothermal activity: Black smoker chemistry and chimneys: Annual Reviews of Earth and Planetary Science, v. 18, p. 173-204.

Walsh, J.F., Kesler, S.E., Duff, D., and Cloke, P.L., 1988, Fluid inclusion geochemistry of high-grade, vein-hosted gold ore at the Pamour Mine, Porcupine Camp, Ontario: Economic Geology and the Bulletin of the Society of Economic Geologists, v. 83, p. 1347-1368.

Webster, J.D., Kinzler, R.J., and Mathez, E.A., 1999, Chloride and water solubility in basalt and andesite melts and implications for magmatic degassing: Geochimica et Cosmochimica Acta, v. 63, p. 729-738.

Weiershäeuser, L., 2005, Fluids Associated with an Archean Regional Hydrothermal System, Abitibi Subprovince, Canada; Fluid Inclusion Characteristics and Hot Cathode Cathodoluminescence Characteristics of Host Minerals – Implications for Archean Seawater Chemistry and Magmatic Hydrothermal Processes: Ph.D Thesis. University of Toronto, 150 pp.

Weiershäeuser, L., and Spooner, E.T.C., 2005, Seafloor hydrothermal fluids, Ben Nevis area, Abitibi greenstone belt; implications for Archean (approximately 2.7 Ga) seawater properties: Precambrian Research, v.138, p. 89-123.

Welhan, J.A., and Schoell, M., 1988, Origins of methane in hydrothermal systems: Chemical Geology, v. 71, p.183-198.

Weres, O., Apps, J.A., Narasimhan, T.N., 1982, Prediction of chemical problems in the reinjection of geothermal brines: Special Paper - Geological Society of America, v. 189, 407-426.

Wilkinson, J.J., 2001, Fluid inclusions in hydrothermal ore deposits: Lithos, v. 55, p. 229-272.

Xiao, Z., Gammons, C.H., William-Jones, A.E., 1998, Experimental study of copper(I) chloride complexing in hydrothermal solutions at 40 to 300 degrees C and saturated water vapor pressure: Geochimica et Cosmochimica Acta, v. 62, p. 2949-2964.

Yang, K., and Scott, S.D., 1996, Possible contributions of a metal-rich magmatic fluid to a seafloor hydrothermal system: Nature, v. 383, p. 420–423.

Zhang, Y., and Frantz, J.D., 1987, Determination of the homogenization temperatures and densities of supercritical fluids in the system $NaCl-KCl-CaCl_2-H_2O$ using synthetic fluid inclusions: Chemical Geology, v. 64, p. 335–350.

Zaw, K., Gemmell, J. B., Large, R.R., Mernagh, T.P., Ryan, C.G., and Vielreicher, R.M., 1996, Evolution and source of ore fluids in the stringer system, Hellyer VHMS deposit, Tasmania, Australia; Evidence from fluid inclusion microthermometry and geochemistry: Ore Geology Reviews, v. 10, p. 251-278.

Zubowski, S.M., 2001, Corbet Archean VMS deposit, Noranda, Quebec; Paragenesis and FI microthermometry, unpublished B.Sc. thesis, University of Toronto, p. 1-95.